Universitá degli Studi di Trento

facoltà di scienze matematiche, fisiche e naturali

Tesi di Dottorato di Ricerca in Fisica

ULTRACOLD BOSONIC GASES: SUPERFLUIDITY AND QUANTUM INTERFEROMETRY

Francesco Piazza

Relatore:
Dr. Augusto Smerzi

Dottorato di Ricerca in Fisica, XXIII Ciclo
Febbraio 2011

Contents

List of Figures

Motivation

Since their experimental realization in 1995, Bose-Einstein condensates (BECs) of ultracold atoms have attracted a lot of interest from different communities. One reason can be seen in the fact that these systems contain features giving rise to many outstanding physical phenomena, combined with a remarkable "cleanness". The latter means both a deeper theoretical understanding (than, for instance, for condensed matter systems), and also a greater control and flexibility of experimental trapping and probing tools. Apart from allowing for a cleaner and more controlled observation of phenomena which have already been studied in completely different fields, ultracold BECs give access to novel regimes, and can for instance be employed as quantum simulators for the realization of a chosen Hamiltonian.

Therefore, both fundational and technological problems, either coming from the field of condensed matter, optics, etc., or related to novel unexplored regimes, are being studied in the context of ultracold BECs. This dissertation is devoted in particular to two among these, namely i) superfluidity: Josephson effects, critical velocities and dissipation dynamics, and ii) quantum interferometry. As we shall see, even though these phenomena have been largely studied before the realization of condensates with ultracold atoms, in this new context they manifest novel features which are essentially related to the peculiar properties of the ultracold BEC systems.

Though historically two clearly separate fields, superfluidity being investigated mostly with helium II and (quantum) interferometers being implemented with light, they can both be studied with ultracold atomic BECs. Indeed, the BECs macroscopic phase coherence allows on the one hand for quantum oscillations between two coupled reservoirs (Josephson effects), and, BECs having also a condensate fraction much larger than superfluid helium, on the other hand for high contrast interference and an enhanced coherent interaction with external fields, which are essential in a good interferometer. Moreover, what makes dilute BECs very special systems is the nature of atom-atom interactions. Ultracold atomic condensates are indeed dilute, therefore cleaner than strongly interacting systems, and yet interactions give rise to non-trivial nonlinearities, which, for instance, make a BEC a proper superfluid, with a finite critical velocity below

which it shows no viscosity. These nonlinearities are also extremely relevant for quantum interferometry, since they allow for the creation of entangled states (with non-classical particle correlations), which can be employed to largely enhance the interferometer precision. In addition, Feschbach resonances are a most valuable experimental tool, by which the strength of the atom-atom interaction can be fine-tuned through external magnetic fields.

The aims of this dissertation are twofold. Firstly, the study of superfluidity, presented in the first part, has more a fundational character, since we investigate some well known problems, already raised in the context of superfluid helium, in order to gain a deeper understanding, by exploiting the cleannes of dilute BECs systems, as well as analyzing the new features emerging from the unique dilute BECs properties. We study the BEC flow through weak-links, first analyzing the various regimes of transport by the current-phase relation and the Josephson plasma oscillations, and then turning to the superfluid instability, determining critical velocities and examining the dissipation dynamics in different geometries and dimensionalities. Secondly, the analysis of quantum interferometry, given in the second part, has instead a more technological character, since we propose two possible implementation of interferometric protocols in double-well traps, with application to the measurement of weak-forces, and study their sensitivity in detail, especially in relation to its possible quantum enhancement.

Part I

Superfluidity in Bose-Einstein Condensates

Superfluidity in short

Superfluidity manifests itself in different ways, related to both stationary and dynamical properties of a system, and it would be difficult to define it as one single phenomenon [50]. However, the basic ingredients giving rise to superfluidity are essentialy two: i) macroscopic phase coherence, and ii) interaction among the system constituents. As noted by London, the macroscopic coherence is enforced by the presence of a BEC, which, even if involving a tiny but finite portion of the constituents, allows to assign an order parameter, and in turn a phase, to the macroscopic system. This is why superfluidity appears in bosonic liquids[1] cooled to a sufficiently low temperature.

The first experimental observation of superfluidity dates back to 1938, and was simultaneously performed by Kapitza in Moscow and Allen and Misener in Cambridge, who used liquid ^{4}He. When cooled below the so called "lambda temperature" $T_\lambda \sim 2.17K$, the fluid suddenly showed practically no viscosity. This most straightforward manifestation of superfluidity, as noted above, is just one of many which have later been observed with helium, and it is not the aim of this brief introduction to give an organic treatment of the matter.

In what follows, we will deal with the observation of superfluid phenomena in ultracold dilute gases of bosonic atoms. As we shall see, these dilute BECs, are good systems where to study superfluidity, being very flexible and clean, and also well described by simple theoretical models. In particular, we will concentrate on two main aspects of this vast subject: i) Josephson Effect(s), and ii) the existence of critical velocities below which the superfluid flow is stationary. The first is the most direct manifestation of macroscopic phase coherence and the quantum nature of a superfluid, as we shall discuss in chapter 1. The second aspect is directly related to the absence of viscosity, and will be treated in chapter 2.

[1] we used the word "liquid" as opposed to "solid", since in this last case no superfluid would be present.

Chapter 1

Transport through weak links and Josephson effects

1.1 Supercurrents and the Josephson-Anderson relation

One of the most striking manifestations of superfluidity is the presence of a non-zero stationary mass current between two coupled reservoirs even in absence of any external drive, what can be called a "supercurrent". This is essentially related to an extended coherence, due to a non-zero BEC fraction, allowing us to assign an order parameter to each piece of superfluid. In this chapter, we will discuss the consequences of this coherence, essentially following the arguments used by Anderson [7], in order to give a general derivation of the basic equations explaining the Josephson effect(s). A useful definition of a superfluid[1] is indeed the following:

$$\langle\hat{\psi}(\boldsymbol{r})\rangle = f(\boldsymbol{r})e^{i\phi(\boldsymbol{r})} \neq 0, \tag{1.1}$$

where f is a real function, and $\langle\rangle$ indicates the average value over some many-body state. In Eq. (1.1), $\hat{\psi} = \sum_i \varphi_i \hat{a}_i$ is the field operator, with $\{\varphi_i\}$ forming a set of single particle basis states and $\hat{a}_i$ being the destruction operator corresponding to the i-th state. In order to have a non-zero order parameter, the many body state must be written as a superposition:

$$|\Psi\rangle = \sum_N c_N |\Psi_N\rangle, \tag{1.2}$$

[1] along the line of what P. W. mantains [7], we consider this definition more useful than Off-Diagonal-Long-Range Order [101], which nontheless has the advantage of avoiding the use of superpositions of states of different numbers of particles, whose physical interpretation can be misleading.

where c_N are complex coefficients, and $|\Psi_N\rangle$ is a many-body state of N particles. Therefore the order parameter reads:

$$\langle\hat{\psi}(\boldsymbol{r})\rangle = \sum_N c^*_{N-1} c_N \mathrm{M}_N(\boldsymbol{r}), \tag{1.3}$$

where $\mathrm{M}_N(\boldsymbol{r}) = \langle\Psi_{N-1}|\hat{\psi}(\boldsymbol{r})|\Psi_N\rangle$. In a perfect BEC, where the condensate fraction is 100%, we have $|\Psi_N\rangle = \frac{(\hat{a}_0^\dagger)^N}{\sqrt{N!}}|0\rangle$, where $|0\rangle$ is the vacuum state, and the matrix element $\mathrm{M}_N(\boldsymbol{r}) = \varphi_0(\boldsymbol{r})\sqrt{N}$ is maximal. On the other hand, in ^{4}He, which is a strongly interacting system, this matrix element is around 10% of its maximum value. This higher depletion of the condensate, as we shall discuss below, does not imply that the system is "less superfluid". What is instead crucial to satisfy Eq. (1.1) is the phase coherence between each coefficient c_N in the superposition (1.2). Indeed, choosing for instance the many-body state (1.2) as a coherent state

$$|\Psi(\bar{N};\phi)\rangle = e^{-\bar{N}/2}\sum_N \frac{\bar{N}^{N/2} e^{iN\phi}}{\sqrt{N!}}|\Psi_N\rangle, \tag{1.4}$$

with average total number $\bar{N}$ and phase ϕ, one obtains, if $\bar{N} \gg 1$,

$$\langle\hat{\psi}(\boldsymbol{r})\rangle \simeq \bar{\mathrm{M}}(\boldsymbol{r})e^{i\phi}, \tag{1.5}$$

where the $\bar{\mathrm{M}}(\boldsymbol{r}) = \sum_N |c_N|^2 \mathrm{M}_N(\boldsymbol{r})$ is the mean value of the matrix element with respect to the total number distribution.

Using $|\Psi_N\rangle$ ($|\Psi(\bar{N};\phi)\rangle$), one can construct a number (phase) representation for the many-body states of the system, where the total number operator N is conjugate to the phase operator ϕ, insofar as N corresponds to $-i\frac{\partial}{\partial\phi}$, and ϕ to $i\frac{\partial}{\partial N}$. This enables us to write the equations for the average values of N and ϕ:

$$\hbar\frac{d}{dt}\langle N\rangle = \langle\frac{\partial H}{\partial\phi}\rangle \tag{1.6}$$

$$\hbar\frac{d}{dt}\langle\phi\rangle = -\langle\frac{\partial H}{\partial N}\rangle. \tag{1.7}$$

If we are in a superfluid state, the average value is to be taken over a coherent state (1.4) with some $\bar{N}$ and phase ϕ_0. In the limit of $\bar{N} \gg 1$, the fluctuations of number and phase can be neglected, and we are left with two equations for $\bar{N}$ and ϕ_0, which are of uttermost importance for superfluids:

$$\hbar\frac{d\bar{N}}{dt} = \frac{\partial E}{\partial\phi_0} \tag{1.8}$$

$$\hbar\frac{d\phi_0}{dt} = -\frac{\partial E}{\partial\bar{N}} = -\mu, \tag{1.9}$$

where we adopted the standard relation $\mu = \frac{\partial E}{\partial N}$ connecting the energy E and the chemical potential μ. In the following, we will drop the $\bar{N}$ notation, and use simply N.

Let us start with the current equation (1.8). Since the properties of an isolated quantum system must be independent of global phases, the total particle number N of a superfluid is conserved in absence of coupling to other systems. On the other hand, when two pieces of superfluid $\mathcal{S}_1$ and $\mathcal{S}_2$, with phases ϕ_1 and ϕ_2, are connected, the particle number in each of them can change in time. It is very instructive to consider these two parts as belonging to a larger superfluid reservoir. According to our definition of superfluidity, the reservoir must be phase coherent as a whole, that is, be described by something like a coherent state (1.4), with a global phase ϕ. This implies that the coupling energy E_J between $\mathcal{S}_1$ and $\mathcal{S}_2$ must i) depend on $\Delta\phi = \phi_1 - \phi_2$, and ii) have a minimum when $\Delta\phi = 0$. Now, using Eq. (1.8), and neglecting the coupling to other elements of the reservoir[2], we can write the total flux as:

$$\frac{dN_1}{dt} = -\frac{dN_2}{dt} = \frac{1}{\hbar}\frac{\partial E_\mathrm{J}}{\partial \Delta\phi}. \tag{1.10}$$

If $\mathcal{S}_1$, $\mathcal{S}_2$ were two macroscopic reservoirs connected by some link, the above equation would describe the usual Josephson current across the link used for originally for superconductors [42]. However, let us once again consider the case where $\mathcal{S}_1$ and $\mathcal{S}_2$ are two infinitesimal neighboring pieces of a superfluid reservoir, and rewrite Eq. (1.10) for the current in the spatial continuum limit:

$$\boldsymbol{J} = \frac{1}{\hbar}\frac{\delta E_\mathrm{J}[f, \boldsymbol{\nabla}\phi]}{\delta \boldsymbol{\nabla}\phi}, \tag{1.11}$$

where $\boldsymbol{J}$ is the current, and now the energy $E_\mathrm{J}[f, \boldsymbol{\nabla}\phi]$ is a functional of the phase gradient and of the amplitude f. Since E_J must have a minimum when $|\boldsymbol{\nabla}\phi| = 0$, we can approximately write: $E_\mathrm{J}[f, \boldsymbol{\nabla}\phi] \simeq \int d^3r E(f)|\boldsymbol{\nabla}\phi|^2$, and thus:

$$\boldsymbol{J} = \frac{2}{\hbar}E(f)\boldsymbol{\nabla}\phi. \tag{1.12}$$

Eq. (1.12) shows that a stationary current can be sustained by a spatially varying phase, which, as we claimed at the beginning of this chapter, is one striking manifestation of superfluidity. Moreover, the current (1.12) can be rightfully called a supercurrent, since it can exist in absence of any external drive, as one can see from Eq. (1.9). The latter, often referred to as the Josephson-Anderson relation, tells us indeed that the phase difference between the two superfluid elements $\mathcal{S}_1$ and $\mathcal{S}_2$ must change in time in presence of a chemical potential difference:

$$\frac{d\Delta\phi}{dt} = -\frac{\Delta\mu}{\hbar}, \tag{1.13}$$

[2]including this coupling in the reasonment is not important for what is discussed here

which also means that no chemical potential difference must be present in the system in the steady state. In the spatial continuum limit, the above relation reads:

$$\hbar \frac{d\boldsymbol{\nabla}\phi}{dt} = \mathbf{F}, \tag{1.14}$$

where $\mathbf{F}$ is the total force acting on the particles. We immediately see that a stationary current in Eq. (1.12), implying a stationary gradient of the phase, in turn means, by Eq. (1.14), $F = 0$: no net force applied to the system. The Josephson-Anderson relation provides also a definition of the velocity of a superfluid particle. Since $\boldsymbol{F} = d\boldsymbol{p}/dt = md\boldsymbol{v}/dt$, we have by Eq. (1.14):

$$\boldsymbol{v}_s = \frac{\hbar}{m}\boldsymbol{\nabla}\phi. \tag{1.15}$$

The Josephson-Anderson relation (1.14), through the identity (1.15), shows how superfluid particles accelerate without friction in presence of any external drive. This identity[3] can also be substituted in the equation for the supercurrent (1.12), in order to link the coupling energy E_J to the superfluid density n_s:

$$\frac{\delta^2 E_\mathrm{J}}{\delta|\boldsymbol{\nabla}\phi|^2} = \frac{\hbar^2}{2m} n_s \tag{1.16}$$

Let us conlude this general section with some remarks. All the arguments provided so far are based on the definition of a superfluid as a system which tends to preserve phase coherence on a macroscopic scale. We formalized this statement by assuming that the many-body state of the system was a coherent state of the form (1.4). As Anderson notes, an indication that such kind of states are actually the ones occuring in superfluids comes directly from the existence of the coupling energy E_J. Indeed, let us consider two coupled pieces of superfluid $\mathcal{S}_1$ and $\mathcal{S}_2$, respectively in quantum states $|\Psi_1\rangle$ and $|\Psi_2\rangle$, and calculate the kinetic energy matrix element for the transfer of one particle from $\mathcal{S}_1$ to $\mathcal{S}_2$:

$$(\langle\Psi_1| \otimes \langle\Psi_2|)\hat{K}(|\Psi_1\rangle \otimes |\Psi_2\rangle) = \sum_{N_1,N_2} c^*_{N_1+1} c_{N_1} c^*_{N_2-1} c_{N_2} K_{12}, \tag{1.17}$$

where $\hat{K}$ is the kinetic energy operator, and $K_{12} = (\langle\Psi_{N1}| \otimes \langle\Psi_{N2}|)\hat{K}(|\Psi_{N1}\rangle \otimes |\Psi_{N2}\rangle)$ is its matrix element on states with fixed total number of particles. We see that the kinetic energy gain from the transfer of particles between the two pieces of superfluid is maximal when the many-body state of $\mathcal{S}_{1,2}$ is a coherent state (1.4). In other words, the existence of a coupling favors the presence of macroscopic phase coherence, by creating many-body states of the form (1.4).

[3] we will not discuss here to what extent v_s does correspond to an actual superfluid particle velocity [7]

It is important to note that the existence of a superfluid in the way defined here, seems to necessarily imply the existence of supercurrents of the kind (1.12). Indeed, macroscopic phase coherence requires a coupling energy which is minimum when the phase difference between two superfluid elements is zero, which in turn means the existence of currents (1.12). The backward implication seems also to hold, since having a stationary current, i.e. $dN/dt \neq 0$ in a stationary state[4], requires the existence of a meaningful phase, being the latter the variable dynamically conjugated to the number through $\partial E_{\mathrm{J}}/\partial\phi$.

In this section, we have derived on general grounds the two basic equations which govern superfluid transport, namely, the current equation (1.12) and the Josephson-Anderson relation (1.13). As we shall discuss below, these two equations explain Josephson physics in both the stationary regime (the phase does not change in time), referred to as the dc effect, and the non-stationary regime, known as ac effect. They can be used to describe Josephson effects in both superfluid bosonic liquids like ^{4}He, superfluid fermionic liquids like ^{3}He [70], and in superconductors [13, 58, 57].

1.2 Superfluid hydrodynamics and equation for the order parameter

In the previous section, we showed that phase and number are conjugate operators, and that, as a consequence of phase coherence (i.e. the presence of a finite BEC fraction), the equations for their mean values are meaningful and given by Eqs. (1.8) and (1.9). Let's consider the generalization of Eq. (1.9) to a non uniform system, with the assumption that the energy is a functional of the particle density $n(\boldsymbol{r})$ only. This means in particular that we are neglecting the quantum kinetic energy coming from the curvature of the density, known as quantum pressure, which is related to zero point motion and not to particle transport. This approximation, in the context of dilute BECs, is often referred to as Thomas-Fermi approximation.

It is clear then that this local density approximation will be valid when the density variations we want to describe are sufficiently slow. Thus we can write:

$$\frac{\partial\phi(\boldsymbol{r},t)}{\partial t} = -\frac{1}{\hbar}\frac{\delta E}{\delta n(\boldsymbol{r})} = \frac{\partial\varepsilon(n)}{\partial n}, \tag{1.18}$$

[4]here $dN/dt \neq 0$ because we are considering only two coupled superfluid volumes. A completely stationary situation can be obtained in presence of a current generator [7], or by considering an two semi-infinite reservoirs (see below)

where $\varepsilon(n)$ is the energy density. If we want to consider a superfluid having a non-zero velocity field, the energy density can be calculated using a Galilean transformation, based on the approximation that the fluid can be considered locally uniform, which restricts this derivation to slowly varying velocity field [76, 72]. The energy density is then:

$$\varepsilon(n) = \varepsilon_0(n) + \frac{1}{2}mnv^2, \tag{1.19}$$

where $\varepsilon_0(n)$ is the internal energy of the fluid, and $\boldsymbol{v}(\boldsymbol{r})$ is the local superfluid velocity field. Notice that we are always assuming that the system is at zero temperature, otherwise, the contribution of thermal excitations to the internal energy would need to be included, as well as the Galilean term $\boldsymbol{p} \cdot \boldsymbol{v}$, where $\boldsymbol{p}$ is the momentum carried by the excitations. Therefore, when both the density and the superfluid velocity are slowly varying, by taking the gradient of Eq. (1.18), we get:

$$m\frac{\partial \boldsymbol{v}(\boldsymbol{r},t)}{\partial t} = -\boldsymbol{\nabla}\left(\mu_0(n) + \frac{1}{2}mv^2\right), \tag{1.20}$$

where we used the identity (1.15). Here $\mu_0(n) = \frac{\partial \varepsilon_0}{\partial n}$ is the local chemical potential. The above equation is exactly equivalent to the Euler equation for non-viscous classical isentropic flow [46], plus the irrotationality condition:

$$\boldsymbol{\nabla} \times \boldsymbol{v} = \frac{\hbar}{m}\boldsymbol{\nabla} \times \boldsymbol{\nabla}\phi = 0, \tag{1.21}$$

coming from the fact that superfluid currents are induced by phase gradients. Eq. (1.20), plus the continuity equation:

$$\frac{\partial n}{\partial t} + \boldsymbol{\nabla}(n\boldsymbol{v}) = 0, \tag{1.22}$$

expressing the conservation of mass, constitute what we shall call the superfluid hydrodynamic equations. It's interesting to observe that the conditions allowing for such description of a superfluid are much different from the ones allowing for the same description of an ordinary liquid. Indeed, in the case of a superfluid, hydrodynamic approximation assumes that the variations of the density and velocity field we want to consider are slower than the characterstic length/time scale over which the superfluid density changes. These characteristic scales are set by the so called healing length and by the chemical potential, which are both depending on the particle interactions. On the other hand, the usual assumption underlying a hydrodynamic description of an ordinary liquid is that the collisions between particles are frequent enough that thermal equilibrium is locally achieved much faster that the time scale of the variation we want to describe, and also that these variations take place on a length scale much larger than the smallest distance over which thermal eqilibrium is possible.

The hydrodynamic equations can be applied to strongly correlated superfluids, like helium II, once the equation of state is known. A less widely applicaple but much simpler approach is to solve equations for the order parameter. The definition of superfluidity given above is indeed based on the existence of a non-zero order parameter (1.1). As shown by Ginzburg and Landau, one can write phenomenological equations for the order parameter which can be used to describe the system's stationary properties, and the second order phase transition to the superfluid state. The Ginzburg-Landau (GL) equation for an order parameter $\Psi(\boldsymbol{r})$ of an uncharged system reads:

$$\xi^2\nabla^2\Psi(\boldsymbol{r}) + (\frac{|\Psi(\boldsymbol{r})|^2}{\Psi_0^2} - 1)\Psi(\boldsymbol{r}) = 0, \tag{1.23}$$

where Ψ_0 is a fixed value of the order parameter (like the bulk value of the density at some temperature), and ξ is the characteristic distance over which the order parameter varies, corresponding to the healing length introduced above. Within GL theory, the healingh length diverges close to the critical temperature T_c like $|T - T_c|^{-1/2}$. As we have seen, the modulus of the order parameter describes the condensate fraction, which can involve only a tiny (but finite) part of the superfluid. Therefore, when applied to superfluid helium or superconductors, the GL equation is sufficiently accurate only in some temperature region close to the critical transition temperature T_c. As we shall see later, in the case of ultracold gases of bosonic atoms, the equation for the order parameter can be derived from the full many-body theory in the dilute limit, and proves very accurate to describe both stationary and also the dynamical properties of dilute BEC.

1.3 Current-phase relation and weak links

In general, Josephson effects are observed with two coupled superfluid[5] reservoirs, forming what is usually called a Josephson junction. We have seen from Eq. (1.10) that a constant phase gradient across a superfluid system corresponds to a stationary current, and this is known as dc Josephson effect. It is clear that there will be a relation between the current J flowing across the junction and the phase difference $\Delta\phi$ between the two macroscopic reservoirs. The current-phase relation $J(\Delta\phi)$ also determines the dynamics in a Josephson junction once the phase evolution $\Delta\phi(t)$ is known, that is, by Eq. (1.13), once the chemical potential difference between the two reservoirs is known as a function of time. The supercurrent oscillation in time in presence of a chemical potential difference is generically referred to as ac Josephson effect. Therefore, the current-phase relation provides fundamental informations about the superfluid transport between

[5] unless specified, by superfluid we will indicate both superfluid helium and superconductors

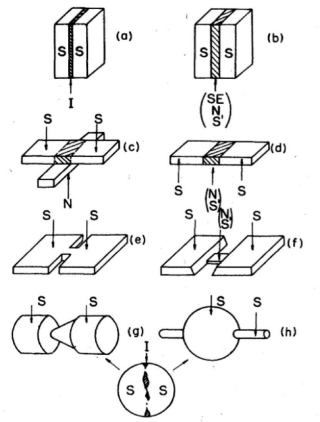

Fig. 1.1: Various kinds of superconducting junctions. Figure taken from [57]. (a) Tunnel junction. (b)-(h) Weak links: (b) sandwich, (c) proximity effect bridge, (d) ion-implanted bridge, (e) Dayem bridge, (f) variable thickness bridge (g) point contact (h) blob-type junction. Here S stands for superconductor, S' for a superconductor with lower critical current, N for normal metal, SE for semiconductor, and I for insulator.

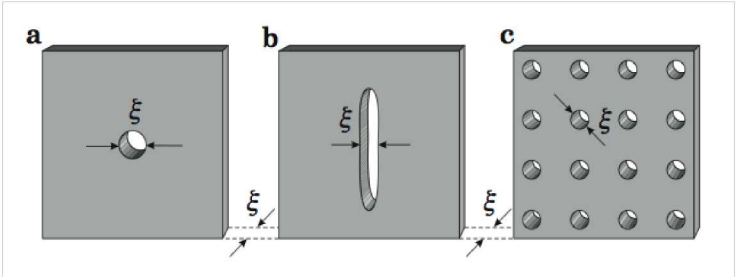

Fig. 1.2: Superfluid weak links. Figure taken from [86]. (a) Single aperture. (b) Slit. (c) Aperture array. Here ξ indicates the superfluid healing length.

the two reservoirs. It will depend on the particular characteristics of the junction, as well as, of course, on the equation of state of the fluid under consideration.

The coupling between two superfluid reservoirs can be realized in different ways, the most famous of which is the tunnelling junction, originally used to observe Josephson effects, where the

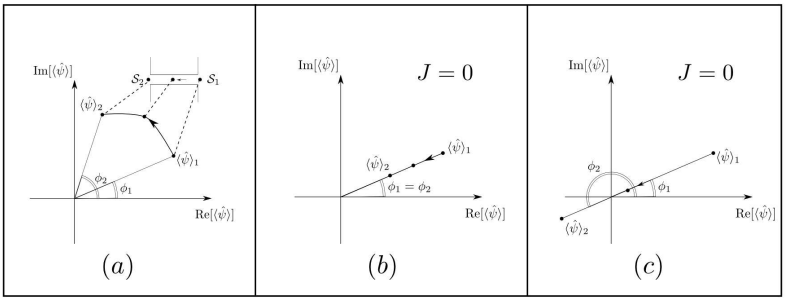

Fig. 1.3: Change of the order parameter $\langle\hat{\psi}(\boldsymbol{r})\rangle$ across the junction between two superfluid reservoirs $\mathcal{S}_1$ and $\mathcal{S}_2$. The plot show trajectories in the complex plane. The figure is made using Fig.3 in [57]. (a) Typical trajectory corresponding to current $J \neq 0$. (b) Trajectory with no phase change $\Delta\phi = 0$, $J = 0$. (b) Trajectory with $\Delta\phi = \pi$, $J = 0$. Here the modulus of the order parameter is zero inside the junction.

two reservoirs are connected by a region where conduction is possible only through tunnelling. Such configuration was realized originally using an insulating film between two superconductors, as shown in Fig. 1.1(a) [57]. However, Josephson effects can be also studied using non-tunnelling junctions, which can all be gathered in the "weak link" category. This broad class essentially indicates a constriction for the particle flow between the two reservoirs, that is, a portion of a superfluid/superconductor which has different transport properties with respect to the rest of the system [57]. A weak link has many implementations in superconductors (Fig. 1.1(b)-(h)), among which the Dayem bridge configuration (Fig. 1.1(e)) most closely resembles the superfluid helium weak link, where the connection between the two reservoirs is provided by apertures on impenetrable walls, as shown in Fig. 1.2 [70, 97].

The current-phase relation $J(\Delta\phi)$ has some general properties which do not depend on the particular fluid equation of state, or the choice of the junction [57]. First of all, since a superfluid must possess a non-zero order parameter, defined in Eqs. (1.1)-(1.5), gauge invariance implies that the current-phase relation is 2π-periodic:

$$J(\Delta\phi) = J(\Delta\phi + 2\pi\nu),\ \nu \in \mathbb{Z}. \tag{1.24}$$

Second, the $J(\Delta\phi)$ must be zero in absence of phase gradients across the junction, that is, when $\Delta\phi = 0$ or $\Delta\phi = \pi$, which both correspond to no change in the phase angle across the junction,

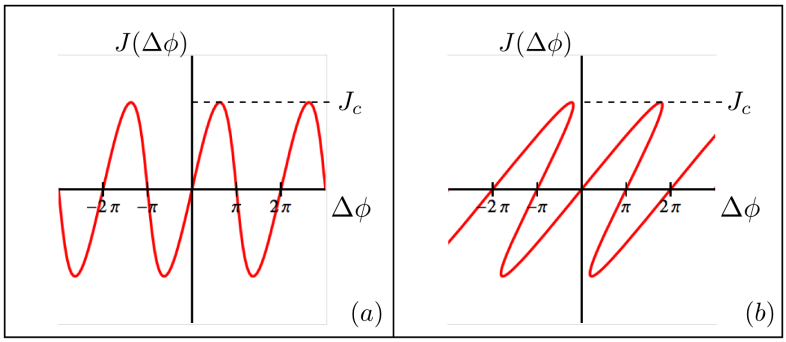

Fig. 1.4: Examples of current-phase relations $J(\Delta\phi)$. (a) Single-valued diagram. (b) Multivalued diagram.

as depicted in Fig. 1.3. Thus:

$$J(\nu\pi) = 0, \ \nu \in \mathbb{Z}. \tag{1.25}$$

Since, as evident from Eq.(1.12), a change in sign of the phase difference produces just an equal but reversed supercurrent, then $J(\Delta\phi)$ must be symmetric with respect to the origin:

$$J(\Delta\phi) = -J(-\Delta\phi). \tag{1.26}$$

Two typical examples of current-phase relations are shown in Fig. 1.4. One important feature characterizing a current-phase diagram is the critical current J_c, that is, the highest stationary current possible in that particular junction. This is related to the problem of superfluid instability which will be the object of chapter 2. Fig. 1.4(a) depicts a single-valued current-phase relation, while Fig. 1.4(b) shows a multivalued one. The latter category, often referred to as reentrant diagrams, is characterized by the existence of more than one value of the current corresponding to the same phase difference. Reentrant phase diagrams, as we shall discuss, are very interesting since they give rise to a completely different dynamics of the ac Josephson effect.

1.4 Two extreme cases: ideal Josephson junction and hydrodynamic junction

We will now describe the current-phase relation for two particular kinds of junction which show two completely opposite transport regimes: an ideal Josephson junction and a hydrodynamic junction.

The essence of an ideal Josephson junction is very well captured by a simple model. Consider two coupled superfluid reservoirs $\mathcal{S}_1$ and $\mathcal{S}_2$, described by spatially constant order parameters $\psi_j = f_j e^{i\phi_j},\ j = 1, 2$, joined by a junction where superfluidity is somehow suppressed, so that both order parameters are very small in this region. This implies that inside the junction the kinetic energy dominates over other energy scales. We can see this by taking the GL equation (1.23), and considering a junction region of size d, so that the kinetic term in the equation is of order $(\xi/d)^2$, where ξ is the bulk healing length and Ψ_0^2 the corresponding density. If $d \ll \xi$, very narrow junction, the kinetic term dominates over all the other terms, so that for the order parameter Ψ inside the barrier region we can simply solve the equation:

$$\nabla^2 \Psi(\boldsymbol{r}) = 0, \tag{1.27}$$

with the boundary conditions in the bulk at the two sides of the junction [6] $\Psi(\boldsymbol{r}) = f_j e^{i\phi_j},\ \boldsymbol{r} \in \mathcal{S}_j$. This problem has a unique solution [8]:

$$\Psi(\boldsymbol{r}) = \chi(\boldsymbol{r}) f_1 e^{i\phi_1} + (1 - \chi(\boldsymbol{r})) f_2 e^{i\phi_2}, \tag{1.28}$$

where $\chi(\boldsymbol{r})$ is a real function satisfying the equation $\nabla^2 \chi(\boldsymbol{r}) = 0$ with boundary conditions $\chi(\boldsymbol{r}) = 1,\ \boldsymbol{r} \in \mathcal{S}_1,\ \chi(\boldsymbol{r}) = 0,\ \boldsymbol{r} \in \mathcal{S}_2$. The kinetic energy can therefore be expressed as $E = E_{\mathrm{Q}} + E_{\mathrm{J}}$, where $E_{\mathrm{Q}} = (\hbar^2/2m) \int d^3r (\nabla f)^2$ is the quantum pressure, and $E_{\mathrm{J}} = (\hbar^2/2m) \int d^3r f^2 (\nabla \phi)^2$ is the coupling energy (see Eq. (1.10)). Here f is the modulus of Ψ, and ϕ its phase. We can then calculate the current using Eq. (1.11), to get:

$$\boldsymbol{J} = \frac{1}{\hbar} \frac{\delta E_{\mathrm{J}}[f, \boldsymbol{\nabla}\phi]}{\delta \boldsymbol{\nabla}\phi} = \frac{\hbar}{m} f^2 \boldsymbol{\nabla}\phi = \frac{\hbar}{m} f_1 f_2 (\boldsymbol{\nabla}\chi) \sin(\Delta\phi). \tag{1.29}$$

The current at every point inside the link depends sinusoidally on the total phase difference $\Delta\phi$ across the junction, and so will do the total flux across the junction.

$$J(\Delta\phi) \propto \sin(\Delta\phi) \tag{1.30}$$

This sinusoidal current-phase relation is a signature of the ideal Josephson regime. This was the situation in which ac josephson oscillations where first observed with superconducting SNS junctions, where, under the influence of an external drive, the current was observed to oscillate sinusoidally during time [57]. What we have shown above tells us that, in order to have ideal Josephson regime, it is not actually necessary to have a non-superfluid layer separating the two

[6] Since we refer here to a general three dimensional problem, a further boundary condition must be imposed. Namely, that the current component normal to the boundary of the system must be zero [57].

superfluid reservoirs which would then be coupled by tunneling, but it is sufficient to have a junction where the order parameter is strongly suppressed. We have seen that in this case the coupling happens through the interference of the two wavefunctions (Ψ is indeed a superposition of two order parameters) corresponding to the two reservoirs, which overlap inside the junction. Therefore, ideal Josephson sinusoidal oscillations would be possible also in a generic weak link where there is no tunnelling transport through a barrier.

A hydrodynamic junction is instead realized when the healing length is much smaller than all other length scales in the system, which allows to describe the junction with the Eqs. (1.20) and (1.22), thereby neglecting the quantum pressure term. In a superfluid, this is possible when the interactions among the particles are strong enough. In this situation, tunneling transport through a barrier is obviously forbidden. Therfore, a hydrodynamic junction must be realized using a weak link.

Let us consider, as an example, two superfluid reservoirs $\mathcal{S}_1$ and $\mathcal{S}_2$ connected by an orifice of radius R [7], the typical weak link used with superfluid helium. Assume that the fluid is incompressible, so that the density n is constant all over the system, and let the phases in the bulk of $\mathcal{S}_1$ and $\mathcal{S}_2$ be ϕ_1 and ϕ_2, respectively. The continuity equation (1.22) becomes, in the stationary case, simply:

$$\boldsymbol{\nabla} \boldsymbol{v} = \nabla^2 \phi = 0, \tag{1.31}$$

where we used the identity (1.15). Using oblate spheroidal coordinates, one can solve the problem analytically, to get the total flux across the orifice:

$$J = \int_A d\sigma v_\perp = 2n \frac{\hbar R}{m} \Delta\phi, \tag{1.32}$$

where A is the area of the orifice, $v_\perp$ is the velocity component normal to the orifice plane, and $\Delta\phi = \phi_1 - \phi_2$. This shows that a hydrodynamic junction in characterized by a linear current phase relation which, including the periodicity required by gauge invariance, reads:

$$J(\Delta\phi) = \frac{2n\hbar R}{m}(\Delta\phi + 2\nu\pi), \ \nu \in \mathbb{Z}. \tag{1.33}$$

This purely hydrodynamic current-phase relation does not have the property (1.25), since $J(\Delta\phi)$ crosses zero only in correspondence of multiples of 2π. As we shall discuss later, this is due to the fact that the hydrodynamic approximation neglects the quantum pressure, thereby missing one branch of the current-phase diagram.

This purely hydrodynamic current-phase relation is an extreme case of the reentrant diagram category introduced above. As anticipated, this class of hydrodynamic junctions behaves in

a completely different way under the influence of an external drive (ac Josephson effect), with respect to tunnelling junction. Generally speaking, a tunnelling junction is such that the ac effect can be thought of as an adiabatic change of phase difference, induced by the chemical potential difference according to the Josephson-Anderson equation (1.13). In this way, running through equilibrium states, the system moves smoothly along the whole sinusoidal phase diagram, and correspondingly the current oscillates back and forth with a frequency fixed by $\Delta\mu$. On the other hand, looking for instance at the reentrant current-phase relation in Fig. 1.4(b), we see that no such adiabatic evolution is possible, since the phase difference can be increased smoothly only up to a critical value at which, in order to further increase $\Delta\phi$, the current must jump. This jump takes place through the very important phase slip mechanism, first discussed by Anderson [7], by which the phase difference across the junction changes by 2π, and the current drops by a quantized amount. Microscopically, the 2π phase change is due to a vortex crossing the flow, which takes the energy away from the superfluid current. Phase slippage is a fundamental mechanism for superfluid flow dissipation, and we will discuss it in larger detail in chapter 2.

The ideal ac Josephson effect, characterized by the sinusoidal oscillation of the current, was much more difficult to observe with helium than with superconductors. The reason for this being the extremely small healingh length (order of the the Å), making it very difficult to suppress superfluidity within the orifice. In other words, helium is typically "very hydrodynamic". Indeed, the first macroscopic quantum interference experiment demonstrating an ac Josephson effect was performed in the hydrodynamic phase-slip regime (reentrant current-phase relation) by Varoquaux, Avenel and Meisel in 1987 [97], using ^{4}He flowing through an orifice. The ac effect in the ideal josephson regime, with a sinusoidal current-phase relation, was first observed one year later with ^{3}He [10]. Ten years after, Packard's group observed the full crossover between ideal Josephson and hydrodynamic regimes using ^{3}He [11], and almost after ten other years using ^{4}He [33].

1.5 Superfluid dilute bosonic gases and the Gross-Pitaevskii equation

Let us now turn to our system of interest, that is, ultracold dilute gases of bosonic atoms. As anticipated, due to their diluteness, these so called BECs allow for a simple theoretical description, since i) at the typical temperatures the condensate fraction is very large, and it is

thus reasonalble to neglect quantum and thermal fluctuations, ii) the interatomic interactions are governed by two-body collisions at low energy, and characterized only by the s-wave scattering length a_s. Under this conditions, the equation for the oder parameter ψ can be derived from the full many-body Hamiltonian, as we shall briefly outline next [75, 74, 23, 76, 72]. The Heisenberg equation for the field operator $\hat{\psi}$ describing N interacting bosons of mass m reads:

$$i\hbar\frac{\partial}{\partial t}\hat{\psi}(\boldsymbol{r},t)=\left[-\frac{\hbar^2}{2m}\nabla^2+V_{\rm ext}(\boldsymbol{r})+\int d^3r'\hat{\psi}^\dagger(\boldsymbol{r}',t)V(\boldsymbol{r}'-\boldsymbol{r})\hat{\psi}(\boldsymbol{r}',t)\right]\hat{\psi}(\boldsymbol{r},t), \tag{1.34}$$

where $V_{\rm ext}$ is the external potential while V is the interaction potential. Writing the field operator as

$$\hat{\psi}(\boldsymbol{r},t)=\psi(\boldsymbol{r},t)+\delta\hat{\psi}(\boldsymbol{r},t)\simeq\psi(\boldsymbol{r},t), \tag{1.35}$$

where the last equality comes from neglecting the depletion of the condensate according to i). The approximation (1.35) is consistent with the use of an effective potential to substitute the bare interaction potential V:

$$V(\boldsymbol{r}-\boldsymbol{r}')\to g\delta(\boldsymbol{r}-\boldsymbol{r}'), \tag{1.36}$$

where $\delta(\boldsymbol{r})$ is the Dirac delta, and $g=4\pi\hbar^2a_s/2m$ is the effective interaction coupling for the relevant scattering processes as of ii). Then by substituting Eq. (1.35) in the Heisenberg equation (1.34), we get the Gross-Pitaevskii (GP) mean-field equation for the order parameter ψ:

$$i\hbar\frac{\partial}{\partial t}\psi(\boldsymbol{r},t)=\left[-\frac{\hbar^2}{2m}\nabla^2+V_{\rm ext}(\boldsymbol{r})+g|\psi(\boldsymbol{r},t)|^2\right]\psi(\boldsymbol{r},t). \tag{1.37}$$

The diluteness condition, which is necessary for the above approximations to be valid, is enforced when the average number of particles in a scattering volume $|a_s|^3$, given by $\bar{n}|a_S|^3$ with $\bar{n}$ the average density, is sufficiently smaller than one. It is important to stress that diluteness does not imply small deviations from the ideal gas behavior, since the ratio of the interaction term to the kinetic term in the GP equation is estimated by Na_s/l, where l is the typical length scale set by the external potential V_{ext} which confines the atoms. This ratio can be large even in the dilute limit, with typical number of atoms ranging from 10^3 to 10^6.

1.6 Current-phase relation of a dilute ultracold bosonic gas flowing through a weak link

This section is based on the work: **Current-Phase relation of a Bose-Einstein condensate flowing through a weak link**, F.P., L. A. Collins [*Theoretical Division, Mail Stop B214, Los Alamos National Laboratory, Los Alamos, New Mexico*

87545], and A. Smerzi [*INO-CNR, BEC Center, and Dipartimento di Fisica, Via Sommarive 14, 38123 Povo, Trento, Italy*], published in Phys. Rev. A **81**, 033613 (2010).

As discussed in section 1.3, the study of the current phase relation provides very important informations about the nature of transport of a superfluid across a given junction. While the are several measurement of the current-phase relation performed with superfluid helium and superconductors, the effort is still to be made using dilute BECs. In the context of ultracold dilute gases, raising a repulsive penetrable barrier across the flow, created for instance using a laser beam, yields a weak link configuration. For instance, with BECs, Josephson effect(s) have been theoretically studied [89, 65, 102, 4] and experimentally demonstrated using multiple well traps [18, 3, 55].

We have seen that a weak link configuration can be modelled very generally upon taking a portion of a superfluid to have different conduction properties with respect to the rest of the system. Two pieces of superconductor joined by a third superconducting region with a smaller coherence length provide one example, whose current-phase relation in one dimension has been studied with the GL equation [12]. The latter has also been employed to study the current-phase relation of a one dimensional superconducting weak link, modelled by an effective external delta potential [91]. With ultracold atoms, on the theoretical site, the current-phase relation has been studied for a flow through a repulsive square well with fermions across the BCS-BEC crossover by means of one dimensional Bogoliubov-de Gennes equations [92], for weak barriers with bosons in a local density approximation (see section 2.2), and for fermions on the BEC side of the crossover using a nonlinear Schrödinger equation approach [5].

1.6.1 Overview of the main results

Our goal is to study the current-phase relation of a dilute BEC flowing through a repulsive barrier of variable size and strength. The weak link configuration, and in turn the current-phase relation, is fixed by the barrier height with respect to the chemical potential and by the barrier width with respect to the healing length. We solve a one-dimensional GP equation, but the results presented in the following are not just relevant for ultracold dilute bosonic gases, but also include the essential features of current-phase relations of superconducting or superfluid He-based weak links, when governed by the Ginzburg-Landau equation. For any barrier width, we find that in the limit of zero barrier height, the current phase relation tends to $j(\delta\phi) = c_\infty \cos(\delta\phi/2)$,

with c_∞ being the bulk sound velocity. We shall see that this corresponds to the phase across a grey soliton at rest with respect to the barrier. On the other hand, if the barrier height is above the bulk chemical potential at zero current, the limit of tunneling flow is reached either when the barrier height is much bigger than the bulk chemical potential at zero current or when the barrier width is much larger than the bulk healing length. In this regime, we recover the the usual Josephson sinusoidal current-phase relation $j(\delta\phi) = j_{\rm jos}\sin(\delta\phi)$, and obtain an analytical expression for the Josephson critical current $j_{\rm jos}$ as a function of the weak link parameters. For barriers wider than the healing lenght inside the barrier region, we observe two families of multivalued current-phase relations. The first family of reentrant diagrams corresponds to the one introduced before (see Fig. 1.4(b)), already studied and discovered for superconductors and superfluid helium. It is characterized by a positive slope of the current when the phase difference is close to π, thereby reaching a phase difference larger than π at least for small currents. The second family of multivalued diagrams, appearing at a smaller barrier height, has instead a negative slope of the current close to π, and in some cases can remain within the $0-\pi$ interval across the whole range of currents. As discussed in sections 1.3 and 1.4, the first kind of reentrant behavior was proven to be connected to the onset of phase-slippage in the ac Josephson effect, as opposed to the sine-like current oscillations observed in the ideal Josephson regime. Therefore, the second kind of reentrant current-phase relation discovered here might be connected to the appearance of new features in the ac Josephson dynamics. We finally illustrate how the multivaluedness characterizing both families of reentrant current-phase relations is always due to the competition between a hydrodynamic component of the flow and a nonlinear-dispersive component, the latter due to the presence of a soliton inside the barrier region. The two components can coexist only for barriers wide enough to accomodate a soliton inside. In this spirit, we develop a simple analytical model which describes very well reentrant regimes of current-phase diagrams.

1.6.2 The model

We consider a dilute BEC flowing through a repulsive rectangular potential barrier. We look for stationary solutions of the one-dimensional GP equation for the order parameter $\Psi(x)$:

$$-\frac{\hbar^2}{2m}\partial_{xx}\Psi + V_{\rm ext}(x)\Psi + g|\Psi|^2\Psi = \mu\Psi, \tag{1.38}$$

where $\Psi(x) = \sqrt{n(x)}\exp[i\phi(x)]$ is the complex order parameter of the condensate, μ is the chemical potential, and $a_s > 0$. Here n is the condensate density which, for dilute BECs, will be

very close to the total atom density (see section 1.5). The order parameter phase $\phi(x)$ is related to the superfluid velocity via $v(x) = (\hbar/m)\partial_x\phi(x)$ (see Eq. (1.15)). The piecewise constant external potential describes the rectangular barrier of width $2d$ and height V_0:

$$\begin{cases} V_{\rm ext}(x) = V_0 & , \ |x| \leq d \ , \\ V_{\rm ext}(x) = 0 & , \ |x| > d \ . \end{cases} \tag{1.39}$$

We consider solutions of Eq. (1.38) which are symmetric with respect to the point $x = 0$, thereby discarding situations in which a reflected wave is present. A zoo of solutions for both attractive and repulsive square wells is presented in [48]. Symmetric solutions in the presence of a barrier exist due to the nonlinearity in the GPE. Indeed, solutions of the linear Schrödinger equation in presence of a repulsive barrier have always a reflected wave upstream. This point illustrates quite well how nonlinearities, and in turn interactions, are crucial for the existence of stable stationary currents in presence of obstacles. This aspect will be discussed in more detail in chapter 2.

We further restrict our analysis to subsonic flows $v_\infty \leq c_\infty$, with $c_\infty = \sqrt{gn_\infty/m}$ being the sound velocity for a uniform condensate of density n_∞. As boundary conditions, we fix the condensate density n_∞ and velocity v_∞ at $x = \pm\infty$, thereby determining the chemical potential $\mu = gn_\infty + \frac{1}{2}mv_\infty^2$. Using the relation $\Psi = \sqrt{n}\exp[i\phi]$, Eq. (1.38) can be split into a continuity equation, enforcing a spatially constant current $j = n(x)v(x) = n_\infty v_\infty$, and an equation for the density:

$$\mu = -\frac{\hbar^2}{2m}\frac{\partial_{xx}\sqrt{n}}{\sqrt{n}} + \frac{mj^2}{2n^2} + V_{\rm ext}(x) + gn \ , \tag{1.40}$$

where we have used the continuity equation $v(x) = j/n(x)$ to eliminate the velocity. The solution $n(x)$ of Eq. (1.38) is expressed in terms of Jacobi elliptic functions [61, 47, 83, 56, 12]. Due to symmetry, we need only consider half of the space $x > 0$. The solution outside the barrier $x > d$ becomes

$$n_{\rm out}(x) = n_\infty - A_\infty + A_\infty \tanh^2\left[\sqrt{\frac{mg}{\hbar^2}A_\infty}(x-d) + x_0\right] \ , \tag{1.41}$$

where $x_0 = \operatorname{arctanh}\sqrt{(n_d - mv_\infty^2/g)/A_\infty}$, $A_\infty = n_\infty - mv_\infty^2/g \geq 0$, and n_d is the density at the barrier edge $x = d$. The solution inside the barrier $x < d$ is:

$$\begin{cases} n_1(x) = n_0 + A_1\dfrac{\mathrm{sn}^2[b_1x, k_1]}{\mathrm{cn}^2[b_1x, k_1]} & , \Delta \geq 0 \text{ and } A_1 \geq 0 \ , \\ n_2(x) = n_0 + A_2\dfrac{1 - \mathrm{cn}[b_2x, k_2]}{1 + \mathrm{cn}[b_2x, k_2]} & , \text{else} \ , \end{cases} \tag{1.42}$$

where n_0 is the density at $x = 0$,

$$\Delta = (n_0 - 2\tilde{\mu}/g)^2 - \frac{4mj^2}{gn_0} \tag{1.43}$$

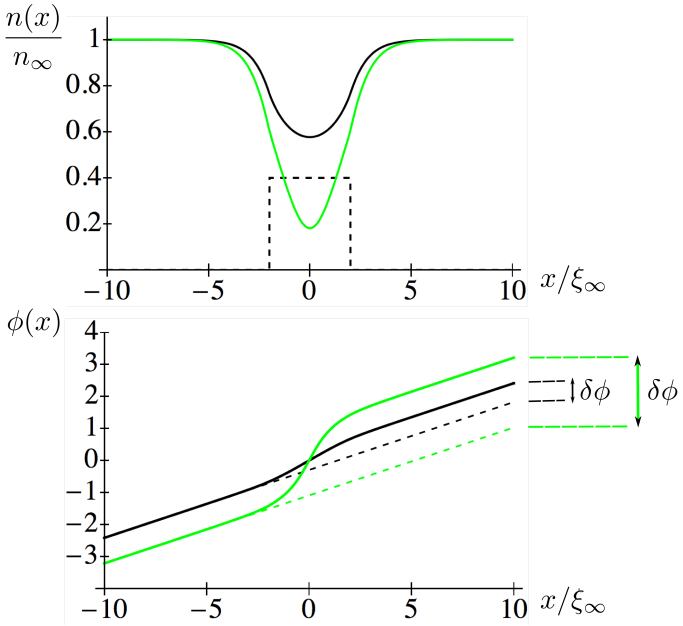

Fig. 1.5: Typical solutions for a barrier with width $2d = 4\xi_\infty$, $V_0 = 0.4gn_\infty$, and $j = 0.3c_\infty n_\infty$. Density (upper panel) and phase (lower panel) as a function of position are shown for both the upper and the lower solution, corresponding to black and green (light gray) solid lines, respectively. Dashed lines in the lower panel correspond to the phase accumulated by a plane wave in absence of barrier.

with

$$\tilde{\mu} = \mu - V_0, \tag{1.44}$$

and $A_1 = 3n_0/2 - \tilde{\mu}/g - \sqrt{\Delta}/2$, $A_2 = \sqrt{2(n_0^2 - n_0\tilde{\mu}/g + mj^2/2gn_0)}$. Finally, the parameters entering the Jacobi sines sn and cosines cn are $b_1 = \sqrt{mg(\sqrt{\Delta} + A_1)/\hbar^2}$, $k_1 = (\sqrt{\Delta}/(\sqrt{\Delta} + A_1))^{1/2}$, and $b_2 = \sqrt{4mgA_2/\hbar^2}$, $k_2 = ((A_2 - A_1 - \sqrt{\Delta}/2)/2A_2)^{1/2}$.

Given n_∞ and v_∞, we are left with two free parameters: n_0 and n_d. These are determined by matching the density and its derivative at the barrier edge $x = d$. First, the derivative matching condition, enforced using the first integral of Eq. (1.40), allows us to write n_d as a function of n_0 for any value of Δ:

$$n_d = \frac{g}{2V_0}\left[n_\infty^2 + n_0^2 + \frac{mv_\infty^2 n_\infty}{g}(2 - \frac{n_\infty}{n_0}) - 2\frac{\tilde{\mu}}{g}n_0\right] . \tag{1.45}$$

The density matching equation $n_d = n_i(d)$ $(i = 1, 2)$ is then solved by a numerical root finding method, yelding n_0.

Two bounded solutions are always found, an example is given in the upper panel of Fig. 3.2. In general, the two solutions can both correspond to a positive Δ, both to a negative Δ, or one to a positive and the other to a negative Δ. For a superconductor flowing through a repulsive one dimensional delta potential barrier, it has been shown with GL equation that the two solutions become a plane wave and a soliton when the strength of the barrier goes to zero [91]. With a repulsive square well potential, we find the same behavior for our GP solutions. In the following, the solution which tends to a plane wave for $V_0 \to 0$ will be referred to as "upper solution", while the one tending to a grey soliton will be called "lower solution". The study of the stability of the two solutions would not be made here. This issue has been considered in [31], using GP equation in the case of a repulsive delta potential barrier.

For given barrier parameters V_0 and d, and at a fixed density at infinity n_∞, the solutions exist up to a critical injected velocity $v_\infty = v_c < c_\infty$, at which they merge and disappear. This was also found in the case of a repulsive delta potential in [31]. Similarly, in [48], the same kind of merging was reported for a one-dimensional BEC flow through a repulsive square well, when the width of the latter increases.

1.6.3 Current-phase relation

The current-phase relation $j(\delta\phi)$ only depends on the properties of the weak link, in our case the barrier height V_0 with respect to the chemical potential, and the width $2d$ with respect to the healing length. For a fixed current $j = v(x)n(x)$, the phase difference across the system is calculated using the relation $\phi(x) = \int^x dy(m/\hbar)j/n(y)$ and then renormalized by the phase accumulated by the a plane wave with the same boundary conditions in absence of barrier (see lower panel in Fig. 3.2). Two different values of $\delta\phi$ are found, corresponding to the upper and lower solutions.

In this subsection, we will use dimensionless quantities, employing the chemical potential at zero current gn_∞ as the unit of energy, the bulk healing length $\xi_\infty = \hbar/\sqrt{2mgn_\infty}$ as the unit of length, and $\hbar/gn_\infty$ as the unit of time. Exploiting the symmetry of the system about $x = 0$, the phase difference can be written as

$$\delta\phi_i = \lim_{x\to\infty}\left[\int_0^d dy\frac{j}{n_i(y)} + \int_d^x dy\frac{j}{n_{out}(y)} - \frac{jx}{n_\infty}\right] \ , \ i = 1, 2, \tag{1.46}$$

where the third term is the renormalization coming from the phase difference accumulated by

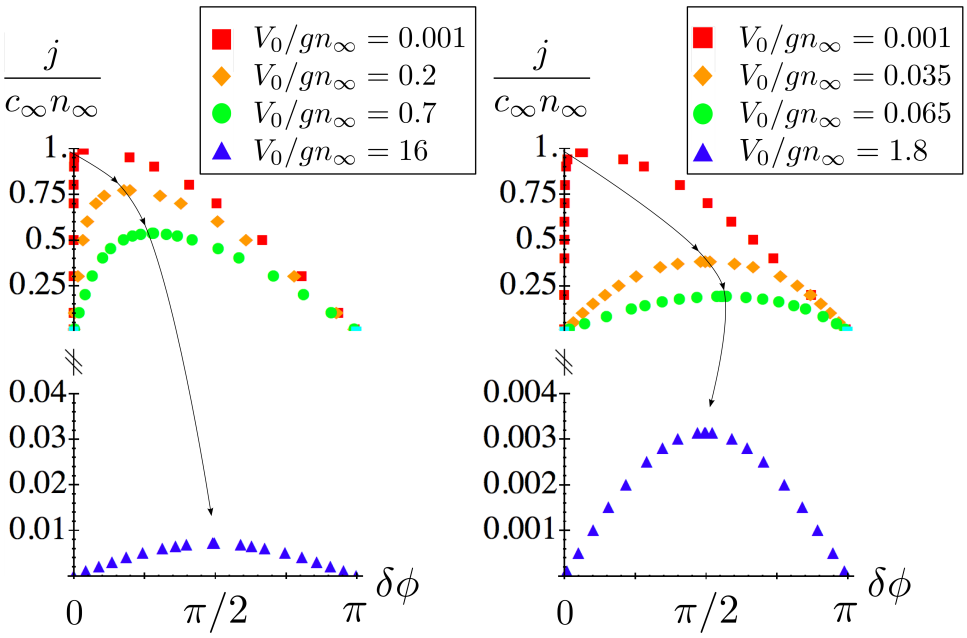

Fig. 1.6: Current-phase relation for a barrier with half width $d = 0.5\xi_\infty$ (left panel) and $d = 3\xi_\infty$ (right panel), for different barrier heights V_0 (see insets). The arrows sketch the behavior of the maximum of the curves upon increasing V_0.

the plane wave in absence of barrier. The limit can be calculated using Eq. (1.41), yielding

$$\delta\phi_i = \int_0^d \frac{j dy}{n_i(y)} - jd + 2\left[\arcsin\left(\frac{j}{\sqrt{2n_i(d)}}\right) - \arcsin\left(\frac{j}{\sqrt{2}}\right)\right]. \tag{1.47}$$

The first two terms in Eq. (1.47) correspond to the phase acquired inside the barrier while the third, which we can call the pre-bulk term, gives the phase accumulated outside the barrier, where the density has not yet reached its bulk value n_∞. For simplicity, we have chosen $n_\infty = 1$.

In Fig. 3.3, the current phase relation is shown for different barrier widths and heights. Each curve has a maximum at the point $(\delta\phi_c, j_c)$, with $j_c = n_\infty v_c$ being the critical current at which the two stationary solutions merge and disappear. The upper solutions constitute the part of the current-phase diagram which connects the maximum with the point $(\delta\phi = 0, j = 0)$, while the lower ones belong to the branch connecting the maximum to the point $(\delta\phi = \pi, j = 0)$.

Indeed, we will now show that, for any d and $V_0 \to 0$, the upper branch tends to a plane wave, while the lower branch tends to a grey soliton. In order to have a finite n_d in this limit,

the term in square brackets in Eq. (1.45) must tend to zero, yielding a cubic equation with two coincident solutions $n_0 = 1$ and a third $n_0 = j^2/2$, where we have set $n_\infty = 1$ for simplicity. For $n_0 = 1$ we have $\Delta = (1 - j^2/2)^2 \geq 0$, corresponding to the plane wave solution $n_1(x) = n_0 = 1$. For $n_0 = j^2/2$ we obtain instead $\Delta = 0$, $A_1 = j^2/2 - 1 < 0$, corresponding to a grey soliton solution $n_2(x) = n_0 + (1 - n_0)\tanh^2(\sqrt{1/2 - n_0/2}x)$. Therefore, in this limit $\delta\phi_1 = 0$ for any j, meaning that the upper branch is actually a vertical line, while for the lower branch we have

$$\cos(\frac{\delta\phi}{2}) = \frac{j}{\sqrt{2}}. \tag{1.48}$$

This curve has a maximum at $\delta\phi_2 = 0$, corresponding to $j = \sqrt{2}$, that is, the sound velocity c_∞ in dimensionless units.

The arrows in Fig. 3.3 sketch the behavior of the maximum of the current-phase relation $(\delta\phi_c, j_c)$ as the height V_0 is increased at a fixed barrier width $2d$. For any width, the current-phase diagram initially takes a cosine-like shape (Eq. (1.48)) when $V_0 \sim 0$ (red squares in Fig. 3.3). On the other hand, it tends to a $\sin(\delta\phi)$ shape for sufficiently large V_0, indicating the entrance in the Josephson regime of tunneling flow, as we shall discuss later (blue triangles in Fig. 3.3). Between these two limits, the behavior of the maximum is determined by the barrier width. For thin barriers ($d \lesssim \xi_\infty$), as shown in the left panel of Fig. 3.3, the point $(\delta\phi_c, j_c)$ moves down-right, reaching the Josephson regime still keeping $\delta\phi_c$ always smaller than $\pi/2$. For sufficiently wider barriers instead, during the down-right displacement of the maximum $\delta\phi_c$ is able to reach values larger than $\pi/2$ above some V_0. The maximum then moves down-left to finally enter the Josephson regime, as shown in the right panel of Fig. 3.3. We note that in this way, while V_0 is increased, the phase $\delta\phi_c$ takes the value $\pi/2$ twice, but only the second time entering the Josephson regime with a sinusoidal current-phase relation. The first time (orange diamonds in the right panel of Fig. 3.3) the flow is not yet in the tunneling regime since V_0 is much smaller than the chemical potential. Indeed, the current-phase relation is symmetrical with respect to $\pi/2$, but not sinusoidal.

1.6.4 Ideal Josephson regime

As described in the previous subsection, for strong enough barriers the flow enters the tunneling regime, and the current-phase relation takes a sinusoidal form. Next, we will analytically describe this behavior, deriving a relation between the Josephson critical current and the barrier parameters V_0 and d. Since we are now interested in tunneling flows, we will take $V_0 > gn_\infty$ and will show that the Josephson regime is attained by either increasing the barrier height V_0 or its

width $2d$.

Since in this regime the injected velocity of a stationary flow v_∞ must be much smaller than the sound velocity c_∞, we can neglect the kinetic energy term $mv_\infty^2/2$ in the chemical potential, which can thus be written as

$$\tilde{\mu} \simeq gn_\infty - V_0 < 0. \tag{1.49}$$

Moreover, the density inside the barrier n_0 being exponentially small, we can write $\Delta \simeq (2\tilde{\mu}/g)^2 - s > 0$, with $s = 4(n_0\tilde{\mu} + mj^2/n_0)/g$, where we have neglected n_0^2. Therefore, both the upper and lower solutions are of the kind $n_1(x)$, with $A_1 \simeq n_0 - mj^2/2n_0\tilde{\mu}$, $b_1 \simeq \sqrt{2m|\tilde{\mu}|/\hbar^2}$, and $k \simeq 1$. The density in the Josephson regime has thus the form

$$n_{\rm jos}(x) = n_0 + (n_0 + \frac{mj^2}{2n_0|\tilde{\mu}|}) \sinh^2\left(\sqrt{\frac{2m}{\hbar^2}|\tilde{\mu}|}\ x\right). \tag{1.50}$$

In order to write the density matching equation $n_d = n_{\rm jos}(d)$, we approximate n_d by discarding both n_0^2 and $2mv_\infty^2 n_\infty/g$ in Eq. (1.45), obtaining a quadratic equation for n_0. Further assuming that $\sinh^2\sqrt{\frac{|\tilde{\mu}|}{\epsilon_d}} \gg 1$, with $\epsilon_d = \hbar^2/2md$ being the kinetic energy associated with the barrier length scale d, the solutions of the above equation are of the form $n_0^{+/-} = \bar{n}_0(1 \pm \sqrt{1-q})$ with $\bar{n}_0 = (gn_\infty/4V_0)n_\infty/\sinh^2\sqrt{|\tilde{\mu}|/\epsilon_d}$, and $q = mj^2/2\bar{n}_0^2|\tilde{\mu}|$.

The Josephson critical current corresponds to the merging of the two solutions at $q = 1$, and reads

$$j_{\rm jos} = n_\infty\sqrt{\frac{2|\tilde{\mu}|}{m}}\frac{gn_\infty}{V_0}\mathrm{e}^{-2\sqrt{|\tilde{\mu}|/\epsilon_d}}, \tag{1.51}$$

where we have used $\sinh(x) \simeq \exp(x)/2$, for $x \gg 1$. The critical velocity for a bosonic and fermionic superfluid flowing through a repulsive square well has been calculated in the work we will treat in section 2.2 within the local density approximation (for BEC case see also [54]). Analytical expressions for the critical current of a BEC flow were found for both slowly varying and weak barriers [31]. Eq. (1.51) thus enriches the above set of analytical results by providing the critical current for strong barriers of any width.

Finally, we calculate the current-phase relation using Eq. (1.47). Since $j_{\rm jos}$ is exponentially small, only the first term in Eq. (1.47) contributes, and the integral can be performed analytically to obtain:

$$\delta\phi^+ = \arcsin\left(\frac{j}{j_{\rm jos}}\right)\ , \delta\phi^- = \pi - \arcsin\left(\frac{j}{j_{\rm jos}}\right). \tag{1.52}$$

We have thus recovered the sinusoidal current-phase relation characterizing an ideal Josephson regime of tunneling flow.

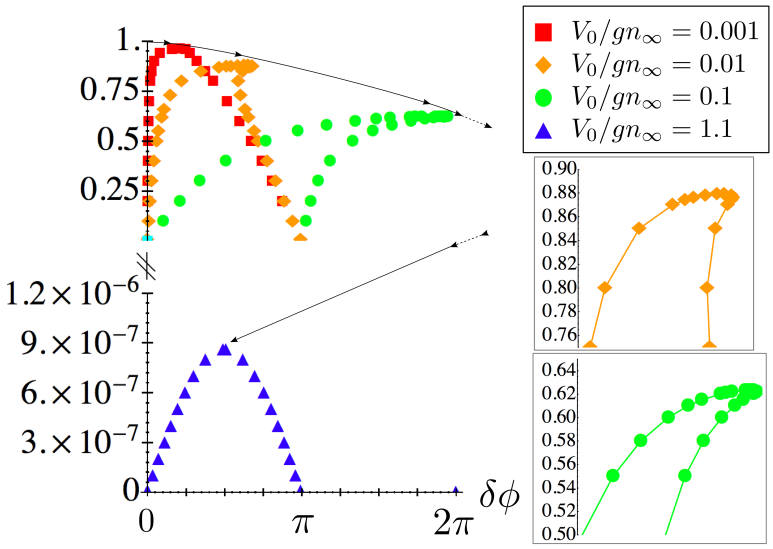

Fig. 1.7: Current-phase relation in the reentrant regime $d = 20\xi_\infty$, for different barrier heights V_0 (see uppermost inset). Middle and lowermost insets show in more detail the shape of the diagram close to the critical point. The arrows sketch the behavior of the maximum of the curves upon increasing V_0.

It is important to pinpoint the conditions for having ideal Josephson transport: i) the barrier height must be larger than the chemical potential, as expressed by Eq. (1.49), valid when the bulk velocity is much smaller than the sound speed, and ii) the following condition must be verified:

$$V_0 - gn_\infty \gg \epsilon_d, \tag{1.53}$$

that is, the height of the barrier with respect to the bulk chemical potential must be much larger than the kinetic energy associated with the density modulation due to the barrier itself. The ideal Josephson limit, once condition (1.49) is met, can thus be reached by increasing either the height or the width of the barrier.

1.6.5 Reentrant regimes

When the barrier width $2d$ greatly exceeds the healing length, the current-phase relation becomes multivalued, as shown in Fig. 1.7 for $d = 20\xi_\infty$.

In our system, two kinds of multivalued diagrams are found for a given barrier width $2d$. We designate the first kind (green dots), appearing at larger barrier heights V_0, as reentrant type I,

and the second kind (orange diamonds in Fig. 1.7), occurring for smaller V_0, as reentrant type II. They differ in the behavior of the lower branch at small currents $j \ll 1$. The phase decreases with increasing j in type II diagrams, while it increases in type I, reaching values larger than π for $j \ll 1$. These two families of diagrams also differ in the number of positive values of the current j corresponding to the same phase difference $\delta\phi$. Indeed, diagrams of type I can have two values of j at the same $\delta\phi$, while diagrams of type II can allow for three.

The existence of these type II diagrams, to our knowledge, has not been discussed in the literature. Only type I current-phase relations were predicted and observed. As already discussed in section 1.3, the crossover from a sine-like current-phase relation to a type I diagram corresponded to the onset of phase slippage in the ac Josephson dynamics, where vortex nucleation governed the current oscillation, giving rise to strongly non-adiabatic evolution. The quantized jumps in the current correspond to a 2π phase slip taking place when no stationary solution can be smoothly (or adiabatically) reached by further increasing the phase difference. By looking the green-dotted diagram in Fig. 1.7, we see that this critical phase difference corresponds to the point $(\delta\phi_{\rm slip}, j_{\rm slip})$ where the derivative $\partial j(\delta\phi)/\partial\phi = \infty$, that is, to the right of the maximum $(\delta\phi_c, j_c)$ of the current phase relation. If, starting from the point $(\delta\phi_{\rm slip}, j_{\rm slip})$, the phase is slighlty increased by ε, the next stationary solution would be $(\delta\phi_{\rm slip} + \varepsilon - 2\pi, j_{\rm slip} - j_q)$, where j_q is a finite quantized value. In this spirit, this new found family of type II diagrams, having a different structure, might introduce novel features in the ac Josephson dynamics.

In the remainder of this section, we will develop an analytical model that captures the essential features underlying both kinds of reentrant current-phase diagrams introduced before. Examination of typical density profiles belonging to the reentrant regime (see Fig. 1.8) suggests to construct the lower solution by starting from the upper one at the same current, then adding a grey soliton inside the barrier region.

Since we are dealing with wide barriers, we describe the upper solution in the local density approximation (LDA), neglecting the quantum pressure term in Eq. (1.40). This provides a hydrodynamic description of the weak link of the same kind discussed in section 1.4, with the difference that here we do not assume incompressibility, which is a poor approximation for dilute BECs. At a fixed current j, the density inside the barrier $|x| < d$ is constant and equal to $n_0 = \tilde{\mu}/3g + 2\tilde{\mu}\cos(\omega/3)/3g$, when $j < j_{\rm th}$, or $n_0 = \tilde{\mu}/3g + 2\tilde{\mu}\cos(\pi/3 - \omega/3)/3g$, when $j > j_{\rm th}$, with $j_{\rm th}$ defined by $j_{\rm th}^2 = 4\tilde{\mu}^3/27mg^2$, and $\omega = \arccos|1 - 27mg^2j^2/4\tilde{\mu}^3|$. The phase difference calculated within LDA misses the pre-bulk term in Eq. (1.47), thus, for the upper branch, it is

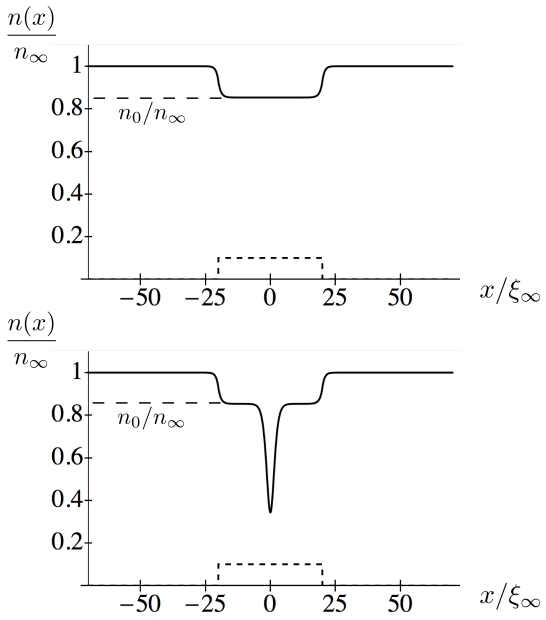

Fig. 1.8: Typical density profiles in the reentrant regime $d = 20\xi_\infty$ for the upper (upper panel) and lower (lower panel) solutions. Here $V_0 = 0.1gn_\infty$, and $j = 0.5c_\infty n_\infty$

simply

$$\delta\phi_1 = \frac{2mjd}{\hbar}\left(\frac{1}{n_0} - \frac{1}{n_\infty}\right). \tag{1.54}$$

Now, for the density profile of the lower branch $n_2(x)$, we take a grey soliton (Eq. (1.41)) placed inside the barrier at $x = 0$, with a bulk density given by n_0 and a bulk velocity $v_0 = j/n_0$ while in the region $|x| > d$ we keep the density profile of the upper branch, that is, a constant density n_∞ and velocity j/n_∞. Notice that in this subsection n_0 stands for the density of the upper solution at $x = 0$, as indicated in Fig. 1.8. The density at $x = 0$ for the lower solution corresponds to the center of the dip in the grey soliton density profile. Finally, using Eq. (1.47) we obtain the phase difference for the lower branch

$$\delta\phi_2 = \delta\phi_1 + 2\arccos\sqrt{\frac{mv_0^2}{gn_2(d)}}. \tag{1.55}$$

At a given current j, the overall phase difference corresponding to the lower solution has two contributions: i) the "hydrodynamic phase" $\delta\phi_1$ and 2) the "nonlinear-dispersive phase" $\delta\phi_{\rm sol} = 2\arccos\sqrt{mv_0^2/gn_2(d)}$ accumulated across the grey soliton. While $\delta\phi_1$ is a monotonically increasing function of j, $\delta\phi_{\rm sol}$ is instead monotonically decreasing, starting from π at zero current. Indeed, by further approximating $n_2(d) \simeq n_0$ we get $\delta\phi_{\rm sol} = 2\arccos(j/\sqrt{gn_0^3/m})$.

Then, since n_0 is a monotonically decreasing function of j, the argument of arccos increases for increasing current. Therefore, starting from π at $j = 0$, $\delta\phi_{\rm sol}$ decreases monotonically with j. In correspondence of the point where these two opposed contributions equal each other, the current has infinite derivative with respect to the phase. This point is indeed the phase slip critical point $(\delta\phi_{\rm slip}, j_{\rm slip})$ introduced above.

Therefore, the multivaluedness characterizing a reentrant current-phase relation is due to the competition between the hydrodynamic and the nonlinear-dispersive components of the flow, which can coexist only for barriers wide enough to accomodate a soliton inside. In particular, we can derive a condition for the appearance of type I reentrant behavior upon expanding Eq. (1.55) for small currents, and requiring $\delta\phi_2 > \pi$. Using $\arccos(x) \simeq \pi/2 - x$, for $x \ll 1$, we get $\delta\phi_2 \simeq \pi + 2j\nu$, where $\nu = md(1/n_0 - 1/n_\infty)/\hbar - \sqrt{m/gn_0^3}$, and we have taken $n_2(d) \simeq n_0$. The condition for type I reentrance to appear is thus $\nu > 0$. For $j \ll 1$, we have $n_0 \simeq \tilde{\mu}/g \simeq n_\infty - V_0/g$, and since within the LDA approximation $V_0 \ll gn_\infty$, the condition $\nu > 0$ takes the simple form

$$\frac{V_0}{gn_\infty}\ \frac{d}{\xi_0\sqrt{2}} > 1, \tag{1.56}$$

with $\xi_0 = \hbar/\sqrt{2mgn_0}$ being the healing length inside the barrier region where the density is n_0. Equation (1.56), holding for $V_0 \ll gn_\infty$, has a clear physical meaning: in order to have a type I reentrant current phase diagram, the barrier width $2d$ must be sufficiently larger than $2\sqrt{2}\xi_0$, which is the characteristic size of a soliton placed inside the barrier.

In Fig. 1.9, we compare the current-phase relation calculated with the above model (solid lines) to the exact results. Within the reentrant regime, for both type I and type II, the agreement is striking with only slight differences close to the the maximum $(\delta\phi_c, j_c)$. On the other hand, for thin/strong barriers, LDA, and in turn the above model, is in clear disagreement with the exact results. (See cases $d = 3\xi_\infty$ in Fig. 1.9).

The difference between type I and type II diagrams has a physical interpretation within the above model, namely that the hydrodynamic component of the flow dominates for all currents in type I reentrance (excluding the region[7] $j \simeq j_c$), while it is overcome by the nonlinear-dispersive part for sufficiently small current in type II.

In the literature [57], multivalued current-phase relations are typically modelled by describing the weak link with an equivalent circuit containing a linear inductance in series with a sinusoidal

[7] close to the critical point $(\delta\phi_c, j_c)$, and for every current-phase relation, the lower branch always has a phase decreasing with increasing current, up to the critical point itself, at which it meets the upper branch. In particular, for reentrant diagrams, this means that the dispersive part of the flow always dominates over the hydrodynamic part sufficiently close to the critical point.

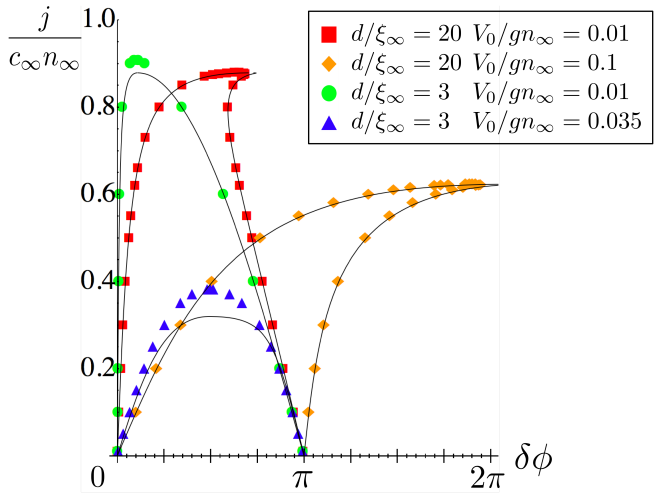

Fig. 1.9: Comparison between the LDA+soliton model (black solid lines) and the exact results (see inset).

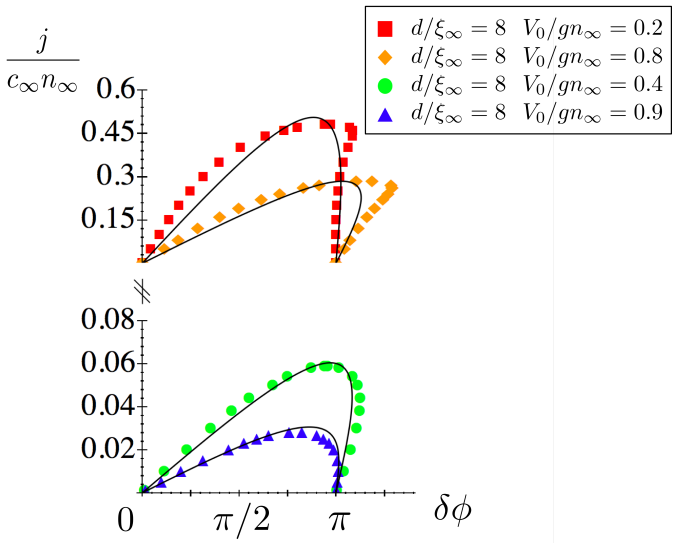

Fig. 1.10: (Color online) Comparison between the Deaver-Pierce model (black solid lines) and the exact results (see inset).

inductance, the latter corresponding to an ideal Josephson junction. When compared to our GP exact results (see Fig. 1.10), this model in general fails to describe the curvature of both branches, and misses type II reentrance, as well as nearly free regimes (e.g. red squares in Fig. 3.3,1.7) since it does not allow the phase $\delta\phi_c$, corresponding to the maximum of the diagram, to be smaller than $\pi/2$. It proves quite accurate only for sufficiently large barrier heights V_0, very close to the Josephson regime. In the ^{4}He experiment of [33], this so called Deaver-Pierce model [43] agrees well with the measured current-phase relation. This might be due to the fact that these experiments are performed with a fixed weak link configuration, moving the system across the transition between Josephson and type I reentrant regime, upon changing the ^{4}He healing length with temperature, but always staying sufficiently close to the Josephson regime.

1.6.6 Outlook

The most important result reported here is the discovery of a new kind of multivalued current-phase relation for dilute BECs, different from the reentrant diagrams observed with superfluid helium. Further developments of this project would involve the study of the ac Josephson dynamics, with special attention to the reentrant regimes, and the possible differences in the phase slip behavior between type I and type II reentrant current-phase relations.

It will also be important extend these results in order to propose a scheme for the observation of the above transport regimes with a dilute BEC inside a double-well trap.

1.7 Josephson plasma oscillations from hydrodynamic to tunneling transport

This section is based on the work: **Dynamics of a tunable superfluid junction**, L. J. LeBlanc [*Department of Physics, University of Toronto, 60 St. George, Toronto ON, Canada, M5S 1A7*], A. B. Bardon [*ibid.*], J. McKeever [*ibid.*], M. H. T. Extavour [*ibid.*], D. Jervis [*ibid.*], J. H. Thywissen [*ibid.*], F.P., and A. Smerzi [*INO-CNR, BEC Center, and Dipartimento di Fisica, Via Sommarive 14, 38123 Povo, Trento, Italy*], published in Phys. Rev. Lett. **106**, 025302 (2011). This work is a theory-experiment collaboration. The experiment was performed in J. Thywissen's group at the University of Toronto.

In section 1.6, we have seen how the current phase relation of a dilute BEC flowing through

a weak link can be modified, by changing the length of the link, from purely sinusoidal to multi-valued (reentrant). As already mentioned, this crossover from hydrodynamic to ideal Josephson transport has been demonstrated with superfluid helium by Packard's group [11, 33]. The experiment consisted in measuring the current-phase relation in the standard ac Josephson effect, where a chemical potential difference between two superfluid helium reservois was created through a pressure drop. The weak link was realized by a nanometer-sized aperture array. The effective link length was tuned by modifiying the healingh length ξ upon changing the temperature (see section 1.2) from close to much below the critical value. The crossover from a sinusoidal to a reentrant current-phase relation coincided with the onset of phase slippage dynamics, characterized by sawtooth current oscillations.

In the field of ultracold gases, Josephson effect(s) have been experimentally demonstrated in both double-well [3, 55] and multiple-well optical trapping potentials [18, 66, 1]. In a double-well trap, the role of the superfluid reservoirs is played by the two spatially localized parts in which the-still fully coherent-cloud is split, each confined about either of the two potential minima. The chemical potential difference is created by an imbalance in the occupation of these two halves.

This double-well implementation of a dilute BEC Josephson junction presents important differences from the superfluid helium counterpart [78]. The essential difference comes from the finite compressibility of the BEC, which, toghether with the mesoscopic size of the samples which are typically employed, makes the internal energy contribution, due to atom-atom interactions, come into play. One striking manifestation of this fact is the prediction and observation of macroscopic quantum self-trapping, where the initial imbalance between the population of the two wells remains constant in time, with only small amplitude oscillations about its initial value, while the phase difference increases linearly in time under the influence of the chemical potential difference induced by internal energy. On the other hand, sinusoidal oscillations of both population and phase difference between the two wells have been observed in the small amplitude regime, where the frequency of these so called plasma oscillations not only depends on the overlap between the two localized wavefunction, as it is in ideal Josephson tunneling regime (see section 1.4), but also on the internal energy coming from interatomic interactions.

All the so far performed experiments with dilute BECs are well described by a two-mode model (TMM) [42, 89, 65, 102, 4, 90], which is charaterized by a sinusoidal current-phase relation. This fact indicates that the regime of transport so far explored was dominated by tunnelling, therefore close to the ideal Josephson regime, apart from the new features introduced by the internal energy contribution. However, one must note that this is not strictly true, since, in

absence of interaction among the atoms, the Scrödinger equation for the order parameter is exactly equivalent to the TMM for any height of the inter-well barrier, provided the oscillation amplitude is small and the anharmonicity of the trap is negligible. In this case, observing that the oscillations are well described by a TMM would not imply tunnelling transport. Anyway, the fact that an experiment is well decribed by a TMM, for sure implies that the system is not in the hydrodynamic regime (see section 1.2,1.4), either because of the small interactions, or because of tunnelling governing the transport.

As noted in the previous section, the measurement of the current-phase relation has never been performed with dilute BECs, and also the experimental observation of a crossover from hydrodynamic to tunnelling transport has never been pursued.

1.7.1 Overview of the main results

In this work, we study the transport of a BEC between two wells separated by a tunable barrier, and experimentally demonstrate the crossover from hydrodynamic to ideal Josephson transport by analyzing the measured frequency of the small amplitude plasma oscillations. As the barrier height V_b is adjusted from below to above the BEC chemical potential, μ, the density in the link region decreases until it classically vanishes when $V_\mathrm{b} = \mu$. The healing length in the link region, ξ, increases with V_b and dictates the nature of transport through this region. Starting from a slight imbalance in the population of the two wells, we observe Josephson plasma oscillations with a frequency spanning three octaves, as we smoothly tune ξ from $0.3d$ to $2d$, where d is the separation between the wells. In the low barrier regime, the oscillation frequency is well predicted by using hydrodynamic equations (1.20) and (1.22), while when V_b is higher than μ we find good agreement with a TMM.

We thus demonstrate the crossover through the comparison of experimental data with two different theoretical models which are valid either in the hydrodynamic or the ideal Josephson regime of transport. This approach is needed because only plasma frequencies are measured here, and we do not probe the full current-phase relation, since the phase only makes small oscillations around zero.

A secondary but interesting finding is the observation of a higher frequency component in the oscillation spectrum, corresponding to the excitation of a second collective mode which also drives population transfer between the two wells. We follow this second mode throughout the hydrodynamic to tunnelling transport crossover, and observe that its amplitude vanishes when the system enters the tunnelling regime. By comparison with the GP equation, which agrees

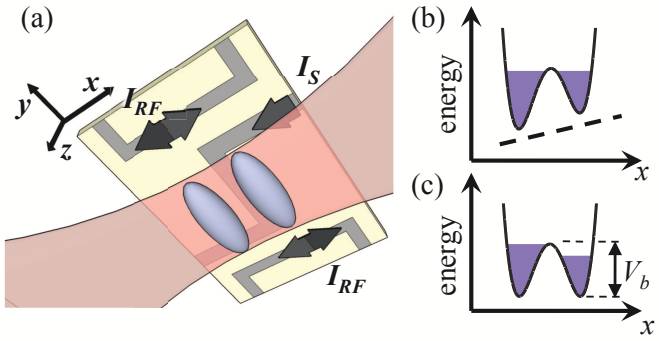

Fig. 1.11: (a) Schematic of atom chip double-well trap. Central 'Z' wire [79] carries static trapping current, $I_{\rm S} = 2$ A, which, with uniform external fields $\mathbf{B}_{\rm ext} = \langle 2.2, 0.11, 0\rangle$ mT, results in an Ioffe-Pritchard style trap with harmonic trapping frequencies $(\omega_{x_0,z_0}, \omega_{y_0}) = 2\pi \times (1300, 10)$ Hz. Side wires are 1.58 mm from trap center and carry RF currents with amplitude $I_{\rm RF}$. This RF current produces a z-polarized field at the trap location with amplitude $B_{\rm RF} = 23.6 \pm 0.6$ μT (peak Rabi frequency $\Omega = 2\pi \times (82 \pm 2$ kHz)). A levitation beam (pink) is positioned to provide a force cancelling gravity (z-direction) while compressing the sample along y. Atoms are trapped 190 μm from the chip surface. (b) A schematic one-dimensional cut at $t = -0.5$ ms through trapping potential along x (solid line) in the presence of linear bias (dashed line) and (c) balanced potential at $t = 0$, with $\mathcal{Z}_0 \neq 0$.

very well with the experimental data for all barrier heights, we find that the excitation of the higher mode is due the combination of trap anharmonicity, axial anysotropy about the splitting axis, and nonlinearity due to atom-atom interactions.

1.7.2 Experimental preparation of a BEC in an atom chip double-well trap

The experiment begins as ^{87}Rb atoms in the $|F = 2, m_F = 2\rangle$ ground state are trapped on an atom chip and evaporatively cooled in a static magnetic potential $\mathbf{B}_{\rm S}(\mathbf{r})$, as described elsewhere [9]. To prevent gravitational sag and to compress the trap in the weak direction (with characteristic trap frequency $\omega_y = 2\pi \times 95$ Hz), we add an attractive optical potential with a 1064 nm beam. We dress the static potential with an oscillating radio-frequency (RF) magnetic field [21, 53] radiating from two parallel wires on the atom chip (Fig. 1.11(a)). In the rotating-wave approximation (RWA), the adiabatic potential created by the combination of the static chip trap,

the RF dressing, and the optical force is

$$U(\mathbf{r}) = m'_F \mathrm{sgn}(g_F)\hbar\sqrt{\delta(\mathbf{r})^2 + \Omega_\perp^2(\mathbf{r})} + \tfrac{1}{2}m\omega_y^2 y^2, \tag{1.57}$$

where $m'_F = 2$ is the effective magnetic quantum number, $\delta(\mathbf{r}) = \omega_{\mathrm{RF}} - |\mu_{\mathrm{B}} g_F B_{\mathrm{S}}(\mathbf{r})/\hbar|$ is the detuning, $\Omega_\perp(\mathbf{r}) = \mu_{\mathrm{B}} g_F B_{\mathrm{RF},\perp}(\mathbf{r})/2\hbar$ is the RF Rabi frequency, $B_{\mathrm{RF},\perp}(\mathbf{r}) = |\mathbf{B}_{\mathrm{S}}(\mathbf{r}) \times \mathbf{B}_{\mathrm{RF}}(\mathbf{r})|/|\mathbf{B}_{\mathrm{S}}(\mathbf{r})|$ is the amplitude of the RF field locally perpendicular to $\mathbf{B}_{\mathrm{S}}(\mathbf{r})$, μ_{B} is the Bohr magneton, g_F is the Landé g-factor, $\hbar$ is the reduced Planck's constant and m is the atomic mass. By assuming the individual wells are harmonic near each minimum, calculations show that $\omega_z = 2\pi \times 425$ Hz, and ω_x varies from $2\pi \times 350$ Hz to $2\pi \times 770$ Hz as we tune from low to high barriers. For comparison between theory and experiment, we account for small corrections to Eq. (1.57) beyond the RWA [32].

After turning on the dressing field at a frequency $\omega_{RF} = 2\pi \times 765$ kHz, where the trap is a single well, we evaporatively cool to produce a BEC with no discernible thermal fraction. In 20 ms, we adiabatically increase ω_{RF} to a new value characterized by $\delta_0 \equiv \delta(\mathbf{r} = \mathbf{0})$, such that the barrier V_{b} rises and the dressed state potential splits along the x-direction into two elongated traps [82].

1.7.3 Population imbalance oscillations analysis

Using a second 1064 nm beam weakly focussed off-center in x, an approximately linear potential is added across the double-well junction to bias the population towards one well (Fig. 1.11(b)). By applying the bias beam before and during the splitting process, we prepare systems of atoms with a population imbalance $\mathcal{Z} \equiv (N_{\mathrm{R}} - N_{\mathrm{L}})/(N_{\mathrm{R}} + N_{\mathrm{L}})$, where N_{R} (N_{L}) is the number of atoms in the right (left) well. The range of initial population imbalances $\mathcal{Z}_0 = \mathcal{Z}(t = 0)$ we use is 0.05 to 0.10, small enough to avoid self-trapping [3], and observe small-amplitude plasma oscillations. To initiate the dynamics, the power of the bias beam is ramped off in 0.5 ms, which is faster than the characteristic population transfer rate between the two wells). The out-of-equilibrium system is then allowed to evolve for a variable time t in the symmetric double-well (Fig. 1.11(c)).

To measure the time-dependent population $\mathcal{Z}(t)$, we freeze dynamics by rapidly increasing both B_{RF} and ω_{RF} to separate the wells by 70 μm, where $V_{\mathrm{b}}/\mu \sim 10^4$. We then release the clouds from the trap and perform standard absorption imaging along y after 1.3 ms time-of-flight (Fig. 1.12(b)). Analysis of these images allows us to determine N_{R} and N_{L} to a precision of ±50 atoms.

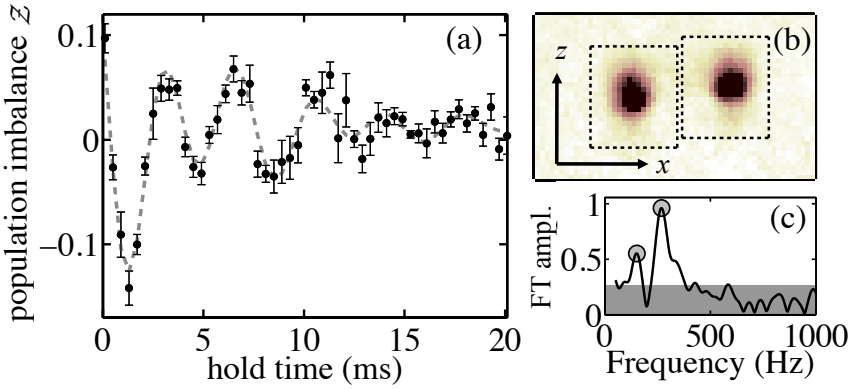

Fig. 1.12: (a) Population imbalance, $\mathcal{Z}$, vs. time for $\delta = 2\pi \times (0.1 \pm 0.5)$ kHz, $N = 5900 \pm 150$. The dashed line is a decaying two-frequency sinusoidal fit to the data, using two fixed frequencies from the FT (lower inset). Each point is the average of six repetitions of the experiment; error bars are statistical. (b) Averaged absorption image after separation and 1.3 ms time of flight, with right and left measurement regions (dashed boxes) indicated. (c) FT amplitude spectrum of data showing two distinct peaks at 268 ± 6 and 151 ± 13 Hz rising above the noise floor (grey).

Upon release of the potential bias, we find that the population $\mathcal{Z}(t)$ oscillates about[8] $\mathcal{Z} = 0$ (Fig. 1.12(a)). To analyze the dynamics, we use a Fourier transform (FT) to find the dominant frequency components (Fig. 1.12(c)). We repeat this measurement at many values of V_b/μ, where μ is the Thomas-Fermi chemical potential, by varying δ_0. For the purposes of this analysis, we ignore the decay of this signal, the $1/e$ time constant of which is typically two oscillation periods. We shall discuss this issue in more detail in subsection 1.7.7

When the barrier is low, $\mathcal{Z}(t)$ consistently displays two dominant frequency components. For higher barriers, the amplitude of the higher-frequency mode decreases until only a single frequency rises above the noise floor. The white points in Fig. 1.13 give these measured frequencies as a function of the experimental parameter δ_0, and the calculated ratio of barrier height to chemical potential, V_b/μ. The ensembles used in Fig. 1.13 had total atom number $N = 6600 \pm 400$ (± 1700), where the error bar is statistical (systematic).

In order to verify that the system crosses over between two completely different regimes of transport, we compare the lower frequency of the population imbalance oscillations to the

[8] When the average value of $\mathcal{Z}$ differs from zero, we subtract the average $\bar{\mathcal{Z}}$ from all values of $\mathcal{Z}(t)$. In all experiments, $|\bar{\mathcal{Z}}| < 0.05$.

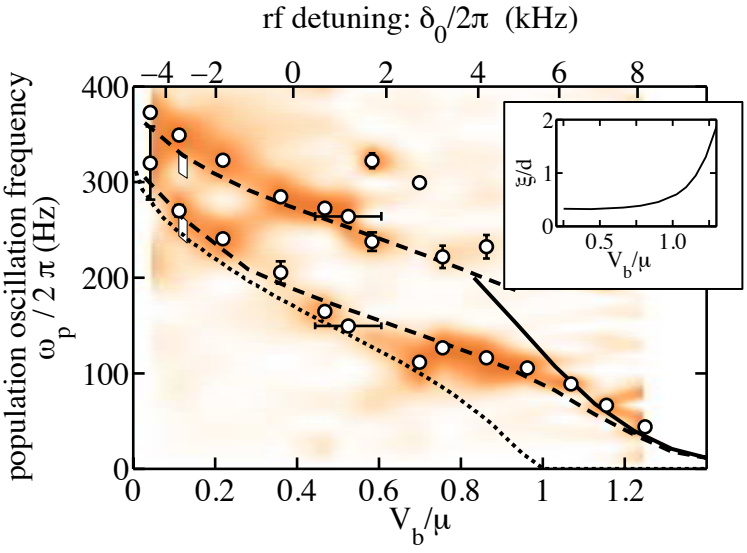

Fig. 1.13: Frequency components of population imbalance vs. RF detuning (measured) and barrier height to chemical potential ratio (calculated). Experimental points (white circles) represent the two dominant Fourier components at each detuning; error bars represent uncertainty contributed by noise in the FT from a single time series, but do not include shot-to-shot fluctuations. The spectral weight is represented through the color map, which has been linearly smoothed between discrete values of $V_{\rm b}/\mu$ and darker colors indicate greater spectral weight. All calculations use N = 8000 and $\mathcal{Z}_0 = 0.075$, and a single-parameter fit of the data to the GP curves shifts all experimental points by $\delta_{\rm shift} = 2\pi \times 5.1$ kHz to compensate for a systematic unknown in $B_{\rm S}(\mathbf{0})$. Statistical vertical error bars are shown, while a typical horizontal statistical error bar is shown at $V_{\rm b}/\mu \approx 0.5$. Dashed line represent 3D GP frequencies, the solid line the plasma oscillation frequency predicted by the TMM, $\omega_{\rm p}/2\pi$, and the dotted line the hydrodynamic result, $\omega_{\rm HD}/2\pi$. White bars at $V_{\rm b}/\mu \sim 0.1$ indicate the bounds of the GP simulation corresponding to the systematic plus statistical uncertainty in atom number. Inset: ratio of healing length, ξ, to inter-well distance, d, as a function of $V_{\rm b}/\mu$. ξ is calculated at the center of the barrier.

prediction of two models which are supposed to be valid in the two opposite limits, namely, the superfluid hydrodynamics equations (1.20)-(1.22), and a TMM.

1.7.4 The hydrodynamic regime

For small barrier height, we compare our experimentally measured frequencies with a hydrodynamic prediction, given by the dotted line in Fig. 1.13. We find good agreement with the measured lower frequency mode at low barriers. Since tunnelling cannot contribute to hydrodynamic transport, the corresponding frequency goes to zero as $V_{\rm b} \rightarrow \mu$. The breakdown in hydrodynamics also coincides with an increasing healing length, as shown in the inset of Fig. 1.13.

Let us now describe how the hydrodynamic estimate is obtained. We use the equations (1.20)-(1.22), where the local chemical potential $\mu_0(n)$ has two contributions, one from the internal energy $gn(\boldsymbol{r})$, and the other from the external potential $U(\boldsymbol{r})$. We assume that the population imbalance oscillates harmonically, which is tantamount to neglecting the higher frequency components. In our case, we are essentially neglecting the frequency component corresponding to the second collective mode we excite by the linear bias potential. The equation of motion for the population imbalance $\mathcal{Z}$ thus reads:

$$\ddot{\mathcal{Z}} = -\omega_{\rm HD}^2 \mathcal{Z} \tag{1.58}$$

where $\omega_{\rm HD}$ is the hydrodynamic frequency that characterizes the system.

The first time derivative of $\mathcal{Z} \equiv 2N_{\rm R}/N$ is

$$\dot{\mathcal{Z}} = \frac{2}{N}\int_{V_R} d^3r \;\; \dot{n} = -\frac{2}{N}\int_{V_R} d^3r \; \nabla\cdot(n\mathbf{v}) = -\frac{2}{N}\int_S d\sigma \; \hat{\nu}\cdot(n\mathbf{v}), \tag{1.59}$$

where we have used the continuity equation (1.22). Here V_R is the volume of the right well, S is the area of the plane separating the two wells, and $\hat{\nu}$ is the unit normal vector for this plane.

The second derivative of $\mathcal{Z}$ is then

$$\ddot{\mathcal{Z}} = -\frac{2}{N}\int_S d\sigma \; \hat{\nu}\cdot(\dot{n}\mathbf{v} + n\dot{\mathbf{v}}). \tag{1.60}$$

To evaluate the frequency, $\omega_{\rm HD}$, we use the fact that at $t = 0$ the system is in the ground state, so that $\mathbf{v}(t=0) = 0$. The time derivative of $\mathbf{v}$ is given by the Euler equation (1.20), and we get

$$\ddot{\mathcal{Z}}\Big|_{t=0} = \frac{2}{mN}\int_S d\sigma \; n \; \hat{\nu}\cdot\boldsymbol{\nabla}\left(U(\mathbf{r}) + gn\right). \tag{1.61}$$

The geometry of this double well system is such that the normal vector $\hat{\nu} = \hat{x}$, and the only component of the gradient which contributes is the x-component. Assuming some initial imbalance, $\mathcal{Z}_0$, the frequency with which the populations oscillate is given by

$$\omega_{\rm HD}^2 = -\frac{\ddot{\mathcal{Z}}}{\mathcal{Z}} = -\frac{2}{mN\mathcal{Z}_0}\iint_S dydz \; n \; \frac{\partial}{\partial x}\left(U(\mathbf{r}) + gn\right). \tag{1.62}$$

Consistently with hydrodynamic approach, we calculate this initial density profile in the trap, tilted by a linear bias Gx, in the local density (Thomas-Fermi) approximation:

$$n_{\rm TF}(\mathbf{r}) = \frac{1}{g}\left(\mu - (U(\mathbf{r}) + Gx)\right), \tag{1.63}$$

The gradient term in the integrand of Eq. (1.62) is then simply $-G$.

The characteristic frequency is thus

$$\omega_{\rm HD}^2 \approx \frac{2G}{mN\mathcal{Z}_0}\iint_S dydz\; n_{\rm TF}, \tag{1.64}$$

which can be found by simply evaluating the density at the surface between the two wells and integrating over the region by which the two halves are connected. From this expression, we see that the $\omega_{\rm HD}^2$ decreases as the area connecting the wells decreases, and falls to zero when the barrier surpasses the chemical potential and the Thomas-Fermi density is strictly zero on the plane S.

The equation (1.62), upon substituting $n_{\rm TF}$ with the Gross-Pitaevskii ground state density, is also valid when we include a quantum pressure term in Eq. (1.20). However, even with the quantum pressure, this model is not in exact agreement with the Gross-Pitaevskii equation, due to the non-harmonic component in the oscillation. At high barriers, though anharmonicity is small, Eq. (1.62) is less accurate than the TMM.

We have checked that the frequencies predicted by Eq. (1.64) are consistent with the dynamical simulations of Eqs. (1.20) and (1.22), done using a test particle method [88].

1.7.5 The tunnelling regime and the Two-Mode Model

When the barrier is higher that the chemical potential, and tunnelling dominates transport, we find that a TMM accurately predicts the measured lower mode frequency, as shown in Fig. 1.13. The agreement is very good even for $V_{\rm b}$ just above μ, beyond which the frequency decreases exponentially. To our knowledge, this constitutes the first direct observation of tunnelling transport of neutral atoms through a magnetic barrier, only inferred, for instance, in Refs. [51, 61].

In the remainder of this subsection, we will describe the TMM we employed, corresponding to the solid black line in Fig. 1.13. The model is based on the nonlinear two-mode ansatz used in [90],

$$\Psi(\mathbf{r},t) = \psi_{\rm R}(t)\Phi_{\rm R}(\mathbf{r};N_{\rm R}(t)) + \psi_{\rm L}(t)\Phi_{\rm L}(\mathbf{r};N_{\rm L}(t)) \tag{1.65}$$

where $\psi_{\rm R,L}(t) = \sqrt{N_{\rm R,L}(t)}\exp(i\theta_{\rm R,L}(t))$ and $\Phi_{\rm R,L} = (\Phi_+ \pm \Phi_-)/\sqrt{2}$ is a real function localized in the left (right) well, with Φ_+ (Φ_-) being the ground (first antisymmetric) state of the GPE

along the splitting direction, with the normalization $\int d^3r|\Phi_\pm|^2 = 1$. Substituting Eq. (1.65) in the GP equation (1.37), we get two equations for the population imbalance $\mathcal{Z}$ and the phase difference $\Delta\phi = \theta_{\rm R} - \theta_{\rm L}$:

$$\begin{aligned}\hbar\frac{d}{dt}\mathcal{Z} &= \Delta E\sqrt{1-\mathcal{Z}^2}\sin(\Delta\phi),\\ \hbar\frac{d}{dt}\Delta\phi &= -(\mu_{\rm L}-\mu_{\rm R}) - \Delta E\frac{\mathcal{Z}}{\sqrt{1-\mathcal{Z}^2}}\cos(\Delta\phi),\end{aligned} \tag{1.66}$$

where

$$\mu_{\rm L,R} = \int d^3r\left[\frac{\hbar^2}{2m}(\nabla\Phi_{\rm R,L})^2 + V_{\rm ext}\Phi_{\rm R,L}^2 + gN_{\rm R,L}\Phi_{\rm R,L}^4\right], \tag{1.67}$$

and $\Delta E = E_- - E_+ = 2(\mathcal{K} + N\chi)$ with

$$E_\pm = \int d^3r\left[\frac{\hbar^2}{2m}(\nabla\Phi_\pm)^2 + V_{\rm ext}\Phi_\pm^2 + \frac{1}{2}gN\Phi_\pm^4\right], \tag{1.68}$$

$$\mathcal{K} = -\int d^3r\left[\frac{\hbar^2}{2m}(\nabla\Phi_{\rm R})(\nabla\Phi_{\rm L}) + \Phi_{\rm R}V_{\rm ext}\Phi_{\rm L}\right], \tag{1.69}$$

$$\chi = -\frac{g}{4}\int d^3r\Phi_{\rm R}^3\Phi_{\rm L}. \tag{1.70}$$

In obtaining Eqs. (1.66), we have discarded the overlap integrals of the kind $g\int d^3r\Phi_{\rm L}^2\Phi_{\rm R}^2$ since, in all the explored regions of parameters where the TMM is in good agreement with GP equation, these are always neglegible.

Now, assuming that $\mathcal{Z}, \Delta\phi \ll 1$, we can linearize the equations (1.66). First, we have to take into account the dipendence of $\Phi_{\rm L,R}$ on the well occupations $N_{\rm L,R}$, which is the essence of the nonlinear ansatz (1.65). We consider this dependence only in the last term of the local chemical potential, which then reads:

$$\mu_{\rm L} \simeq \int d^3r\left[\frac{\hbar^2}{2m}(\nabla\ \Phi_{\rm L}|_{N_{\rm L}=N/2})^2 + V_{\rm ext}\ \Phi_{\rm L}|^2_{N_{\rm L}=N/2} + gN_{\rm L}\Phi_{\rm L}^4\big|_{N_{\rm L}=N/2} + \right.$$
$$\left. +\ \frac{\partial}{\partial N_{\rm L}}(gN_{\rm L}\Phi_{\rm L}^4)\Big|_{N_{\rm L}=N/2}(N_{\rm L}-\frac{N}{2})\right].$$

The linearized equations then give harmonic oscillations of both phase difference and population imbalance, with the characteristic plasma frequency:

$$\omega_p^2 = \frac{1}{\hbar^2}\Delta E\left(\Delta E + N\frac{\partial\mu_{\rm L,R}}{\partial N_{\rm L,R}}\right), \tag{1.71}$$

where we assumed that the external potential $V_{\rm ext}$ is symmetric about zero along the splitting direction. In order to calculate the plasma frequency for our double-well system, we use the trap given in Eq. (1.57) as the external potential, and find numerically the wave functions $\Phi_\pm$. By

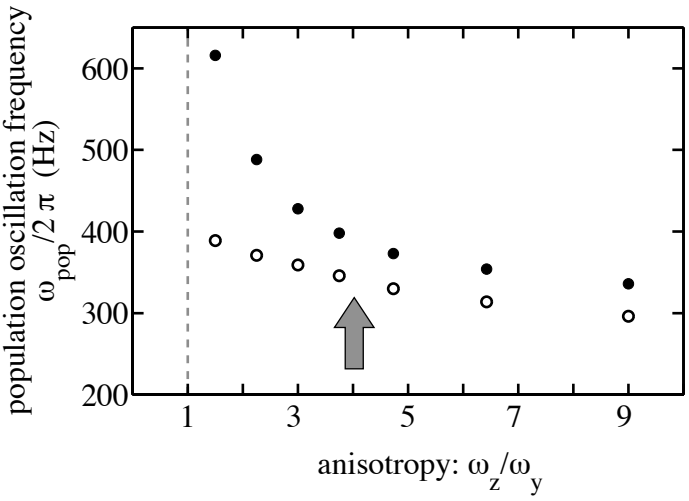

Fig. 1.14: Mode frequencies for $m = 0$ (open) and $m = 2$ (closed) as a function of trap anisotropy. Grey arrow indicates the anisotropy used in this experiment. These calculations use the approximate potential Eq. (1.72). The anisotropy is changed by keeping ω_z fixed and decreasing ω_y

repeating the calculation for slightly different N, we can also estimate the value of the derivative of the local chemical potential $\mu_{\mathrm{L,R}}$.

One dinstictive feature of the nonlinear TMM is indeed the fact that the plasma frequency ω_p depends on the derivative of the single-well chemical potential $\mu_{\mathrm{L,R}}$, and therefore takes into account the effect of transverse degrees of freedom on the effective nonlinearity determining the interaction energy. This provides an important correction, typically around 20%, which is crucial to reach a good agreement between the TMM and the GP equation in the proper limit.

1.7.6 Comparison with GP equation and the analysis of the higher mode

We have so far demonstrated that, upon tuning the height of the interwell barrier, we could modify the nature of transport in our system from hydrodynamic, where the frequency of the plasma oscillations is proportional to the effective cross-area of the weak link and is well predicted by classical fluid dynamics equations (1.20)(1.22), to tunnelling, where the frequency depends on the overlap between the two wavefunctions localized on either side of the link and is well

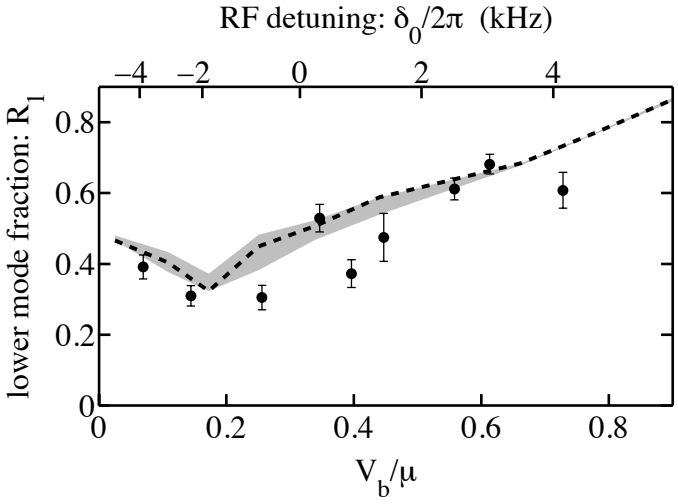

Fig. 1.15: Amplitude fraction of low-frequency mode in population dynamics. Dashed line shows the GP simulation for 8000 atoms with initial imbalance $z(0) = 0.075$. The grey shaded area represents the variation of the GP calculations over the range of z(0) = 0.05 to 0.10. The vertical error bars are statistical; the statistical uncertainty in δ is $2\pi \times 0.5$ kHz (not shown). The GP calculation gives $R_1 = 1$ when $V_\mathrm{b}/\mu \simeq 1.1$.

predicted by a TMM.

Now, in order to explain the behavior in the whole crossover between these two limiting regimes, and also the existence of the higher-frequency mode, we turn to numerical solutions of a time-dependent three-dimensional GP equation. We solve Eq. (1.37) with the double-well trap (1.57) as the external potential, starting from a ground state with $\mathcal{Z} \neq 0$, obtained by adding a linear bias potential along the splitting direction Gx, which we remove at $t = 0$. While all calculations were done using Eq. (1.57), an intuitive understanding of the potential emerges from the separable approximate form:

$$U_\mathrm{sep}(\boldsymbol{r}) \simeq \tfrac{1}{2}m\omega_y^2 y^2 + \tfrac{1}{2}m\omega_z^2 z^2 + \alpha_2 x^2 + \alpha_4 x^4 \ , \tag{1.72}$$

where $\alpha_2 < 0$. The trap exhibits an axial anisotropy, with elongation along the y-direction such that $\omega_z \sim 4\omega_y$.

The slope and separation of the two measured frequencies are well captured by the GP equation, as shown in Fig. 1.13, though the decay of population imbalance is not reproduced by these simulations.

In the following, we will discuss the structure and origin of the higher-lying mode. If our

trap were smoothly deformed to a spherical harmonic potential, the two observed modes would connect to odd-parity modes [94, 34]: the lower mode connects to the lowest $m = 0$ mode (coming from the $\ell = 1$ mode at spherical symmetry, where the quantum numbers ℓ and m label the angular momentum of the excitation and its projection along the axis of symmetry, y, respectively), while the higher mode originates from the lowest $m = 2$ mode ($\ell = 3$ at spherical symmetry). We checked this numerically by deforming our trap into a fully harmonic axially symmetric trap, and following the mode frequencies throughout this process.

With insight from GPE simulations, the observation of a second dynamical mode, which was not seen in previous experimental work [3, 55], can be explained. In a purely harmonic trap, a linear bias excites only a dipole mode [44]. By breaking harmonicity along the splitting direction, x, the barrier allows the linear perturbation ($\ell = 1, m = 0$, where x is the azimuthal axis) to excite multiple Bogoliubov modes [69]. Still two additional ingredients are required to excite the higher mode. First, atom-atom interactions couple the x-excitation to the transverse (y, z) motion through the nonlinear term in the GPE. Second, the anisotropy of the trap in the y-z plane mixes the $m = 0$ and $m = 2$ modes such that each of the resulting modes drives population transfer between wells.

We explored this last aspect in some more detail, and obtained some more information about the nature of the two collective modes we observed. We studied the role of the trap anisotropy (i.e., $\omega_z \neq \omega_y$) by observing the transformation of the $m = 0$ and $m = 2$ modes as the trap is deformed from axially symmetric to strongly axially anisotropic, in presence of a purely anharmonic potential along x, using the simplified potential, Eq. (1.72). The dipole perturbation excites both modes as soon as the axial symmetry is broken, and the spectrum shows a second frequency growing in strength as the axial anisotropy is increased. The values of the mode frequencies as a function of ω_z/ω_y are shown in Fig. 1.14. Close to axial symmetry, the lower frequency depends only slightly on the transverse confinement, indicating that the $m = 0$ mode is a dominant component of the Bogoliubov excitation. Motion is primarily along the splitting direction without oscillations in the transverse directions. Sufficiently far from axial symmetry, both frequencies start to decrease with increasing anisotropy and show a similar behavior. In particular, the experimental trapping conditions correspond to the point $\omega_z \approx 4\omega_y$, as indicated in Fig. 1.14, where the two modes begin to show a similar dependence on transverse confinement. This strongly suggests that for such high axial anisotropy, each Bogoliubov mode is mainly a combination of the two original $m = 0$ and $m = 2$ modes at axial symmetry.

To conclude, let us discuss the behavior of the amplitudes of the two collective modes, and

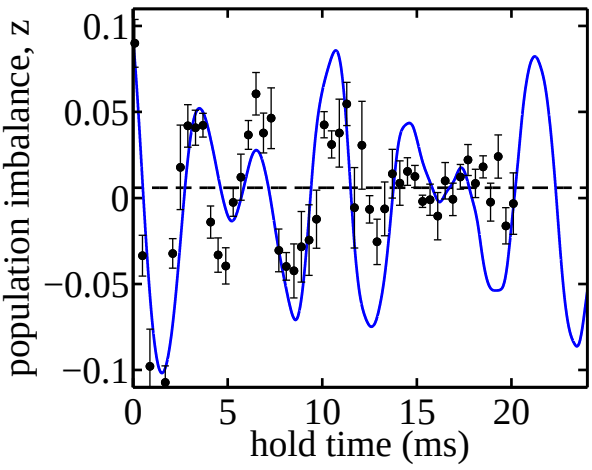

Fig. 1.16: Comparison of experimental and GP time series for $\delta = -0.1$ kHz (GP)) and $\delta = -0.1 \pm 0.5$ kHz (experiment). Experimental points are shown as black dots, and the fit to experimental data is shown as a black dashed line. The GP results are shown as a solid blue line.

in particular how the higher-lying mode disappears from the excitation spectrum. Figure 1.15 shows the relative strength $R_1 = a_1/(a_1 + a_2)$ of the lower frequency mode as a function of the barrier height. The amplitude a_1 (a_2) of the lower (higher) frequency mode is extracted from a decaying two-frequency sinusoidal fit. The modes have comparable strength, even in the linear perturbation regime, when the barrier is below the chemical potential. The small spread in the GPE amplitudes shown by the grey band indicates that the higher mode is excited independently of the initial imbalance, and is not simply due to a high-amplitude nonlinearity.

The trend in R_1 reflects the shape of the trap. When the barrier is raised from zero, the higher mode is at first more easily excited due to an increased anharmonicity along x as the trap bottom becomes flatter. By further increasing the barrier, the higher frequency mode disappears from the population oscillation spectrum due to the vanishing excitation of transverse modes. This happens since, as the wavefunctions in each individual well are increasingly localized to the effectively harmonic minima, the linear bias no longer excites intra-well transverse motion. Furthermore, in the linear perturbation regime, the inter-well Josephson plasma oscillation, like all Bogoliubov modes, cannot itself trigger any other collective mode.

1.7.7 Damping of the oscillations

As we have seen, in comparing the oscillation spectra measured in the experiment with those found from GP calculations, we have found a general agreement in both frequency and amplitude of the two lowest collective modes.

On the other hand, if we directly compare the measured oscillation timeseries to the GP result, we observe one striking difference, that is, the presence of damping in the experimental data. The measured amplitude of the population oscillations falls off with time, with a characteristic time scale of the decay, τ, approximately equal to two oscillation periods, for all values of $V_{\rm b}/\mu$. We model this as an exponentially decaying envelope in our analysis, and include it in our fitting equation.

In the GP results, no such decay is observed. Figure 1.16 shows a comparison between one experimental run and a GP calculation for very similar parameters ($\delta = -0.1$ kHz). Indeed, GP calculations to 64 ms show no sign of damping. Besides the possibility of the damping arising from technical sources, it may be due to thermal or other stochastic effects not included in the $T = 0$ mean field calculation.

1.7.8 Outlook

We have here studied the quantum transport of a BEC in a double-well potential throughout the crossover from hydrodynamic to tunnelling regimes.

Apart from fundamental interest, which we have already argued in the introduction to this work, knowing and controlling the nature of superfluid transport is crucial for technological applications of weak-link based devices, such as double-slit interferometers [51, 82, 84, 38, 5]. The adiabatic transformation of a BEC from a single- to a double-well trapping potential has been discussed in recent experimental works [51, 61, 27, 99, 38], where the experimental results were theoretically modelled using a TMM, valid, as we have here verified, at high barriers [52]. Indeed, our work demonstrates that for $V_{\rm b} < \mu$, the lowest mode frequency will lie below that estimated by the TMM. Furthermore, the higher-lying mode we observe approaches the lowest collective mode as $\omega_y \ll \omega_z$, and may be important for the dynamics of splitting in strongly anisotropic double wells [51, 77]. Whether using splitting to prepare entangled states [27], or recombination [38] to perform closed-loop interferometry [99], an improved understanding of double-well dynamics provides a foundation for controlling mesoscopic superfluids.

In summary, examination of the dynamics of an elongated BEC in a double well is timely.

Recent experiments have created squeezed and entangled states by adiabatically splitting a BEC [51, 37, 27]. The degree of squeezing inferred in the elongated case [51, 37] seems to exceed what would be expected in thermal equilibrium [27], raising the possibility that out-of-equilibrium dynamics may be important. With much remaining to be explored in these systems, this work represents the first study of the dynamics in the crossover regime.

Chapter 2

Superfluid instability and critical velocity

In the previous chapter, we have seen how macroscopic phase coherence allows superfluids to sustain a stationary flow between regions among which a constant phase difference is mantained. This feature, which is at the core of Josephson effects, implies the existence of a definite relation between the phase difference existing between two superfluid reservoirs and the current transferring particles from one to the other. The current-phase relation provides essential informations about the static and dynamical properties of transport across a superfluid weak link, as discussed before. One of these informations, which will be the subject of this chapter, is the existence of a critical current through the weak link above which a stationary flow is not possible anymore, even if a constant phase gradient is enforced. Above this critical current, superfluidity therefore looses one of his crucial features, and is to some extent "dissipated". As we shall discuss, the existence of a finite critical current is due to interactions between particles, and is responsible for the characteristic absence of visicosity observed with superfluids since their discovery.

In this chapter, using the mean-field GP equation, we will study the dynamics of superfluid dilute BECs when the flow velocity reaches the critical value above which stationary currents are impossible. We will also investigate the behavior of the critical current, or critical velocity, in different geometries and dimensionalities, trying to determine a general criterion for the breakdown of stationary superfluid flows.

2.1 Critical velocity and the absence of stationary solutions

In section 1.6, we have studied the current-phase relation using the GP equation in presence of a repulsive square barrier across the flow. The critical current, corresponding to the highest value of the current as a function of the phase, corresponds to the point above which stationary solutions do not exist anymore. More precisely, at this critical point the two branches of solutions, one plane-wave-like and the other soliton-like (in the sense clarified in subsection 1.6.2), become the same.

The disappearance of stationary solutions defines a critical velocity but, in principle, this is does not necessarily coincide with the "true" critical velocity at which the superfluid flow becomes unstable and dissipates its energy. A good example is provided by the plane wave solution in absence of an obstacle: the stationary solution always exists, but an energetic instability sets in when the velocity equals the sound speed, according to the well known Landau criterion. In general, the instability can appear at a velocity lower than the one above which stationary solutions are absent.

However, in the case of GP equation in presence of a single obstacle, there are indications that the velocity at which the stationary solutions merge and disappear is the true critical velocity. This has been verified by performing dynamical simulations by Hakim [31], solving a one-dimensional GP equation in presence of a repulsive delta potential barrier, and by Pham *et* al. [73], solving a two-dimensional GP equation in presence of a circular impenetrable disk. In both cases, two branches[1] of solutions were found. Solutions belonging to the first branch, when dynamically evolved using the time-dependent GP equation, remained stationary up to the velocity for which they existed. Solutions in the second branch were instead found to be time-dependent for any velocity. The former branch, which one could thus call stable branch, contains the plane-wave-like solutions, while the soliton-like solutions belong to the unstable branch. In two dimensions the soliton-like solutions actually contain vortices, which, as we shall see, are the two-dimensional equivalent of the solitonic excitation for phase slip dissipation. The GP dynamics, when the velocity is larger than the value for which stationary solutions cease to exist, was studied in one-dimensional cases [31] by adiabatically increasing the velocity above this threshold value during time evolution, which resulted into soliton nucleation.

[1] Pham *et* al. find also a third asymmetric branch between the two symmetric branches

2.2 Critical velocities in effectively one-dimensional flow : hydrodynamics and mean-field predictions

This section is extracted from the work: **Critical velocity of superfluid flow through single-barrier and periodic potentials**, G. Watanabe [*INO-CNR, BEC Center, and Dipartimento di Fisica, Via Sommarive 14, 38123 Povo, Trento, Italy, RIKEN, 2-1 Hirosawa, Wako, Saitama 351-0198, Japan*], F. Dalfovo [*INO-CNR, BEC Center, and Dipartimento di Fisica, Via Sommarive 14, 38123 Povo, Trento, Italy*], F. P., L. P. Pitaevskii [*INO-CNR, BEC Center, and Dipartimento di Fisica, Via Sommarive 14, 38123 Povo, Trento, Italy, Kapitza Institute for Physical Problems, 119334 Moscow, Russia*], and S. Stringari [*INO-CNR, BEC Center, and Dipartimento di Fisica, Via Sommarive 14, 38123 Povo, Trento, Italy*], published in Phys. Rev. A **80**, 053602 (2009). This work was devoted to the comparison between hydrodynamic and mean-field calculation of the critical velocity for both bosonic and fermionic ultracold dilute gases, in the case of a single barrier and a periodic potential in effectively one-dimensional flows. In this section, we will only discuss the main results for superfluid bosons through a single barrier.

Before turning to the study of the dynamics above the critical velocity, let us now consider one important question, which has been raised since the first studies of superfluid instability with helium: is there a general criterion which determines the critical velocity ? The relevance of this question is higher in the context of superfluid helium than for dilute BECs, since in the former no reliable equation, a part from the GL in some temperature regimes, can be used to perform a thoroughful study of the stability of the solutions, like the one described above with the GP equation.

A good starting point is provided by the superfluid hydrodynamic equations (1.20)-(1.22). It has been shown [46] that no stationary solution of these equations is permitted if the modulus of the velocity field $\boldsymbol{v}(\boldsymbol{r})$ is equal or larger than the sound speed $c(\boldsymbol{r})$ at any point $\boldsymbol{r}$ in the fluid[2]. Therefore, the condition

$$v(\boldsymbol{r}) = c(\boldsymbol{r}) \tag{2.1}$$

[2]Using the hydrodynamic equations, this argument is valid in one, two and three dimensional flows only in absence of an external potential, such that the presence of the obstacle is implemented through suitable boundary conditions. In one dimension, this holds also in presence of an external potential, thus applies to the repulsive penetrable barrier case we consider in this section.

provides a criterion for instability in the hydrodynamics framework. It is thus interesting to check whether the criterion (2.1) is verified by the GP equation in the hydrodynamic limit.

2.2.1 Overview of the main results

We use the hydrodynamic criterion $v(\boldsymbol{r}) = c(\boldsymbol{r})$ to predict the critical velocity, and compare the latter to the GP mean-field result. We study one dimensional flows through a single repulsive square barrier (as in section 1.6). When the barrier width is around ten times the bulk healing length, the GP critical velocity is in good agreement with the hydrodynamic result.

2.2.2 The hydrodynamic prediction for critical velocity

We consider the one-dimensional GP equation describing the flow of a condensate through a repulsive square well, as described in subsection 1.6.2. The hydrodynamic approximation of the equation for the density (1.40) is obtained by neglecting the quantum pressure term, to get the Bernoulli equation for the stationary flow:

$$\mu = \frac{mj^2}{2n^2} + V_{\text{ext}}(x) + gn \ , \tag{2.2}$$

where the external potential is defined by Eq. (1.39), and the current is given by the continuity equation $j = n(x)v(x) = n_\infty v_\infty$.

In the hydrodynamic framework, as discussed above, the system becomes unstable when the local superfluid velocity, $v(x)$ at some point x is equal to the local sound velocity, $c(x)$. It has been shown in [54] that this coincides with the breakdown of the hydrodynamic stationary solution. Indeed, we observe that $n(x)$ and $v(x)$ exhibit a kink at the point where $v(x) = c(x)$, with a finite jump in the first derivative, and one cannot construct a stationary solution for $v(x) > c(x)$. As in section 1.6, we are always restricting ourselves to subsonic solutions of the hydrodynamic equations, that is, $v_\infty < c_\infty = \sqrt{gn_\infty/m}$.

The local sound speed is obtained by the equation of state, giving

$$mc^2(x) = n\frac{\partial}{\partial n}gn = gn(x) \ . \tag{2.3}$$

Here $c(x)$ depends on x through the density profile $n(x)$.

If the external potential has a maximum at $x = x_0$ (i.e., $V_{\text{ext}}(x_0) = V_{\max}$), then at the same point the density is minimum, $c(x)$ is minimum and $v(x)$ is maximum. This means that the superfluid becomes first unstable precisely at $x = x_0$. In the symmetric repulsive square well

case considered here, $x_0 = 0$ and $V_{\max} = V_0$. The condition for the occurrence of the instability $v(x_0) = c(x_0)$ can be rewritten as

$$m[j_c/n_c(x_0)]^2 = g n_c(x_0), \tag{2.4}$$

where $n_c(x)$ is the density profile calculated at the critical current $j_c = n_\infty v_{\infty,c}$. By inserting condition (2.4) into the Bernoulli equation (2.2) we can eliminate the current, to get

$$n_c(x_0) = \frac{2}{3g}(\mu_c - V_{\max}), \tag{2.5}$$

where $\mu_c = g n_\infty + m v_{\infty,c}^2/2$ is the critical chemical potential. Now, using Eq. (2.5), we can eliminate n_c from Eq. (2.2), and obtain the following implicit relation for the critical current:

$$j_c^2 = \frac{1}{mg^2}\left[\frac{2\mu_c}{3}\left(1 - \frac{V_{\max}}{\mu_c}\right)\right]^3 . \tag{2.6}$$

It is worth noticing that this equation contains only x-independent quantities. It is also independent of the shape of the external potential: the only relevant parameter being its maximum value $V_{\max} = V_0$. Moreover, it can be applied to both bosons and fermions. Its version for bosons in slowly varying potentials was already discussed in Refs. [61, 31] (see also Ref. [49]). By making explicit the dependence of μ_c and j_c on $v_{\infty,c}$, Eq. (2.6) can be transformed into an algebraic cubic equation for the critical velocity $v_{\infty,c}$.

2.2.3 Comparison between GP and hydrodynamic critical velocity

In Fig. 2.1, we plot the critical velocity obtained from the hydrodynamic expression (2.6) (thick solid lines), and compare it with the GP results. The GP critical velocity is obtained, as described earlier, by determining the value of v_∞ at which the two stationary solutions merge, before disappearing.

The plot refers to the case considered in section 1.6: a one-dimensional repulsive square barrier of width $2d$ and height $V_{\max} = V_0$, the superfluid having a bulk constant density n_∞ and velocity $v_\infty \equiv j/n_\infty$ at large distances from the barrier. The critical velocity $v_{\infty,c} = j_c/n_\infty$ is normalized to the value of the sound velocity in the uniform gas, c_∞, with the same bulk density, and is plotted as a function of $V_{\max}/g n_\infty$.

We show the critical velocity for various values of $2d/\xi$. It is evident that the results of the GP equation approach the hydrodynamic prediction for $2d/\xi \gg 1$, as expected.

The limit $V_{\max}/g n_\infty \to 0$ corresponds to the usual Landau criterion for a uniform superfluid flow in the presence of a small external perturbation, i.e., a critical velocity equal to the sound

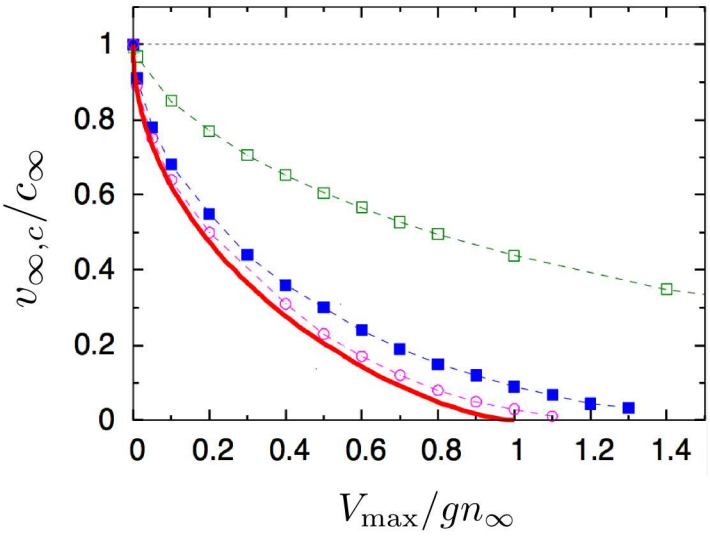

Fig. 2.1: Critical velocity in the case of a repulsive square well, plotted as a function of the maximum of the external potential in units of the chemical potential gn_∞ of the superfluid at rest. The critical velocity is given in units of the sound velocity, c_∞, of a uniform gas with the same bulk density. Thick solid lines: prediction of the hydrodynamic theory, calculated from Eq. (2.6). Symbols: results obtained from the numerical solution of the GP equation (1.38) for various values of $2d/\xi$. Open squares: $2d/\xi = 1$; filled squares: $2d/\xi = 5$; open circles: $2d/\xi = 10$. Dashed lines are guides to the eye.

velocity of the gas c_∞. In the hydrodynamic scheme, the critical velocity decreases when $V_{\max}$ increases mainly because the density has a local depletion and the velocity has a corresponding local maximum, so that the instability occurs earlier. In the limit of weak and thin barriers, our GP results agree with the analytic expression $v_{\infty,c}/c_\infty \simeq 1 - (3/4)(2dV_{\max}/\xi gn_\infty)^{2/3}$ already derived in Ref. [31]; conversely, for thick barriers ($2d/\xi \gg 1$), the $V_{\max} \to 0$ limit of the hydrodynamic expression (2.6) is $v_{\infty,c}/c_\infty \simeq 1 - \sqrt{3/2}\,(V_{\max}/gn_\infty)^{1/2}$ [54]. All curves obtained from the GP equation have a curvature which lies in between these two limiting cases.

The condition for the applicability of the hydrodynamic expression (2.6) is that the typical length scale of the external potential must be much larger than the healing length ξ of the superfluid. For a one-dimensional potential barrier of width $2d$, this implies $2d/\xi \gg 1$. Whenever the critical condition for the instability is reached at a position x_0 far from the barrier edge, at a distance much larger than the healing length ξ, the results for the critical velocity are insensitive

to the details of the shape of the barrier and are expected to be the same for both sharp and smooth barriers. In the hydrodynamic limit, this condition is satisfied and, indeed, our results for the rectangular barrier are consistent with the results discussed in [31] for a generic slowly varying potential. Of course, the hydrodynamic equations would not be reliable in predicting, for example, the behavior of the density distribution near the edge of the barrier, within a distance of order ξ.

Effects beyond hydrodynamics become important when ξ is of the same order or larger than $2d$; they cause a smoothing of both density and velocity distributions, as well as the emergence of solitonic excitations, which are expected to play an important role in determining the critical velocity. This is well known for bosons, where a supercritical current results in the emission of shock waves in classical hydrodynamics and of solitons in the Gross-Pitaevskii theory [31, 71, 54]. For the same reason,the soliton-like branch of the current-phase relation is indeed missing in a hydrodynamic framework, as already shown in the general case of the hydrodynamic junction, section 1.4.

2.2.4 Outlook

We have shown that, in the case of an effectively one-dimensional flow through a repulsive barrier, the hydrodynamic criterion for instability $v(\boldsymbol{r}) = c(\boldsymbol{r})$ is verified by the GP equation when the barrier is sufficiently wide/weak, in order for the local density approximation to apply inside the obstacle. This was expected, since both the hydrodynamic and GP critical velocities correspond to the disappearance of stationary solutions. In the GP equation, this disappearance is, more precisely, a merging of two branches of solutions, a stable plane-wave-like branch and an unstable soliton-like branch.

One aspect which deserves further investigation is the nature of the instability which takes place at the critical velocity. The hydrodynamic criterion $v(\boldsymbol{r}) = c(\boldsymbol{r})$, in the spirit of local density description, can be understood as the local manifestation of the Landau energetic instability of the uniform flow. However, in the GP framework, we just observed a merging and breakdown of stationary solutions, which, as already disscussed, is not strictly related to the true instability, and therefore does not provide information about the nature of the latter. Therefore, a systematic study of the stability of the GP stationary solutions, through Bogoliubov linearized equations, seems necessary in order to fully understand the matter. Such study, in the case of an optical lattice, has been performed in the work from which this section is extracted.

A natural development of this work is the study of similar problems in higher dimensions.

The extensions of the hydrodynamic criterion, and its comparison to GP equation, to fully two- or three-dimensional flows is nontrivial, especially in presence of external potentials creating the weak-link, as well as confining the system. The study of superfluid instability criterion and dissipation dynamics in such configurations will be the subject of the rest of this chapter.

2.3 Phase-slips and superfluid dissipation

In the previous section, we have studied the behavior of the critical velocity using the GP equation to describe a dilute BEC flowing through a weak link in an effectively one-dimensional geometry. We also anticipated that, when the velocity is raised above the critical value, the instability of the system manifests itself through the nucleation of solitons. As we shall discuss in this section, this soliton shedding is the one-dimensional realization of the phase-slip mechanism for the slowdown of a superfluid, first introduced by Anderson [7].

In a phase-slip event, the phase difference across the system drops by 2π, and thereby the critical velocity, according to Eq. 1.15, is decreased by a quantized amount. Due to a phase-slip, the order parameter changes the total number of phase-windings across the system. Therefore, it should be clear that, at some time during a phase-slip event, the order parameter must become zero at one point in space [59].

In the one-dimensional case, when the velocity is dynamically increased above the critical value, the density first forms a notch with increasing depth, which eventually touches zero at the center of the weak link. At this moment, the number of phase windings of the order parameter drops by one unit, and a dark soliton is created inside the weak link, having zero density at its center and a π phase difference across it. The dark soliton subsequently evolves into a gray soliton which drifts away from the weak link, carrying the energy subtracted from the superfluid flow.

In two- or three-dimensional cases, phase-slippage takes place through the nucleation of quantized vortices, as we already mentioned in section 1.4. As discussed by Anderson, since the total phase variation along any closed contour encircling a singly-quantized vortex core must be 2π, the total current drops by a quantized amount when a vortex crosses the system perpendicular to the flow direction.

The mechanism of phase-slippage based on vortex nucleation was proposed by Anderson in the context of superfluid helium. However, ultracold dilute atomic gases present some advantages for the study of superfluid dynamics in general, and in particular can shed new light on the physics

of phase-slips. As already mentioned in section 1.6, with dilute BECs a weak link can be created by a laser beam generating a repulsive barrier for the atoms.

A distinctive feature of ultracold dilute quantum gases rests with the possibility of experimentally interrogate the response of the system in a wide variety of traps and dynamical configurations. Moreover, even if the dilute BEC is described by a GP equation with a contact interaction potential (see section 1.5), and therefore lacks the rotonic part of the helium spectrum, its nonlinearity appears to be the only crucial ingredient needed to reveal the microscopic mechanisms underlying the vortex-induced phase-slips.

On the experimental side, the critical velocity for superfluid instability and some aspects of the dissipation dynamics have been already studied with dilute BECs. The superfluid critical velocity in a harmonically trapped cloud swept by a laser beam has been observed experimentally in [68] and associated with the creation of vortex phase singularities in [35], while solitons were observed in the effectively-one-dimensional geometry of [24]. Such problems have been object of a large theoretical study mainly based on numerical simulations of the GP equation, starting from the seminal work of Frisch, Pomeau, and Rica, studying the instability due to vortex nucleation in a two-dimensional flow past an impenetrable disk [29]. A two-dimensional flow inside a constricted waveguide with inpenetrable walls was studied in [93]. The already mentioned work [31] was devoted to the study of a one-dimensional flow past a repulsive barrier, as done later also in [71]. The phase-slip dissipation caused by a moving barrier inside both a homogeneous and trapped condensate has been studied in two [36, 100, 73], and three [100, 2] dimensions. The production of Cherenkov radiation in this situation was also studied [17].

2.4 Phase-slip dissipation in two dimensions: dilute BEC in a toroidal trap

This section is based on the work: **Vortex-Induced Phase Slip Dissipation in a Toroidal Bose-Einstein Condensate Flowing Through a Barrier**, F.P., L. A. Collins [*Theoretical Division, Mail Stop B214, Los Alamos National Laboratory, Los Alamos, New Mexico 87545*], and A. Smerzi [*INO-CNR, BEC Center, and Dipartimento di Fisica, Via Sommarive 14, 38123 Povo, Trento, Italy*], published in Phys. Rev. A **80**, 021601(R) (2009).

In this section, we will deal with a dilute BEC inside a toroidal trap, where a constriction

for the flow can also be created by an offset of the central hole of the torus. Broadly speaking, such multiply connected configurations allow for the observation of macroscopic phase coherence effects and can lead to a range of important technologies. While superconducting Josephson junctions are already employed in sensors and detectors, their superfluid counterparts can realize ultrasensitive gyroscopes to detect rotations [33]. For instance, a toroidally shaped superfluid weak link provides the building block of a d.c.-SQUID, which is most promising sensing device based on superfluid interference.

Superfluidity of a BEC confined in a torus, in absence of barriers, has been experimentally observed at NIST [80]. The BEC was initially stirred by transfer of quantized orbital angular momentum from a Laguerre-Gaussian beam and the rotation remained stable up to 10 seconds in the multiply connected trap. The metastability of a ring-shaped superflow due to centrifugal forces has been observed in [25].

2.4.1 Overview of the main results

We theoretically study the dynamics of a dilute BEC flowing inside a toroidal trap at zero temperature and in the presence of a repulsive barrier. Similar qualitative results are observed when, rather than by a repulsive barrier, the constriction is created by an offset in the position of the central hole of the torus. As initial condition, we consider a superfluid state with a finite orbital angular momentum in the cylindrically symmetric torus. The critical regime is reached by adiabatically raising the standing repulsive barrier. The dissipation takes place through phase slips created by singly-quantized vortex lines crossing the flow. We find two different critical barrier heights. At the smallest critical height, a singly-quantized vortex moves radially along a straight path from the center of the torus and enters the annulus, leaving behind a 2π phase slip. Eventually, it keeps circulating with the background flow without crossing completely the torus so that it decreases the total angular momentum only by a fraction of unity. At the highest critical height, a singly-quantized anti-vortex enters the torus from the outward low density region of the system. The ensuing vortex dynamics depends on the velocity asymmetry between the inner and the outer edge of the annulus, as well as on the final barrier height and ramping time. For instance, a vortex and an anti-vortex can just circulate on separate orbits or can collide along a radial trajectory and annihilate. When they orbit on the same loop or annihilate, the system undergoes a global 2π phase slip, with the decrease of one unit of total angular momentum. In general, the BEC flow can be stabilized after the penetration of a few vortices. In hydrodynamic regime, we find that the instability towards vortex penetration occurs when the local superfluid

velocity equals the average of the local sound speed along the transverse section of the annulus. This happens inside the barrier region and close to the edges of the cloud.

The results obtained are relevant for toroidal BECs in effectively two dimensional regimes, so that the degrees of freedom along the axial direction do not come into play. Indeed, we have studied the above scenario using numerical simulations of the two-dimensional time-dependent GP equation. We also performed a study with the three-dimensional GP equation, but with a very tight axial confinement, employing the experimental parameters of a squashed toroidal trap created at NIST. However, experiments carried on in the latter setup proved not to be well described by mean-field, and were actually performed to demonstrate the role of quantum fluctuations when dimensionality is reduced [19].

2.4.2 Stationary currents in the toroidal trap

We numerically solve the two-dimensional time-dependent GP equation

$$i\hbar\frac{\partial\psi(\boldsymbol{r},t)}{\partial t} = \left[-\frac{\hbar^2\nabla^2}{2m} + V_{\rm tr}(\boldsymbol{r}) + V_{\rm bar}(\boldsymbol{r},t) + g|\psi|^2\right]\psi(\boldsymbol{r},t). \tag{2.7}$$

The trapping potential is made by a harmonic potential plus a gaussian repulsive core creating a hole in the trap center:

$$V_{\rm tr}(\boldsymbol{r}) = V_{\rm ho}(\boldsymbol{r}) + V_{\rm co}(\boldsymbol{r}) = \frac{\hbar\omega_\perp}{2d_\perp^2}(x^2+y^2) + V_0 e^{-(x^2+y^2)/\sigma_c^2}. \tag{2.8}$$

From now on, we will express quantities in trap units of time $\omega_\perp^{-1}$ and length $d_\perp$. As an initial condition, we consider the numerical ground state obtained with $V_{\rm bar} = 0$, and transfer by linear phase imprinting a total angular momentum $L_z = N\ell$, with N the total number of particles and ℓ integer. The transferred angular momentum is low enough to have flow velocities in the torus region much smaller than the sound speed. Over each loop of radius $r = \sqrt{x^2+y^2}$ the circulation is $C = 2\pi\ell$ and the modulus of the fluid velocity,

$$v(r) = \frac{C}{2\pi r}, \tag{2.9}$$

is constant and directed along the tangent of the same loop. In principle, these ℓ quanta of circulation can be carried by a single multiply-quantized macro-vortex [22], which hovewer breaks up into singly-quantized vortices still confined within the central hole [1].

In our simulations, as soon as a finite angular momentum is transferred to the condensate, the vorticity field component perpendicular to the $x-y$ plane,

$$\nu(\boldsymbol{r},t) = (\nabla\times\boldsymbol{v}(\boldsymbol{r},t))\cdot\hat{z}, \tag{2.10}$$

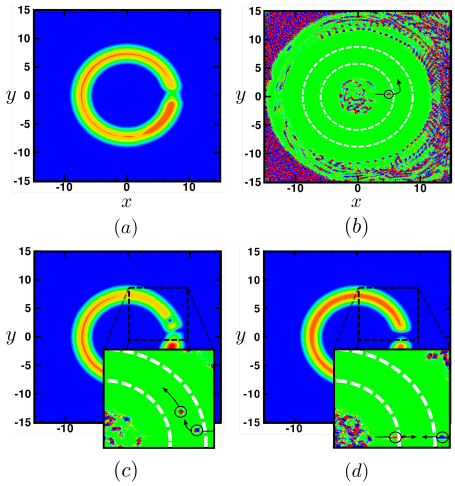

Fig. 2.2: Vortex nucleation and dynamics. (a), (b) and (c) $t_{\rm r} = 10$, $L_z/N = 8$ and $V_{\rm s} = 0.34\ \mu$. (a) $t = 7.6$. Density contour plot with no visible vortex core. (b) $t = 7.6$. The z component of the vorticity field $\nu(\boldsymbol{r})$. The white dashed lines indicates the Thomas-Fermi radii of the cloud. The encircled dot corresponds to a vortex about to enter the annulus from the inner edge. (c) $t = 11.6$. A vortex circulates along the annulus while the vorticity (inset) shows an anti-vortex about to enter. (d) $t_{\rm r} = 10$, $L_z/N = 2$, $V_{\rm s} = 0.61\ \mu$. Vortex anti-vortex annihilation.

shows a "sea" of positive and negative vorticity spots, that is, a mesh of vortices and anti-vortices, see Fig. 2.2 (b). This happens in two regions of very low density, close to the center and in the space surrounding the torus. We can regard the presence of the "vortex sea" as due to numerical noise acting inside very low density regions, possibly triggering an instability of GP equation; we will return to this point in the next section.

We solved the two-dimensional GP equation numerically by a finite-difference real space product formula (RSPF) approach, and employed a spatial grid of 300 to 600 points extending from -15 to $+15$ in both the x and y directions, with a time step of 1×10^{-5} (see [20] for details).

2.4.3 Instability and vortex-nucleation

After angular momentum is transferred to the cloud, the barrier potential $V_{\rm bar}(\boldsymbol{r}, t)$ is adiabatically ramped up over a time $t_{\rm r}$ to a final heigth $V_{\rm s}$. We use a repulsive well with widths w_x centered at the maximum density, and w_y centred at $y = 0$. We always choose $w_x > d$, where

$d \equiv R_2 - R_1$ is the width of the annulus. More precisely, the barrier potential is

$$V_{\rm bar}(\boldsymbol{r}, t) = f(t) V_{\rm s} V_{\rm bx}(x) V_{\rm by}(y), \tag{2.11}$$

with $f(t) = t/t_{\rm r}$ ($f(t) = 1$ for $t > t_{\rm r}$), and

$$V_{\rm bx} = \frac{1}{2}\left(\tanh(\frac{x - R_x + x_0}{b_{\rm s}}) + \tanh(\frac{-x + R_x + x_0}{b_{\rm s}})\right). \tag{2.12}$$

Here R_x is the x-shift of the center of the barrier while its width is $w_x \sim 2x_0$. The other part of the barrier potential, $V_{\rm by}$, has the same shape as $V_{\rm bx}$, but with $R_y = 0$. The final height of the barrier is $V_{\rm s}$ as long as $x_0, y_0 \gg b_{\rm s}$.

While the barrier is raised, the density and velocity field initially adapt to its presence, and the flow shows no sign of excitations. In the barrier region, where the density is depleted, the flow velocity increases mainly at the edges of the annulus. By examining the vorticity, we observe that the two vortex seas are strongly fluctuating, with vortices and anti-vortices trying to escape but being pushed back by zones of higher density. However, when the barrier reaches a critical height $V_{\rm c1}$, a vortex from the inner sea can successfully escape and enter the annulus. As shown in Fig. 2.2 (a) and (b), at $V_{\rm c1}$ the flow can no longer sustain a stationary configuration and becomes unstable. In the example of Fig. 2.2, before raising the barrier, the flow velocity at the maximum density, located at $r_{\rm m} = 7.2$, is $v(r_{\rm m}) = 0.67\ c_{\rm s}$, where $c_{\rm s}$ is Thomas-Fermi estimate of the sound speed in the ground state. The corresponding value of the healing length at $r_{\rm m}$ is $\xi \sim \sqrt{2g\rho(r_{\rm m}, 0)} = 0.28$. The Thomas-Fermi width of the annulus is $d = 3.59$. In this case, the barrier widths are $w_x \sim 4$ and $w_y \sim 2$. The observed critical barrier heights are $V_{\rm c1} \sim 0.14\ \mu$, and $V_{\rm c2} \sim 0.24\ \mu$.

In Fig. 2.2 (a), we observe the depletion of the density but not a visible vortex core. However, if we inspect the the vorticity field (2.10) plotted in Fig. 2.2 (b), we clearly see an isolated red spot, corresponding to a positive vorticity, moving radially from the center of the torus towards the higher density region, indicating the presence of the core of a singly-quantized vortex. In the literature, phase singularities appearing inside strongly depleted regions have been referred to as "ghost vortices" [96] .

The above scenario for vortex nucleation in a multiply connected geometry confirms that a persistent flow in such a configuration is possible because of the pinning of the vorticity in the low density regions near the center and outside of the torus. An explanation of this pinning has been given, based on the existence of an effective energy barrier felt from a vortex core when trying to move towards a region of much higher density [16, 60, 95, 51]. This effective energy barrier arises

from the nonlinearity of the GP equation. Within this interpretation, the obstacle raised across the annulus serves to unpin singly-quantized vortices by steadily decreasing the density during the ramping process, up to suppression of the effective energy barrier. The density depletion occurs on a radial stripe and makes way for the vortex moving outwards along a straight line connecting the center of the vortex with the barrier. This as well happens for the anti-vortex moving inwards at a larger height of the repulsive barrier, see below.

The above energetic argument should provide an energetic criterion for the superfluid instability. In the sections 2.1 and 2.2, we discussed a different criterion, see Eq. (2.1), coming from hydrodynamics, and studied its validity within one-dimensional GP equation. As already noted in subsection 2.2.4, the nature of both the hydrodynamic and full GP instability is not understood, and therefore the connection to the above energetic argument is nontrivial. Moreover, while for one-dimensional GP equation we verified the local hydrodynamic criterion (2.1) in the proper weak/broad barrier regime, in the present two-dimensional problem we find a different result.

Indeed, in the hydrodynamic regime, when $\xi \ll d, w_x, w_y$ and $V_s \ll \mu$, we observe the instability towards vortex penetration when the local superfluid velocity reaches the "true" sound speed [103]. The latter is calculated at the maximum of the repulsive well (at $y = 0$ in our case) with the density integrated along the radial direction. This critical condition is first met inside the barrier region, at the Thomas-Fermi radius of the cloud.

This criterion is different from the local criterion (2.1) insofar as it involves the true sound speed and not the local sound speed, and the latter should be compared to the superfluid velocity at the Thomas-Fermi radius of the cloud. In the next section, we will return, giving quantitative results, to the study of this new criterion.

The parameters of Fig. 2.2, have been chosen such that the system is outside the hydrodynamic regime, in order to emphasize the generality of the presented vortex dynamics phenomenology.

2.4.4 Phase-slips

As we discussed in the previous section, the passage of a vortex core between two points causes a 2π slip in the phase difference between them. In Fig. 2.3, we observe 2π sharp drops in the circulation C on a given loop of radius r at the moment the vortex core crosses it. The larger the loop radius r, the later the vortex core reaches it and creates the phase slip. The fact that the circulation at small (and large) radii is not exactly integer, but slightly larger, is due to

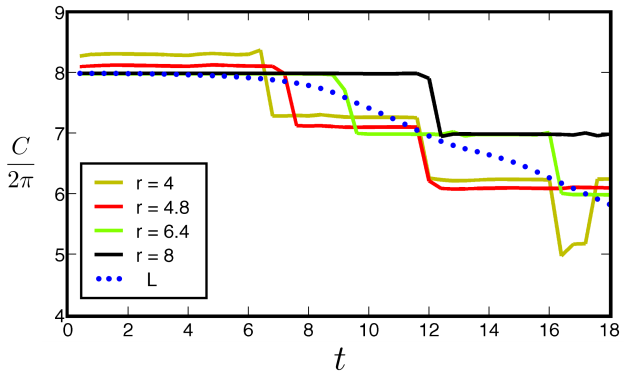

Fig. 2.3: Circulation (solid lines) for loops with different radii and total angular momentum (dots) as a function of time. The parameters are the same as in Fig. 2.2(a). The 2π drops in the circulation at $r = 4, 4.8, 6.4$ are due to a singly-quantized vortex moving outwards from the center. The drop at $r = 8$ and $t \sim 12$ is due to the passage of an anti-vortex entering the annulus from the outer edge. The oscillation in the circulation at $r = 4$ and $t \sim 16 - 17$ is due to a double crossing of a vortex trying to escape the inner region.

numerical difficulties related to the calculation of the velocity field where the density is very small. However, even at $r = 4$, where the density is small, we see single 2π phase slips taking place at regular intervals and corresponding to vortex core crossings. Moreover, at small radii, close to the inner sea of vortices, the circulation shows spikes at which it decreases by 2π, then quickly goes back to its previous value. These are associated with a vortex moving out of the sea but being pushed back by a region of high density located slightly outwards, as discussed above. Indeed, in this way, a loop is crossed back and forth by the same vortex. We have observed a similar effect with anti-vortices trying to enter the annulus from the outer vortex sea.

Due to phase slippage, the angular momentum is reduced, and eventually the system becomes stable again after a finite number of spawned vortices. The circulation is lowered by a few quanta, and the fluid velocity on vortex-crossed loops is brought back below the critical value. If the ramping is stopped at V_{c1}, only the inner edge of the annulus is unstable since its fluid velocity is larger ($v(r) \propto \ell/r$). In this case, vortices do not cross completely the torus and move on stable circular orbits. The vortices circulate on a fixed loop within our computational times. Vortices orbiting inside a two-dimensional toroidal trap have been studied with GP equation in [62, 63].

However, when the barrier reaches a second critical height $V_{c2} > V_{c1}$, the outer part of the

annulus becomes also unstable. Anti-vortices then enter from outwards while vortices enter the inner edge, as previously discussed. Anti-vortices move radially inwards and contribute to stabilize the outer part by phase slips. Indeed, an anti-vortex crossing a loop makes the circulation drop as a vortex crossing the opposite way.

In Fig. 2.2(c) we see a vortex already circulating inside the high density region of the annulus while an anti-vortex begins to enter. The separation between V_{c1} and V_{c2} is proportional to the velocity difference $\Delta v = \ell(R_1 - R_2)/(R_1 R_2)$ between the two edges. In general, depending on Δv, the dynamics at barrier heights larger than V_{c2} can vary. For instance, at lower angular momenta Δv becomes smaller, and a vortex and an anti-vortex enter the annulus almost simoultaneously. They can then collide and annihilate, as shown in Fig. 2.2(d). When a vortex and an anti-vortex annihilate or separately orbit on the same loop, the system undergoes a global 2π phase slip, and the total angular momentum is decreased by one unit.

2.4.5 Three-dimensional calculations in a squashed torus

We extended our two-dimensional calculations into a three-dimensional configuration. The parameters of the squashed toroidal trap are those employed experimentally at NIST. To transfer angular momentum to the cloud, we use a Laguerre-Gaussian beam. We employ an harmonic trapping with $\omega_\perp = 2\pi \times 20$ Hz (such that $d_\perp = 4.69$ μ) and $\omega_z = 48\omega_\perp$. The Laguerre-Gaussian beam is modelled by a proper external potential term in the GP equation [87]. The core repulsive potential is $V_{co}(r,z) = -V_c(r/\sigma_c)^2 e^{-2(r/\sigma_c)^2}$, and the resulting condensate has a shape close to a hollow disk. We add a repulsive well potential of the same kind used in two dimensions, whose shape, however, is not crucial in determining the qualitative features of the dissipation, as long as w_x is larger than the width of the annulus. We solve the three-dimensional GP equation numerically by a finite-element discrete variable representation in the spatial coordinates and a RSPF in time. The x and y coordinates were divided into boxes of span $[-20.0, +20.0]$ with 160 elements and order 5 Gauss-Legendre bases while the z-direction covered a box $[-10.0, +10.0]$ with 80 elements of order 5 bases. The time step was 1×10^{-5} (see [81] for details).

Since the healing length is of the order of the harmonic lenght along z, we found, as expected, that the nucleation of singly-quantized vortex lines and their dynamics resemble those observed in two-dimensional calculations. In particular, we have two critical values for the barrier height V_{c1} and V_{c2} connected respectively with the nucleation of vortices or both vortices and anti-vortices.

2.4.6 Outlook

The study of the instability scenario in fully three dimensional cases, where the degrees of freedom along all the three directions play a role, represents a necessary extension of the present work. Indeed, a part from the fundamental interest in understanding how the phase-slippage dynamics takes place in three dimensions, recent experimental results have shown that the squashed torus case studied here is not a good candidate for a clean observation of critical velocity for superfluid dissipation, due to the large quantum fluctuations caused from the tight axial confinement. On the other hand, the other toroidal trap used at NIST to demonstrate persistent currents [80], with a larger axial size, seems a promising one.

Another interesting observation which deserves further investigation, is the discovery of a new instability criterion, different from the local criterion (2.1) coming from superfluid hydrodynamics.

These issues will be the object of the next section.

2.5 Phase-slip dissipation in three dimensions: the role of confinement asymmetry and the instability criterion

This section is based on the work: **Instability and Vortex Rings Dynamics in a Three-Dimensional Superfluid Flow Through a Constriction**, F.P., L. A. Collins [*Theoretical Division, Mail Stop B214, Los Alamos National Laboratory, Los Alamos, New Mexico 87545*], and A. Smerzi [*INO-CNR, BEC Center, and Dipartimento di Fisica, Via Sommarive 14, 38123 Povo, Trento, Italy*], arXiv:1011.5041v1.

2.5.1 Overview of the main results

In this manuscript, we study the critical velocity and superfluid dissipation mechanism in a three-dimensional constricted flow configuration, where the size of the cloud along all the three directions is much larger than the healing length ξ. We consider a subsonic flow of a zero-temperature dilute BEC, and numerically solve the GP equation in two different geometries: a wave guide with periodic boundary conditions, which can mimic an elongated cloud along the flow direction, as created in the experiments of [24, 85], and a torus, already introduced in

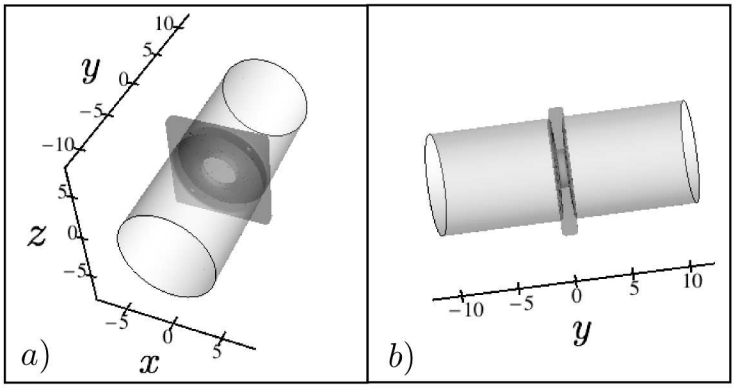

Fig. 2.4: Constriction configuration. The light-gray surface corresponds to the classical (Thomas-Fermi) surface of the cloud. The dark-gray surface shows an isosurface of the barrier potential used to create the constriction.

the previous section. The unstable regime is reached by raising a repulsive penetrable barrier perpendicular to the flow. This barrier is broader than the cloud transverse size, and extends over a few (typically 5 to 10) healing lengths along the flow direction. In this way, we create a constriction for the flow in the barrier region, as shown in Fig. 2.4. Starting from a stationary flow with a given velocity, the barrier is adiabatically raised during the dynamical evolution until the instability sets in, and we observe vortex rings penetrating the cloud, and taking energy off the supefluid flow by the same phase-slip mechanism described earlier.

The two geometries under study present significative differences in the vortex ring nucleation and dynamics. We find that vortex rings, which can find a stationary configuration after entering an axially symmetric waveguide, are instead always transient in the torus, and, more generally, as soon as the axial symmetry about the direction of flow is broken.

Finally, we observe that, in the hydrodynamic regime of GP equation, the instability criterion which determines the critical velocity is not given by the local condition (2.1). We indeed verify, consistently with the the criterion we found in the two-dimensional case treated in the previous section, that the instability sets in as soon as the fluid velocity at the Thomas-Fermi surface of the cloud equals the true sound speed, which in this case is the local sound speed averaged over the transverse section of the waveguide/annulus.

2.5.2 The model

In order to study these various configurations, we solve the time-dependent GP equation (2.7) for three spatial dimensions in scaled form as

$$i\hbar\frac{\partial\psi(\boldsymbol{r},t)}{\partial t}=\left[-\frac{1}{2}\nabla^2+V(\boldsymbol{r},t)+g|\psi|^2\right]\psi(\boldsymbol{r},t) \tag{2.13}$$

where length, time, and energy are given in units of $d_o=[\frac{\hbar}{m\omega_o}]^{\frac{1}{2}}$, $1/\omega_o$, and $\hbar\omega_o$ respectively for a representative harmonic frequency ω_o that characterizes the trap. $V(\boldsymbol{r},t)$ is the external potential. The condensate wavefunction $\psi(\boldsymbol{r},t)$ is normalized to the total number of particles N. The external potential has components associated with the trapping and the barrier potentials of the form

$$V(\boldsymbol{r},t)=V_{\rm tr}(\boldsymbol{r})+V_{\rm bar}(\boldsymbol{r},t). \tag{2.14}$$

In both cases, we find the ground state of the system with $V_{\rm bar}=0$.

The waveguide geometry is implemented by choosing the trapping potential

$$V_{\rm tr}(\boldsymbol{r})=\frac{1}{2}[x^2+\gamma^2z^2]\ , \tag{2.15}$$

with $\omega_o\equiv\omega_x=30\times2\pi$Hz, $\gamma=\omega_z/\omega_x$, and periodic boundary conditions along the flow direction y. We considered three different values of the γ, namely 1, 1.05, and 1.2, which correspond, respectively, to a ground state chemical potential $\mu=11.7,\ 12.0,\ 16.5$ with $N=3\times10^5$ ^{87}Rb atoms and a nonlinear scaling value $g\ N=10134$.

The toroidal geometry is implemented by choosing the trapping potential

$$V_{\rm tr}(\boldsymbol{r})=\frac{1}{2}[\alpha^2x^2+\beta^2y^2+z^2]+V_c\ e^{-2(\rho/\sigma_c)^2}\ , \tag{2.16}$$

where $\alpha=\omega_x/\omega_z$ and $\beta=\omega_y/\omega_z$. We take $\alpha=\beta=0.5$ with $\omega_o\equiv\omega_z=25\times2\pi$Hz and form the torus by including a core potential with parameters $V_c=144$, and $\sigma_c=1.88$ with $\rho^2=x^2+y^2$. The ground state chemical potential is $\mu=7.6$ for $N=2.5x10^5$ ^{23}Na atoms, corresponding to a nonlinear scaling value $g\ N=2028$.

During the dynamical evolution, we use a time-dependent barrier potential of the same kind used in the two-dimensional calculations of the previous section (see Eq. (2.11)):

$$V_{\rm b}(\boldsymbol{r},t)=f(t)V_{\rm s}V_{\rm bx}(x)V_{\rm by}(y)V_{\rm bz}(z)/8, \tag{2.17}$$

with $f(t)=t/t_{\rm r}$ ($f(t)=1$ for $t>t_{\rm r}$) and $V_{\rm bx}=\tanh(\frac{x-R_x+x_0}{b_{\rm s}})+\tanh(\frac{-x+R_x+x_0}{b_{\rm s}})$. Here R_x is the x-shift of the center of the barrier while its width is $w_x\sim2x_0$. $V_{\rm by}(y)$ and $V_{\rm bz}(z)$ have the same form as $V_{\rm bx}$. The final height of the barrier is $V_{\rm s}$ as long as $x_0,y_0,z_0\gg b_{\rm s}$.

Before starting the dynamics, we put the condensate in motion by imprinting an appropriate spatially dependent phase $\theta(\boldsymbol{r})$ on the wavefunction. In the waveguide case, $\theta(\boldsymbol{r}) = mvy/\hbar$ generates a uniform flow of velocity v along the y direction. In the torus, $\theta(\boldsymbol{r}) = ml\phi/\hbar$, with l integer, generates a tangential flow of speed $v(r) = l/\rho$, where $\phi = \arctan(y/x)$.

The results presented in this manuscript are obtained by solving numerically the GP equation. After finding the ground state with an imaginary-time propagation, we perform the dynamical evolution in real time. For all the simulations performed we used a finite-element discrete variable representation (DVR)[81]. In the waveguide geometry, we employed a split-operator method, with a Fast-Fourier-Transform algorithm used for the kinetic part of the evolution, while for the simulations in the torus we used a Real Space Product Formula [81]. The spatial grid for the waveguide calculations was $n_x = 60, n_y = 120, n_z = 60$ (or $n_x = 180, n_y = 120, n_z = 180$ for Figs. 2.7 and 2.8) with box sizes $L_x = 12, L_y = 24, L_z = 12$ for the axially symmetric case (see below), $n_x = 90, n_y = 120, n_z = 80$ with box sizes $L_x = 18, L_y = 24, L_z = 16$ for the axially asymmetric case, while the time-step was $dt = 10^{-4}$. In the torus simulations, we used a spatial grid consisting of 80 elements in each dimension with 4 DVR Gauss-Legendre functions in each element spanning cubic box lengths of $[-12, 12]$, $[-12, 12]$, and $[-10, 10]$ in the x, y, and z-directions respectively. This choice gave 241 grid points in each direction. We also tested the convergence with 5 basis functions and 321 points with only a few percent change in basic quantities such as energies, momentum, and positions.

2.5.3 Criterion for instability

In the hydrodynamic regime, when the healing length ξ is much smaller than all other length scales (the smallest of which is the barrier width along the flow direction), we find that the onset of instability coincides with a simple condition, $v_{\rm TF} = c$: inside the barrier region, the local fluid velocity at the classical (Thomas-Fermi) surface of the cloud, $v_{\rm TF}$, equals the sound speed c, as depicted in the inset of Fig. 2.5. It is important to precisely define the sound speed which sets the threshold for the critical velocity. The latter is the Bogoliubov sound speed, calculated inside the barrier region, for the low-lying modes propagating along the flow, taken as if the system was homogeneous in this direction. In the present case of a harmonic transverse confinement, and within the Thomas-Fermi approximation, this sound speed is simply the average of the local sound speed on a plane perpendicular to the flow $c = c(0)/\sqrt{2}$, where $c(0)$ is the local sound speed at the center of the transverse harmonic trap [103].

We verified this numerically in the waveguide case, as shown in Fig. 2.5. In a waveguide

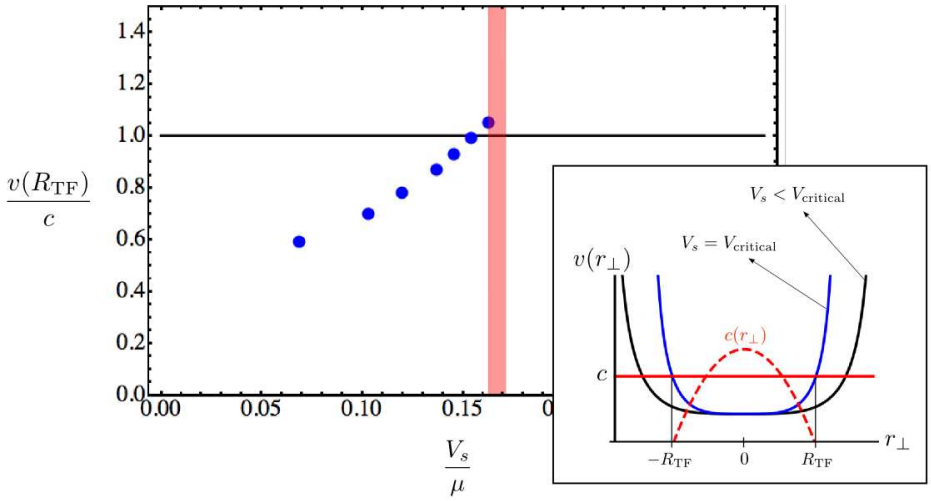

Fig. 2.5: Ratio of the higher local fluid velocity at the Thomas-Fermi radius, $v(R_{TF})$, to the sound speed c inside the barrier, as a function of the barrier height. The red-shaded area correspond to the critical point plus uncertainty. The results are obtained for the cylindrically symmetric waveguide $\gamma = 1$ and initial flow velocity $v = 1.05$. The inset shows a sketch of the behavior of the local fluid velocity along a radial cut inside the barrier region. The red solid line indicates the value of the sound speed c, which with transverse harmonic confinement is just the average of the local sound speed, $c(r_\perp)$ (red dashed line) over the transverse plane. The black(blue) solid line corresponds to a subcritical(critical) condition.

with cylindrical symmetry, the condition $v_{\rm TF} = c$ is verified simultaneously at points on a circle perpendicular to the flow, from where a vortex ring will then enter. In the torus, due to a higher flow speed at the inner edge of the annulus, the critical condition is reached first on the interior of the cloud, with the consequence that vortex rings, if ever formed, must be asymmetric, as we discuss below.

This criterion allows for a simple understanding of the details of vortex penetration dynamics, based on the observation that vortex cores enter first where the critical condition if first reached.

As discussed in the previous section, we verified the same condition for instability to hold for a two-dimensional toroidal BEC.

Already below the critical point, we observe vortices getting closer to the edges of the cloud but failing to enter. The presence of these "ghost" vortices (see previous section), suggests that a pre-instability is triggered at the edges of the condensate, but, since the vortices do not enter the bulk region, it is not sufficient to dissipate the superflow. This observation can help building a

connection between the present criterion and the local criterion (2.1). As anticipated, the latter is clearly not valid here, since it would predict the flow to be always unstable for the simple reason that the local sound speed goes to zero at the edges of the waveguide, and therefore condition (2.1) is always met, even before raising the obstacle. However, even though not giving the condition for the real instability, the local criterion can be signalling the onset of the above pre-instability. Indeed, the latter is present as soon as the fluid moves, since a vortex sea (see previous section) is formed, and the ghost vortices which try to enter the cloud before the critical velocity come out of this fluctuating sea.

2.5.4 Instability dynamics in the waveguide

In analogy with the standard situation where a superfluid flows through a channel, we consider a waveguide with periodic boundary conditions along the flow direction y, and the barrier creating the equivalent of the channel. This situation can be realized experimentally with a BEC inside an elongated trap along the flow direction. As stated above, before raising the barrier in the simulations, a stationary flow is created by imprinting a phase $mvy/\hbar$ on the condensate wavefunction, where v is the constant flow speed. This corresponds in the experiment to sweeping the barrier across the cloud at a constant velocity. We consider a symmetric harmonic confinement in the transverse $x-z$ plane, such that $d_x = \sqrt{\hbar/m\omega_x}$ and $d_z = \sqrt{\hbar/m\omega_z}$ are both sufficiently larger than the bulk healing length. The effect of transverse degrees of freedom comes thus into play, giving rise to a fully three-dimensional dynamics. Such a setup has been used in [85], where, moreover, the possibility of creating a penetrable repulsive barrier with a control over a length comparable to the healing length has been demonstrated.

In this configuration, as soon as the critical barrier height is reached, a vortex ring detaches from the system boundaries and starts shrinking into the cloud inside the barrier region, as shown in Fig. 2.6, a). In the figure, black points indicate the position of vortex cores while the gray surface corresponds to the Thomas-Fermi surface of the cloud. Detection of vortex cores is performed using a plaquette method, described in [28].

Let's observe that a vortex ring shrinking into the cloud is the three-dimensional analogue of the penetration of a vortex-anti-vortex pair in two dimensions, shown in Fig. 2.2(d). Indeed, vortex core located at opposite sides of a circular vortex ring carry opposite vorticity.

Depending on the initial flow velocity, waveguide transverse section, and barrier height at the critical point, the ring attains a certain radius and velocity with which it propagates in the flow direction in a stable fashion, as long as axial symmetry is preserved, as depicted in Fig. 2.6, c)

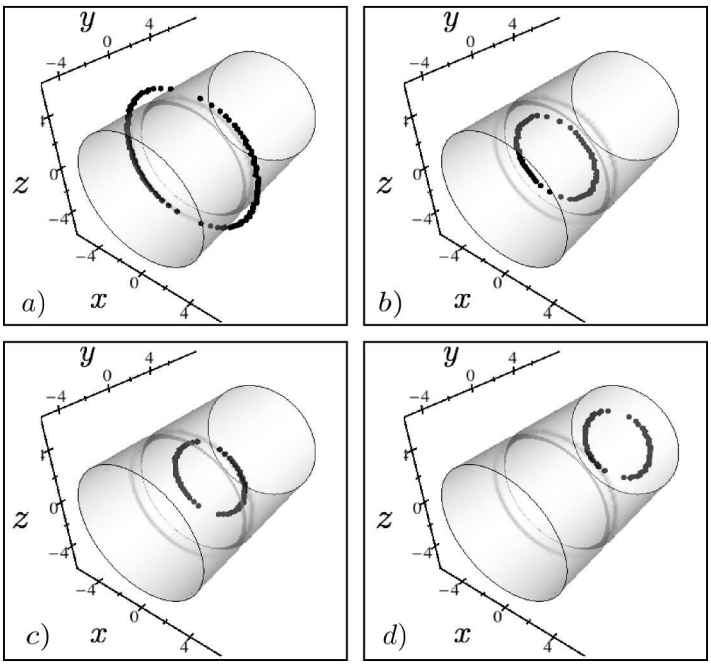

Fig. 2.6: Four subsequent stages of the vortex ring penetration in the waveguide. The gray surface indicates the position of the Thomas-Fermi surface of the condensate. Black dots show the position of the vortex cores. Here the waveguide is axially symmetric $\gamma = 1$, the initial flow velocity is $v = 1.05$, and the final barrier height is $V_s = 0.17\mu$. a) The ring is shrinking around the cloud in barrier region, still outside the Thomas-Fermi borders of the cloud. b) The ring has just entered the cloud. c) The ring has shrunk to its final size and is already outside the barrier region, moving along the flow direction. d) The ring has moved far from the constriction region, with a constant speed and radius.

and d). Here the vortex ring eventually propagates at the speed $u_{\mathrm{r}} = 0.65$, and a radius $R = 2.9$.

For sufficiently strong barriers, the ring shrinks to a point, thereby annihilating and completing a full single phase-slip, as shown in Fig. 2.7. After this process, the velocity has dropped everywhere by the same quantized amount. Again, such an event is the three-dimensional analogue of vortex-anti-vortex annihilation in two dimensions.

It is interesting to analyze the ring annihilation event in more detail. In Fig. 2.8 a) and b), respectively, we show the position of the vortex cores toghether with the density on a plane parallel to the flow direction, at a time just before and just after the ring has shrunk to a point. In Fig. 2.8 c), the density on the same plane is plotted at four subsequent times after the annihilation. The details of self-annihilation process which we observe are consistent with the

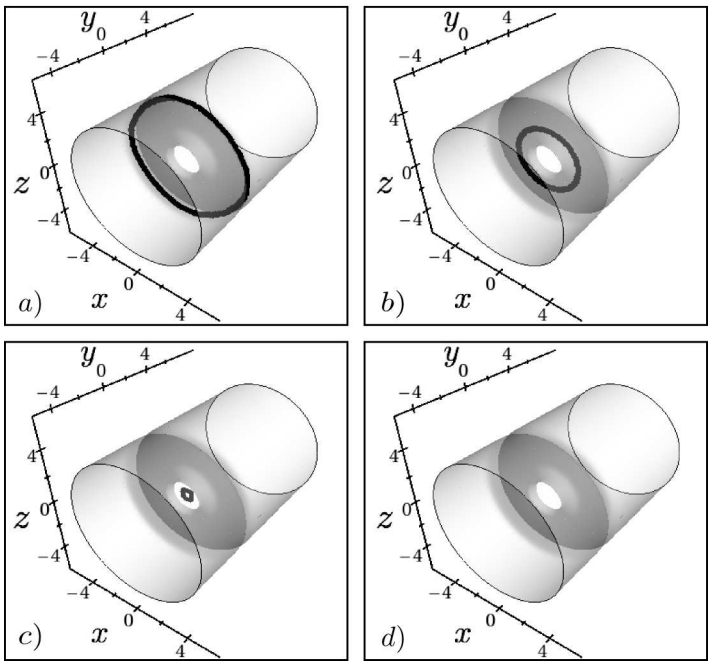

Fig. 2.7: Four subsequent stages of the vortex ring annihilation in the waveguide. The gray surface indicates the position of the Thomas-Fermi surface of the condensate. Black dots show the position of the vortex cores. Here the waveguide is axially symmetric $\gamma = 1$, the initial flow velocity is $v = 0.52$, and the final barrier height is $V_s = 0.94\mu$. a) The ring is shrinking around the cloud in the barrier region, still outside the classical borders of the cloud. b) The ring has entered the cloud. c) The ring is about to shrink completely and annihilate. d) The ring has annihilated and no vortex core is now inside the Thomas-Fermi surface.

previous studies of axisymmetric vortex ring solutions [41, 40, 15, 45, 76]. Namely, if we consider the position of the vortex cores, we see that the points of phase singularity form a loop which shrinks inside the constriction, Fig. 2.8 a), and whose radius eventually becomes zero, Fig. 2.8 b). At this moment, we see the zero-density core being filled with atoms, thereby transforming into a density depression, which further propagates out of the constriction as a rarefaction pulse, as shown in Fig. 2.8 c). Finally, this rarefaction pulse decays into sound.

Both in Figs. 2.6 and 2.7, we see that, at least initially, the vortex cores are subjected to an essentially radial motion, corresponding to the shrinking of the vortex ring. This behavior can be understood by considering what contributes to the motion of vortex cores in non-homogeneous systems [67]. Let us consider a single vortex core located at some position x_c. Its velocity is the sum of two terms: i) the background flow velocity at x_c, and ii) a term perpendicular to the

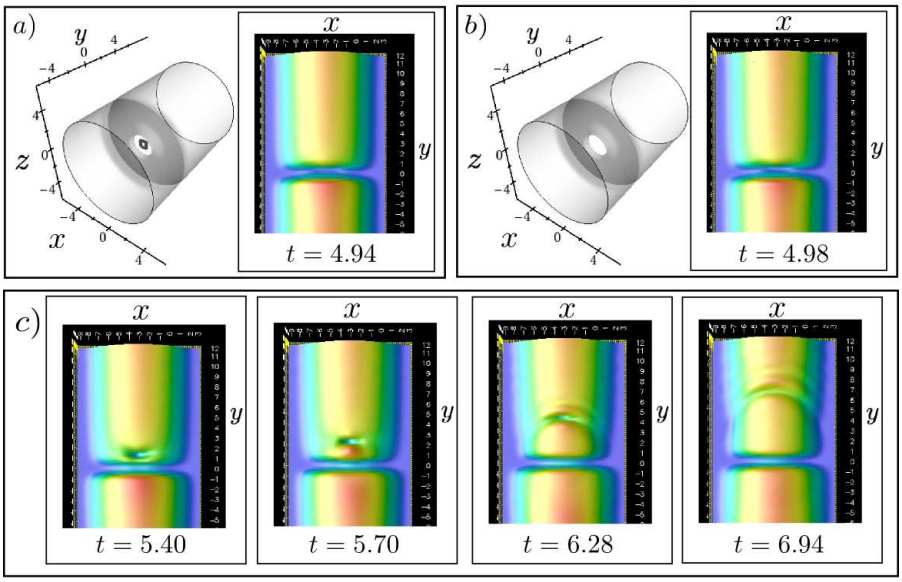

Fig. 2.8: Details of the ring self-annihilation event studied in Fig. 2.7, at six subsequent times. In a) and b), left panel, the gray surface indicates the position of the Thomas-Fermi surface of the condensate, while black dots show the position of the vortex cores. In a) and b), right panel, and c), the density on a $z = 0$ plane parallel to the flow direction is shown. A very small loop structure of vortex cores, in a), shrinks to a point and has disappeared in b). The ring has transformed into a rarefaction pulse, whose propagation and decay into sound appears in c).

gradient of the density at x_c. Both contributions must be calculated as if the vortex was not present. Since the relative weight of term ii) is proportional to the value of the healing length calculated at x_c, in high density regions, a vortex core will move mainly with the background superfluid velocity, while in low density regions, it will move mainly due to the gradient of the density. Therefore, when the vortex ring is inside the constriction, where the density is low, and especially when it is close to the Thomas-Fermi surface, it will principally move perpendicular to the gradient of the density, whose main contribution comes from the density modulation induced by the barrier along the flow direction. This results in an essentially radial motion of the cores, and thus into the shrinking of the ring.

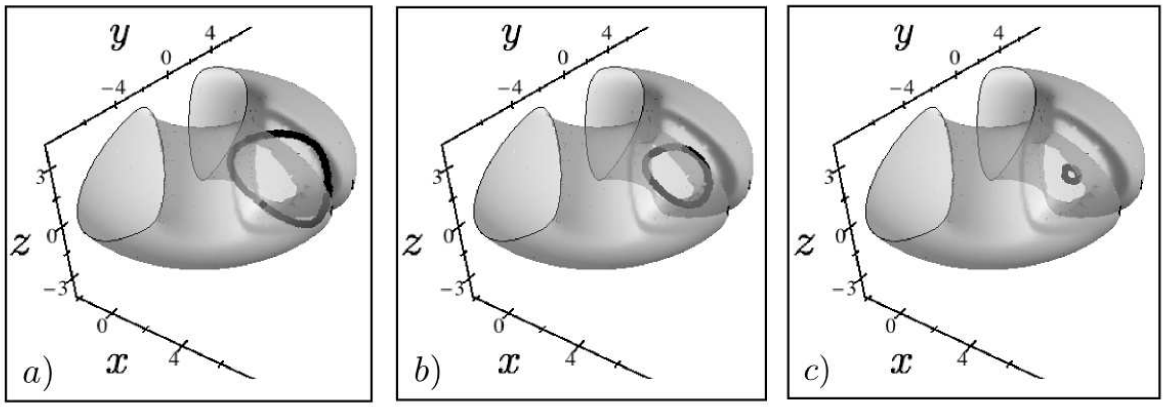

Fig. 2.9: Three subsequent stages of the vortex ring annihilation in the torus. The gray surface indicates the position of the Thomas-Fermi surface of the condensate. Black dots show the position of the vortex cores. Here the initial circulation is $l = 1$, and the final barrier height is $V_s = 0.5\mu$. a) The ring is shrinking around the cloud in barrier region, still outside the classical borders of the cloud. b) The ring has entered the cloud. c) The ring is about to shrink completely and annihilate.

2.5.5 Instability dynamics in the torus

In the toroidal geometry, the scenario is richer since, as already discussed in the previous section, the tangential flow velocity at a given total angular momentum, due to the conservation of quantized circulation, decreases like 1/r, where r is the distance from the center of the torus. This introduces an asymmetry between the inner and the outer edges of the cloud, which is not present in the waveguide case. In three-dimensional configurations, the result is that vortex rings are transient features in a toroidal geometry.

The ring vortex either breaks or shrinks to a point and annihilates for sufficiently strong barriers. While the annihilation process, shown in Fig. 2.9, is very similar to the one taking place in a waveguide, the vortex ring breaking mechanism reflects instead more evidently the asymmetry in the velocity field.

As shown in Fig. 2.10, the ring is strongly deformed since the inner part moves faster (the

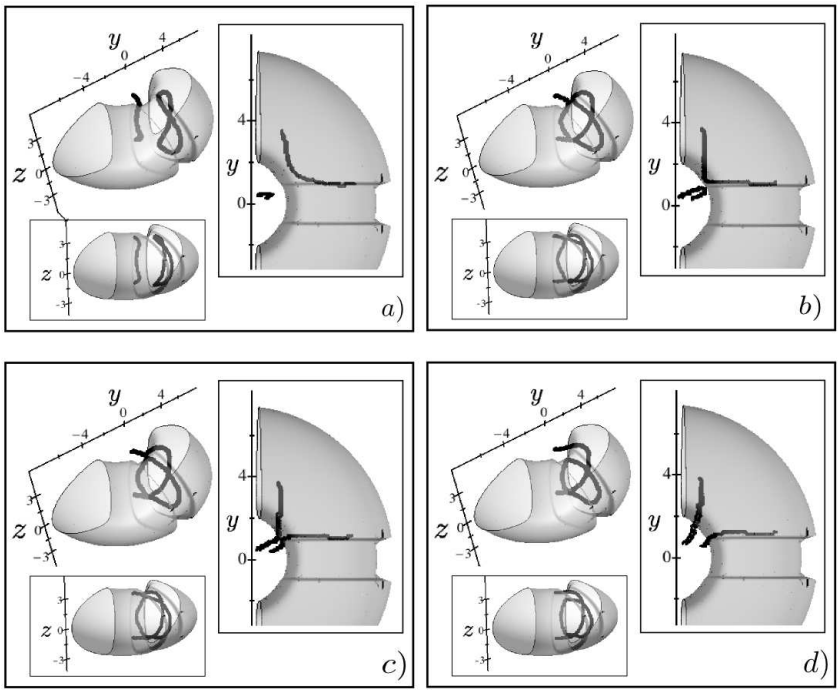

Fig. 2.10: Four subsequent stages of the vortex ring breaking in the torus. The gray surface indicates the position of the Thomas-Fermi surface of the condensate. Black dots show the position of the vortex cores. Insets show the top and side views. Here the initial circulation is $l = 4$, and the final barrier height is $V_s = 0.2\mu$. a) The vortex ring is bending to form a right angle. b) The vortex ring has formed a right angle whose vertex is close to a vortex line coming frome the center of the torus. c) The vortex ring and line have just reconnected: a vortex line and a portion of a ring vortex are now inside the Thomas-Fermi surface. d) The vortex line and the ring have moved apart.

velocity of a vortex core, when the healing length is much smaller than the length scale of density variation, is essentially given by the background flow velocity [67]). The deformation increases in time up to the point at which the ring bends in on itself, forming a right angle at whose vertex a kink is present, as shown in Fig. 2.10 b). Meanwhile, a vortex line coming from the inner core of the torus approaches the vertex, also forming a kink in correpondence to the latter. Eventually, the line and the ring connect, joining each other at the position of the kinks. Such an event produces a vortex line plus a new ring vortex, appearing in Fig. 2.10 c). Thus, the breaking

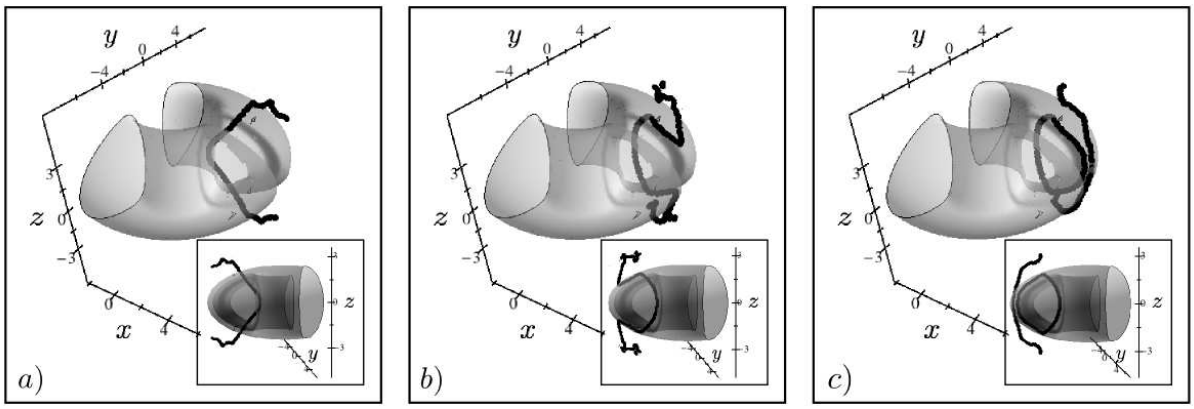

Fig. 2.11: Three subsequent stages of the vortex ring formation in the torus. The gray surface indicates the position of the Thomas-Fermi surface of the condensate. Black dots show the position of the vortex cores. Insets show the side view. Here the initial circulation is $l = 4$, and the final barrier height is $V_s = 0.2\mu$. a) The vortex line is bending around the cloud in barrier region, partially outside the Thomas-Fermi borders of the cloud. b) The vortex line has developed two kinks. c) The vortex ring has just formed.

is actually a vortex reconnection. Vortex reconnections play an important role in turbulent scenarios, being a very efficient mechanism for increasing the number of vortices in the system [98].

When the barrier is not strong enough to make both the edges of the annulus unstable, we also observed cases in which the ring is not formed at all, and a strongly bent vortex line enters the cloud from its inner edge, to circulate around the torus. The fact that the vortex line enters the inner edge of the annulus is due to the above mentioned asymmetry in the velocity field, decaying as the inverse of the distance from the center of the torus, which makes the instability set in there first, according to the criterion discussed in section 2.5.3.

The formation of a vortex ring in the torus is very interesting, since it can be seen as a reconnection of a vortex line with itself. As shown in Fig. 2.11, a bended vortex line is always present at first. While the bending increases, the vortex line develops two sharp kinks whose tips get closer to each other, up to when they join, thereby cutting the original line into a vortex ring plus a yet another line. The latter is then reabsorbed at the system's boundary.

2.5.6 Changing from two to three dimensions

When the condensate is effectively in two dimensions, meaning that the cloud size along the third direction is comparable with the healing lentgth ξ, vortex lines oriented along the direction of tighter confinement can become the preferred excitations with respect to vortex rings [27]. In the previous section, studying a condensate inside an effective two-dimensional toridal trap (the system's size along the axis of the torus was about one healing length), we indeed observed that superfluid dissipation took place through the formation of vortex lines entering the cloud.

For the trap configurations considered here, we have observed vortex ring formation in the very low density regions outside the condensate classical Thomas-Fermi surface. As suggested before, we could call these ghost vortices, since they are not visible from the condensate density profile. In some cases, these ghost vortex rings are able to enter completely the classical surface of the cloud, transforming into what we should then call "real" ring vortices. In the crossover between effective two- and three-dimensional regimes, moving from a scenario in which only vortex lines are present to one in which real vortex rings come into play, it is reasonable to expect an intermediate regime in which ghost vortex rings are formed, but the condensate is sufficiently squashed along the third dimension that the full vortex loop is not able to enter the cloud's classical surface. In this regime, superfluid would be dissipated by vortex rings which are partly real and partly ghost, appearing as simple bent vortex lines in the density profile.

An example of such situation is given in Fig. 2.12, where the waveguide is non-axially symmetric about the flow direction ($\gamma = 1.2$). After the instability sets in, a ghost vortex ring forms and shrinks around the cloud in the barrier region up to when we observe a full-fledged ring vortex, which is only partially inside the Thomas-Fermi surface of the condensate (Fig. 2.12a)). However, since the part of the ring which is inside the Thomas-Fermi surface moves with a larger speed along the flow direction with respect to the part which remains outside, the ring vortex is soon deformed (Fig. 2.12b)), and eventually breaks up (Fig. 2.12c)). The vortex cores located inside the Thomas-Fermi surface of the cloud move, to a good approximation, along with the background velocity field. On the other hand, cores in the low density region outside the surface of the cloud essentially do not feel the background velocity and move along the flow direction only because of the presence of transverse density gradients. After the vortex ring breaks up, the two lines move downstream and continue to deform, and eventually re-join to form a vortex ring (Fig. 2.12d)). The latter undergoes the same deformation described above, leading to another break up.

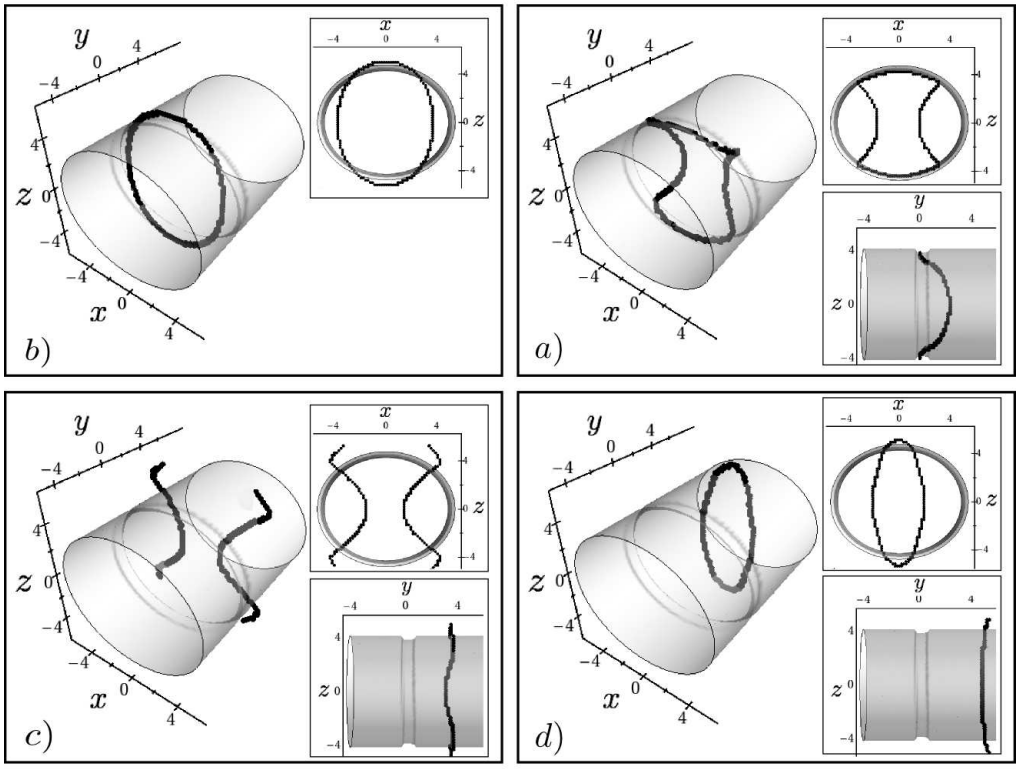

Fig. 2.12: Four subsequent stages of the vortex ring dynamics in the axially asymmetric waveguide. The gray surface indicates the position of the Thomas-Fermi surface of the condensate. Black dots show the position of the vortex cores. Insets show the front and side view. Here the waveguide is non-axially symmetric $\gamma = 1.2$, the initial flow velocity is $v = 1.05$, and the final barrier height is $V_s = 0.13\mu$. a) A partially-ghost ring vortex has formed. b) The ring vortex is strongly deformed. c) The ring vortex has broken up leaving two vortex lines. d) The vortex lines have joined back to form a new ring vortex.

We also verified that, even in a very slightly non-axially symmetric waveguide, ring vortices eventually break up. With $\gamma = 1.05$, the deformation is created more slowly with respect to the $\gamma = 1.2$ case, but the ring breaks up anyway, though at a later time.

2.5.7 Outlook

In these last two sections, we have seen that the excitations which show up above the critical velocity, when the superfluid is flowing through a weak link in two and three dimensions, are always vortices: inside the cloud there are cores of zero density around which the circulation is quantized. This cores are connected with each other to form lines ending at the boundaries of the system, or to form loops. The nature and dynamics of these vortex structures is very rich, and dependent on the system geometry.

The phase slip instability studied in these last two sections is a superfluid dissipation mechanism, since, as already discussed, it subtracts energy from the flow of the superfluid. However, GP equation does not include the dissipative processes which bring the system to thermal equilibrium. In a realistic situation, the vortices, carrying the energy subtracted from the superfluid, are supposed to eventually thermalize, with the result of heating the system. The role of finite temperature on the superfluid instability scenario presented here deserves further study.

Another point which deserves further investigation is the relation between the new instability criterion verified here, and other criteria of completely different origin. Among these, we found already the hydrodynamic local criterion (2.1) gives the correct critical velocity in effective one-dimension (see section 2.2), but not in two- and three- dimensional cases.

Bibliography, Part I

[1] A. Aftalion and I. Danaila. Giant vortices in combined harmonic and quartic traps. *Phys. Rev. A*, 69(3):033608, Mar 2004.

[2] A. Aftalion, Q. Du, and Y. Pomeau. Dissipative flow and vortex shedding in the painlevé boundary layer of a bose-einstein condensate. *Phys. Rev. Lett.*, 91(9):090407, Aug 2003.

[3] M. Albiez, R. Gati, J. Fölling, S. Hunsmann, M. Cristiani, and M. K. Oberthaler. Direct observation of tunneling and nonlinear self-trapping in a single bosonic josephson junction. *Phys. Rev. Lett.*, 95(1):010402, Jun 2005.

[4] D. Ananikian and T. Bergeman. Gross-pitaevskii equation for bose particles in a double-well potential: Two-mode models and beyond. *Phys. Rev. A*, 73(1):013604, Jan 2006.

[5] F. Ancilotto, L. Salasnich, and F. Toigo. dc josephson effect with fermi gases in the bose-einstein regime. *Phys. Rev. A*, 79(3):033627, Mar 2009.

[6] B. P. Anderson and M. A. Kasevich. Macroscopic Quantum Interference from Atomic Tunnel Arrays. *Science*, 282(5394):1686–1689, 1998.

[7] P. W. Anderson. Considerations on the flow of superfluid helium. *Rev. Mod. Phys.*, 38(2):298–310, Apr 1966.

[8] L. G. Aslamazov and A. I. Larkin. Josephson effect in superconducting point contacts. *JETP Lett.*, 9:87–91, 1969.

[9] S. Aubin, S. Myrskog, M. H. T. Extavour, L. J. LeBlanc, D. McKay, A. Stummer, and J. H. Thywissen. Rapid sympathetic cooling to fermi degeneracy on a chip. *Nature Physics*, 2:384–387, 2006.

[10] O. Avenel and E. Varoquaux. Josephson effect and quantum phase slippage in superfluids. *Phys. Rev. Lett.*, 60(5):416–419, Feb 1988.

[11] S. Backhaus, S. V. Pereverzev, A. Loshak, J. C. Davis, and R. E. Packard. Direct measurement of the current-phase relation of a superfluid 3he-b weak link. *Science*, 278(5342):1435–1438, 1997.

[12] A. Baratoff, J. A. Blackburn, and B. B. Schwartz. Current-phase relationship in short superconducting weak leans. *Phys. Rev. Lett.*, 25(16):1096–1099, Oct 1970.

[13] A. Barone and G. Paterno. *Physics and Applications of the Josephson Effect*. John Wiley and Sons, New York, 1982.

[14] F. Baumgärtner, R. J. Sewell, S. Eriksson, I. Llorente-Garcia, J. Dingjan, J. P. Cotter, and E. A. Hinds. Measuring energy differences by bec interferometry on a chip. *Phys. Rev. Lett.*, 105(24):243003, Dec 2010.

[15] N. G. Berloff and P. H. Roberts. Motions in a bose condensate: X. new results on the stability of axisymmetric solitary waves of the grosspitaevskii equation. *Journal of Physics A: Mathematical and General*, 37(47):11333, 2004.

[16] F. Bloch. Superfluidity in a ring. *Phys. Rev. A*, 7(6):2187–2191, Jun 1973.

[17] I. Carusotto, S. X. Hu, L. A. Collins, and A. Smerzi. Bogoliubov-Čerenkov radiation in a bose-einstein condensate flowing against an obstacle. *Phys. Rev. Lett.*, 97(26):260403, Dec 2006.

[18] F. S. Cataliotti, S. Burger, C. Fort, P. Maddaloni, F. Minardi, A. Trombettoni, A. Smerzi, and M. Inguscio. Josephson Junction Arrays with Bose-Einstein Condensates. *Science*, 293(5531):843–846, 2001.

[19] P. Cladé, C. Ryu, A. Ramanathan, K. Helmerson, and W. D. Phillips. Observation of a 2d bose gas: From thermal to quasicondensate to superfluid. *Phys. Rev. Lett.*, 102(17):170401, Apr 2009.

[20] L. Collins, J. Kress, and R. Walker. Excitation and ionization of molecules by a single-mode laser field using a time-dependent approach. *Computer Physics Communications*, 114(1-3):15 – 26, 1998.

[21] Y. Colombe, E. Knyazchyan, O. Morizot, B. Mercier, V. Lorent, and H. Perrin. Ultracold atoms confined in rf-induced two-dimensional trapping potentials. *Europhys. Lett.*, 67:593, 2004.

[22] M. Cozzini, B. Jackson, and S. Stringari. Vortex signatures in annular bose-einstein condensates. *Phys. Rev. A*, 73(1):013603, Jan 2006.

[23] F. Dalfovo, S. Giorgini, L. P. Pitaevskii, and S. Stringari. Theory of bose-einstein condensation in trapped gases. *Rev. Mod. Phys.*, 71(3):463–512, Apr 1999.

[24] P. Engels and C. Atherton. Stationary and nonstationary fluid flow of a bose-einstein condensate through a penetrable barrier. *Phys. Rev. Lett.*, 99(16):160405, Oct 2007.

[25] P. Engels, I. Coddington, P. C. Haljan, V. Schweikhard, and E. A. Cornell. Observation of long-lived vortex aggregates in rapidly rotating bose-einstein condensates. *Phys. Rev. Lett.*, 90(17):170405, May 2003.

[26] J. Estve, C. Gross, A. Weller, S. Giovanazzi, and M. K. Oberthaler. Squeezing and entanglement in a boseeinstein condensate. *Nature*, 455:1216–1219, 2008.

[27] D. L. Feder, M. S. Pindzola, L. A. Collins, B. I. Schneider, and C. W. Clark. Dark-soliton states of bose-einstein condensates in anisotropic traps. *Phys. Rev. A*, 62(5):053606, Oct 2000.

[28] C. J. Foster, P. B. Blakie, and M. J. Davis. Vortex pairing in two-dimensional bose gases. *Phys. Rev. A*, 81(2):023623, Feb 2010.

[29] T. Frisch, Y. Pomeau, and S. Rica. Transition to dissipation in a model of superflow. *Phys. Rev. Lett.*, 69(11):1644–1647, Sep 1992.

[30] C. Gross, T. Zibold, E. Nicklas, J. Estve, and M. K. Oberthaler. Nonlinear atom interferometer surpasses classical precision limit. *Nature*, 464:1165–1169, 2010.

[31] V. Hakim. Nonlinear schrödinger flow past an obstacle in one dimension. *Phys. Rev. E*, 55(3):2835–2845, Mar 1997.

[32] S. Hofferberth, B. Fischer, T. Schumm, J. Schmiedmayer, and I. Lesanovsky. Ultracold atoms in radio-frequency dressed potentials beyond the rotating-wave approximation. *Phys. Rev. A*, 76(1):013401, Jul 2007.

[33] E. Hoskinson, Y. Sato, I. Hahn, and R. E. Packard. Transition from phase slips to the josephson effect in a superfluid ^{4}he weak link. *Nature Physics*, 2:23–26, 2006.

[34] D. A. W. Hutchinson and E. Zaremba. Excitations of a bose-condensed gas in anisotropic traps. *Phys. Rev. A*, 57(2):1280–1285, Feb 1998.

[35] S. Inouye, S. Gupta, T. Rosenband, A. P. Chikkatur, A. Görlitz, T. L. Gustavson, A. E. Leanhardt, D. E. Pritchard, and W. Ketterle. Observation of vortex phase singularities in bose-einstein condensates. *Phys. Rev. Lett.*, 87(8):080402, Aug 2001.

[36] B. Jackson, J. F. McCann, and C. S. Adams. Vortex formation in dilute inhomogeneous bose-einstein condensates. *Phys. Rev. Lett.*, 80(18):3903–3906, May 1998.

[37] G.-B. Jo, J.-H. Choi, C. A. Christensen, Y.-R. Lee, T. A. Pasquini, W. Ketterle, and D. E. Pritchard. Matter-wave interferometry with phase fluctuating bose-einstein condensates. *Phys. Rev. Lett.*, 99(24):240406, Dec 2007.

[38] G.-B. Jo, J.-H. Choi, C. A. Christensen, T. A. Pasquini, Y.-R. Lee, W. Ketterle, and D. E. Pritchard. Phase-sensitive recombination of two bose-einstein condensates on an atom chip. *Phys. Rev. Lett.*, 98(18):180401, Apr 2007.

[39] G.-B. Jo, Y. Shin, S. Will, T. A. Pasquini, M. Saba, W. Ketterle, D. E. Pritchard, M. Vengalattore, and M. Prentiss. Long phase coherence time and number squeezing of two bose-einstein condensates on an atom chip. *Phys. Rev. Lett.*, 98(3):030407, Jan 2007.

[40] C. A. Jones, S. J. Putterman, and P. H. Roberts. Motions in a bose condensate. v. stability of solitary wave solutions of non-linear schrodinger equations in two and three dimensions. *Journal of Physics A: Mathematical and General*, 19(15):2991, 1986.

[41] C. A. Jones and P. H. Roberts. Motions in a bose condensate. iv. axisymmetric solitary waves. *Journal of Physics A: Mathematical and General*, 15(8):2599, 1982.

[42] B. D. Josephson. *Phys. Letters*, 1:251, 1962.

[43] B. D. Jr. and J. Pierce. Relaxation oscillator model for superconducting bridges. *Physics Letters A*, 38(2):81 – 82, 1972.

[44] W. Kohn. Cyclotron resonance and de haas-van alphen oscillations of an interacting electron gas. *Phys. Rev.*, 123(4):1242–1244, Aug 1961.

[45] V. V. Konotop and L. Pitaevskii. Landau dynamics of a grey soliton in a trapped condensate. *Phys. Rev. Lett.*, 93(24):240403, Dec 2004.

[46] L. D. Landau and E. M. Lifshitz. *Fluid Mechanics*. Pergamon Press, Oxford, 1987.

[47] J. S. Langer and V. Ambegaokar. Intrinsic resistive transition in narrow superconducting channels. *Phys. Rev.*, 164(2):498–510, Dec 1967.

[48] P. Leboeuf and N. Pavloff. Bose-einstein beams: Coherent propagation through a guide. *Phys. Rev. A*, 64(3):033602, Aug 2001.

[49] P. Leboeuf, N. Pavloff, and S. Sinha. Solitonic transmission of bose-einstein matter waves. *Phys. Rev. A*, 68(6):063608, Dec 2003.

[50] A. J. Leggett. Superfluidity. *Rev. Mod. Phys.*, 71(2):S318–S323, Mar 1999.

[51] A. J. Leggett. Bose-einstein condensation in the alkali gases: Some fundamental concepts. *Rev. Mod. Phys.*, 73(2):307–356, Apr 2001.

[52] A. J. Leggett and F. Sols. Comment on "phase and phase diffusion of a split bose-einstein condensate". *Phys. Rev. Lett.*, 81(6):1344, Aug 1998.

[53] I. Lesanovsky, T. Schumm, S. Hofferberth, L. M. Andersson, P. Krüger, and J. Schmiedmayer. Adiabatic radio-frequency potentials for the coherent manipulation of matter waves. *Phys. Rev. A*, 73(3):033619, Mar 2006.

[54] A. M. Leszczyszyn, G. A. El, Y. G. Gladush, and A. M. Kamchatnov. Transcritical flow of a bose-einstein condensate through a penetrable barrier. *Phys. Rev. A*, 79(6):063608, Jun 2009.

[55] S. Levy, E. Lahoud, I. Shomroni, and J. Steinhauer. The a.c. and d.c. josephson effects in a bose-einstein condensate. *Nature*, 449:579–583, 2007.

[56] W. Li. Stationary solutions of gross-pitaevskii equations in a double square well. *Phys. Rev. A*, 74(6):063612, Dec 2006.

[57] K. K. Likharev. Superconducting weak links. *Rev. Mod. Phys.*, 51(1):101–159, Jan 1979.

[58] K. K. Likharev. *Dynamics of Josephson Junction and Circuits*. Gordon and Breach, New York, 1986.

[59] W. A. Little. Decay of persistent currents in small superconductors. *Phys. Rev.*, 156(2):396–403, Apr 1967.

[60] M. Benakli, S. Raghavan, A. Smerzi, S. Fantoni, and S. R. Shenoy. Macroscopic angular-momentum states of bose-einstein condensates in toroidal traps. *Europhys. Lett.*, 46(3):275–281, 1999.

[61] Y. G. Mamaladze and O. D. Cheĭshvili. *Sov. Phys. JETP*, 23:112, 1966.

[62] J.-P. Martikainen, K.-A. Suominen, L. Santos, T. Schulte, and A. Sanpera. Generation and evolution of vortex-antivortex pairs in bose-einstein condensates. *Phys. Rev. A*, 64(6):063602, Nov 2001.

[63] P. Mason and N. G. Berloff. Dynamics of quantum vortices in a toroidal trap. *Phys. Rev. A*, 79(4):043620, Apr 2009.

[64] K. Maussang, G. E. Marti, T. Schneider, P. Treutlein, Y. Li, A. Sinatra, R. Long, J. Estève, and J. Reichel. Enhanced and reduced atom number fluctuations in a bec splitter. *Phys. Rev. Lett.*, 105(8):080403, Aug 2010.

[65] G. J. Milburn, J. Corney, E. M. Wright, and D. F. Walls. Quantum dynamics of an atomic bose-einstein condensate in a double-well potential. *Phys. Rev. A*, 55(6):4318–4324, Jun 1997.

[66] O. Morsch and M. Oberthaler. Dynamics of bose-einstein condensates in optical lattices. *Rev. Mod. Phys.*, 78(1):179–215, Feb 2006.

[67] H. M. Nilsen, G. Baym, and C. J. Pethick. Velocity of vortices in inhomogeneous Bose-Einstein condensates. *Proceedings of the National Academy of Sciences*, 103(21):7978–7981, 2006.

[68] R. Onofrio, C. Raman, J. M. Vogels, J. R. Abo-Shaeer, A. P. Chikkatur, and W. Ketterle. Observation of superfluid flow in a bose-einstein condensed gas. *Phys. Rev. Lett.*, 85(11):2228–2231, Sep 2000.

[69] H. Ott, J. Fortágh, S. Kraft, A. Günther, D. Komma, and C. Zimmermann. Nonlinear dynamics of a bose-einstein condensate in a magnetic waveguide. *Phys. Rev. Lett.*, 91(4):040402, Jul 2003.

[70] R. E. Packard. The role of the josephson-anderson equation in superfluid helium. *Rev. Mod. Phys.*, 70(2):641–651, Apr 1998.

[71] N. Pavloff. Breakdown of superfluidity of an atom laser past an obstacle. *Phys. Rev. A*, 66(1):013610, Jul 2002.

[72] C. J. Pethick and H. Smith. *Bose-Einstein Condensation in Dilute Gases*. University Press, Cambridge, 2002.

[73] C.-T. Pham, C. Nore, and M. tienne Brachet. Boundary layers and emitted excitations in nonlinear schrdinger superflow past a disk. *Physica D: Nonlinear Phenomena*, 210(3-4):203 – 226, 2005.

[74] E. P. Pitaevskii. *Nuovo Cimento*, 20:454, 1961.

[75] L. P. Pitaevskii. *Sov. Phys. JETP*, 13:451, 1961.

[76] L. P. Pitaevskii and S. Stringari. *Bose-Einstein Condensation*. University Press, Oxford, 2003.

[77] A. Polkovnikov and V. Gritsev. Breakdown of the adiabatic limit in low-dimensional gapless systems. *Nature Physics*, 4:477–481, 2008.

[78] S. Raghavan, A. Smerzi, S. Fantoni, and S. R. Shenoy. Coherent oscillations between two weakly coupled bose-einstein condensates: Josephson effects, π oscillations, and macroscopic quantum self-trapping. *Phys. Rev. A*, 59(1):620–633, Jan 1999.

[79] J. Reichel. Microchip traps and boseeinstein condensation. *Applied Physics B: Lasers and Optics*, 74:469–487, 2002. 10.1007/s003400200861.

[80] C. Ryu, M. F. Andersen, P. Cladé, V. Natarajan, K. Helmerson, and W. D. Phillips. Observation of persistent flow of a bose-einstein condensate in a toroidal trap. *Phys. Rev. Lett.*, 99(26):260401, Dec 2007.

[81] B. I. Schneider, L. A. Collins, and S. X. Hu. Parallel solver for the time-dependent linear and nonlinear schrödinger equation. *Phys. Rev. E*, 73(3):036708, Mar 2006.

[82] T. Schumm, S. Hofferberth, L. M. Andersson, S. Wildermuth, S. Groth, I. Bar-Joseph, J. Schmiedmayer, and P. Krger. Matter-wave interferometry in a double well on an atom chip. *Nature Physics*, 1:57–62, 2005.

[83] B. T. Seaman, L. D. Carr, and M. J. Holland. Effect of a potential step or impurity on the bose-einstein condensate mean field. *Phys. Rev. A*, 71(3):033609, Mar 2005.

[84] Y. Shin, G.-B. Jo, M. Saba, T. A. Pasquini, W. Ketterle, and D. E. Pritchard. Optical weak link between two spatially separated bose-einstein condensates. *Phys. Rev. Lett.*, 95(17):170402, Oct 2005.

[85] I. Shomroni, E. Lahoud, S. Levy, and J. Steinhauer. Evidence for an oscillating soliton/vortex ring by density engineering of a boseeinstein condensate. *Nature Physics*, 5:193–197, 2009.

[86] R. W. Simmonds. *Josephson Weak Links and Quantum Interference in Superfluid ^3He.* PhD thesis, Graduate Division of the University of California at Berkeley, 2002.

[87] T. P. Simula, N. Nygaard, S. X. Hu, L. A. Collins, B. I. Schneider, and K. Mølmer. Angular momentum exchange between coherent light and matter fields. *Phys. Rev. A*, 77(1):015401, Jan 2008.

[88] A. Smerzi and S. Fantoni. Large amplitude oscillations of a bose condensate. *Phys. Rev. Lett.*, 78(19):3589–3593, May 1997.

[89] A. Smerzi, S. Fantoni, S. Giovanazzi, and S. R. Shenoy. Quantum coherent atomic tunneling between two trapped bose-einstein condensates. *Phys. Rev. Lett.*, 79(25):4950–4953, Dec 1997.

[90] A. Smerzi and A. Trombettoni. Nonlinear tight-binding approximation for bose-einstein condensates in a lattice. *Phys. Rev. A*, 68(2):023613, Aug 2003.

[91] F. Sols and J. Ferrer. Crossover from the josephson effect to bulk superconducting flow. *Phys. Rev. B*, 49(22):15913–15919, Jun 1994.

[92] A. Spuntarelli, P. Pieri, and G. C. Strinati. Josephson effect throughout the bcs-bec crossover. *Phys. Rev. Lett.*, 99(4):040401, Jul 2007.

[93] M. Stone and A. M. Srivastava. Boundary layer separation and vortex creation in superflow through small orifices. *Journal of Low Temperature Physics*, 102:445–459, 1996. 10.1007/BF00755123.

[94] S. Stringari. Collective excitations of a trapped bose-condensed gas. *Phys. Rev. Lett.*, 77(12):2360–2363, Sep 1996.

[95] J. Tempere, J. T. Devreese, and E. R. I. Abraham. Vortices in bose-einstein condensates confined in a multiply connected laguerre-gaussian optical trap. *Phys. Rev. A*, 64(2):023603, Jul 2001.

[96] M. Tsubota, K. Kasamatsu, and M. Ueda. Vortex lattice formation in a rotating bose-einstein condensate. *Phys. Rev. A*, 65(2):023603, Jan 2002.

[97] E. Varoquaux, O. Avenel, and M. Meisel. *Can. J. Phys.*, 65:1377, 1987.

[98] W. F. Vinen and J. J. Niemela. Quantum turbulence. *Journal of Low Temperature Physics*, 128:167–231, 2002. 10.1023/A:1019695418590.

[99] Y.-J. Wang, D. Z. Anderson, V. M. Bright, E. A. Cornell, Q. Diot, T. Kishimoto, M. Prentiss, R. A. Saravanan, S. R. Segal, and S. Wu. Atom michelson interferometer on a chip using a bose-einstein condensate. *Phys. Rev. Lett.*, 94(9):090405, Mar 2005.

[100] T. Winiecki, B. Jackson, J. F. McCann, and C. S. Adams. Vortex shedding and drag in dilute bose-einstein condensates. *Journal of Physics B: Atomic, Molecular and Optical Physics*, 33(19):4069, 2000.

[101] C. N. Yang. Concept of off-diagonal long-range order and the quantum phases of liquid he and of superconductors. *Rev. Mod. Phys.*, 34(4):694–704, Oct 1962.

[102] I. Zapata, F. Sols, and A. J. Leggett. Josephson effect between trapped bose-einstein condensates. *Phys. Rev. A*, 57(1):R28–R31, Jan 1998.

[103] E. Zaremba. Sound propagation in a cylindrical bose-condensed gas. *Phys. Rev. A*, 57(1):518–521, Jan 1998.

Part II

Quantum Interferometry with Bose-Einstein Condensates

Classical and quantum interferometry

The aim of an interferometric device is to measure a phase shift between two fields travelling down separated paths. The phase shift is induced, broadly speaking, by an external perturbation which is the physical quantity to be eventually determined.

Clearly, developments in such a field would aim to reach the best possible precision with given apparatus and resources. Therefore, the uncertainty with which the phase shift can be determined becomes a crucial issue in interferometry. This is tightly connected to information theory and single parameter estimation, as we shall discuss later with some detail.

Estimation theory answers a fundamental question: how the uncertainty of a given device scales with the resources employed in the measurement. In optical or atomic interferometry these resources essentially correspond to the number of particles entering the apparatus. A generic linear interferometer with classical input states, that is, with no quantum correlations between the particles, has a sensitivity $\Delta\theta$ which scales as $1/\sqrt{N}$. This is referred to as shot-noise limit or standard quantum limit (SQL).

The inverse scaling of the sensitivity with the number of particles in input seems to suggest that the interferometer performance could be simply improved at will by increasing the number of resources N. However, it is essential to notice that this number cannot be increased ad infinitum. In optical interferometry, the back-reaction of the mirrors under an increasing light pressure limits the sensitivity [58]. Similar problems occur in atom interferometers, where mirrors and beam splitters are implemented by standing light waves [15]. In addition, there are interaction induced shifts at higher densities.

Hence, there is an optimal number of particles N that can be used in a particular setup. Fixing this number, the sensitivity can still be improved by a factor $1/\sqrt{N}$ in $\Delta\theta$ by using "usefully" correlated states, which can provide a huge gain. In particular, entangled input states can allow for a $1/N$ scaling, referred to as the Heisenberg limit (HL), which is the ultimate limit for quantum interferometers.

Progress in this direction is not only important for interferometry itself, but the results apply

to a wide range of quantum technological applications such as quantum frequency standards, lithography, positioning, and imaging [34].

It is generally believed that entanglement plays a crucial role in new quantum technologies such as quantum communication, quantum simulation, and quantum computation [65]. Moreover, as introduced above, entanglement is also a key resource to beat the SQL. There seem in general to be a relation between phase estimation and entanglement theory [46].

On the experimental side, quantum interferometry has witnessed a substantial advance in the last years. Several proof-of-principle experiments reaching a sub-shot-noise sensitivity have been performed, for a fixed number of particles, with photons [62, 86, 64, 32] and ions [56], while squeezed (entangled) states for interferometry with a nonfixed number of particles have been prepared with BECs [67, 51, 27, 38, 75], atoms at room temperature [30], and light [36, 85].

Current research on linear interferometers is directed toward the determination of optimal input states and output measurements [19, 93, 45, 26, 81, 16, 11, 72, 73, 84, 14], adaptive phase measurement schemes [7, 43, 6, 47], and the study of the influence of particle losses [25, 24, 78]. Also, schemes for nonlinear interferometers are under investigation [59, 79, 10, 9].

In what follows, we will deal with implementations of quantum interferometers with dilute BECs, trapped by optical/magnetic fields. In particular, we will study double-well traps, already introduced in section 1.7, and analyze the potential of two different interferometers realizable with current experimental technology. First, we will study a double-well Rabi interferometer, where the phase accumulation stage takes place while the atoms oscillate between the wells, and the population imbalance is measured at different times. We will discuss the application of this scheme to the measurement of short-range forces. As a second interferometric protocol, we will analyze a two-slit interference scheme, where, after the phase is imprinted, the atoms are released from the trap and freely expand to form an interference pattern, on which position measurements are subsequently performed. Both proposal have the common feature of being simpler to implement than the Mach-Zehnder interferometer, a paradigm of linear interferometers.

Chapter 3

Interferometry with trapped Bose-Einstein condensates

3.1 Sensitivity of an interferometer and estimation theory

In this section, we will introduce some basic concepts and formalism of estimation theory, useful for the application to quantum interferometry with BECs, especially dealing with two-level systems. The organization of the section is modelled on the introduction of the work [48].

3.1.1 Linear interferometers and collective operators

In this chapter, we will be dealing only with linear interferometers, where the phase shift is due to some external effect which independently acts on each particle. A paradigmatic example of such an interferometer is the Mach-Zehnder interferometer (MZI), see Fig. 3.1 a), where the two input signals are recombined through a beam-splitter, then the phase shift takes place when the two arms are completely decoupled, and finally a last beam splitter acts before the intensity is measured at the two output ports.

Here and in what follows, we will also restrict ourselves to interferometric implementations with two-level systems. The two levels could be two momentum states, as for the Mach-Zehnder interferometer,the two internal states of the particles, or the states localized in either of the two wells of a double-well trap, see Fig. 3.1. The double-well implementation will be the object of the next sections.

The transformation corresponding to a generic two-mode linear interferometer can be de-

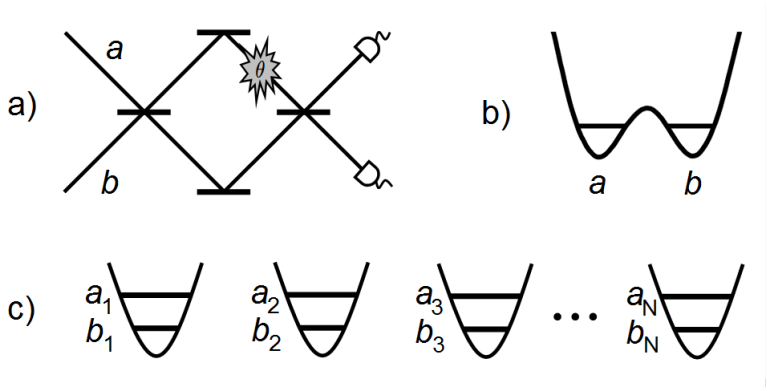

Fig. 3.1: This figure is taken from [48]. Systems that can be used for linear two-state interferometry: a) archetypical optical Mach-Zehnder interferometer as in Refs [64, 60], b) double-well system as implemented in recent experiments on squeezing in BECs [27, 38, 75], and c) system of single wells as in ion traps [56, 49]. In the first two cases each of the N particles lives in the subspace of the two states labelled by a and b, corresponding to momentum states in case a) and to the left and the right well in case b). In case c), there is one particle per well, and particle k in trap k has the two internal degrees of freedom a_k and b_k (displayed are trap states, while in ion traps typically internal states of the ions are used [49]). The interferometer operations acts on the a-b subspace in the cases a) and b) and identically on the subspaces a_k-b_k in case c). In the latter case, the particles are accessible individually via the different traps in principle. They can be treated as distinguishable particles labelled by the trap number k if the spacial wavefunctions of the particles in the different traps do not overlap [70].

scribed in terms of collective spin operators

$$\hat{J}_i = \frac{1}{2}\sum_{k=1}^{N} \hat{\sigma}_i^{(k)}, \tag{3.1}$$

where $\hat{\sigma}_i^{(k)}$ is the i-th Pauli matrix acting on particle k, where $i = x, y, z$. The input state is transformed by $\exp(-i\hat{J}_{\vec{n}}\theta)$, where $\hat{J}_{\vec{n}} = \vec{n} \cdot \hat{\vec{J}}$, and θ is the phase shift. For a Mach-Zehnder interferometer consisting of a beam splitter $\exp(i\hat{J}_x\frac{\pi}{2})$, a phase shift $\exp(-i\hat{J}_z\theta)$, and another beam splitter $\exp(-i\hat{J}_x\frac{\pi}{2})$, the effective rotation is [93]

$$\hat{U}_{\mathrm{MZ}} = e^{-i\hat{J}_x\frac{\pi}{2}} e^{-i\hat{J}_z\theta} e^{i\hat{J}_x\frac{\pi}{2}} = e^{-i\hat{J}_y\theta}, \tag{3.2}$$

hence $\vec{n} = y$. This transformation also describes other applications such as the Fabry-Perot interferometer,Ramsey spectroscopy, and the Michelson-Morley interferometer.

It is important to notice that, since the collective spin operators are just sums of single-particle operators, the linear interferometer transformation factorizes,

$$e^{-i\hat{J}_{\vec{n}}\theta} = e^{-i\hat{\sigma}_{\vec{n}}^{(1)}\frac{\theta}{2}} \otimes e^{-i\hat{\sigma}_{\vec{n}}^{(2)}\frac{\theta}{2}} \otimes \cdots \otimes e^{-i\hat{\sigma}_{\vec{n}}^{(N)}\frac{\theta}{2}}, \tag{3.3}$$

where $\hat{\sigma}_{\vec{n}} = \hat{\vec{\sigma}} \cdot \vec{n}$. Therefore, this operation acts only locally on the particles, and no correlation (entanglement) can be created in a linear interferometer.

3.1.2 Phase estimation sensitivity

A generic phase estimation scheme [41, 44] can be divided into four subsequent stages:

- i) the preparation of the initial state ρ_{in},
- ii) the phase transformation corresponding to the particular interferometer (i.e. the operator $\hat{J}_{\vec{n}}$), changing ρ_{in} into $\rho(\theta)$ parametrized by θ only,
- iii) the measurement performed on $\rho(\theta)$,
- iv) the processing of the measurement results, implying the choice of an estimator, that is, a way to use the measurement results in order to infer the value of the phase θ.

A general measurement, which not necessarily has a corresponding operator defining an observable, can be characterized by its positive operator valued measure (POVM) elements $\{\hat{E}(\xi)\}_\xi$ [65]. Given one of the possible outcomes ξ[1] generated in stage iii) of the phase estimation sequence above, θ can be inferred from ξ upon choosing an estimator $\theta_{\text{est}}(\xi)$ in stage iv).

The estimator $\theta_{\text{est}}(\xi)$ can in principle be any function of the measurement outcome, though one usually looks for the so-called unbiased estimators, such that their mean tends to the true value of the phase shift: $\lim_{m\to\infty} \bar{\theta}_{\text{est}}^{(m)} = \theta$, where $\bar{\theta}_{\text{est}}^{(m)}$ is the mean over m experiments.

The phase sensitivity, $\Delta\theta$ is defined as the standard deviation of the estimator, $\Delta\theta_{\text{est}}$. If the estimator is unbiased, the Cramér-Rao theorem [41, 44] sets a lower bound for the sensitivity:

$$\Delta\theta_{\text{est}} \geq \frac{1}{\sqrt{m}} \frac{1}{\sqrt{F}}, \tag{3.4}$$

where m is the number of independent repetitions of the measurement, and F is the so-called Fisher information (FI). The Fisher information [92, 12, 13] quantifies the statistical distinguishability, achievable through a given measurement defined by $\{\hat{E}(\xi)\}$, of quantum states lying along

[1] in general we can think as a set of numbers resulting from a given measurement

a path described by a single parameter θ (i.e. all states are transformed into each other by a single parameter transformation). One can thus see why the FI is related to a measurement sensitivity. Indeed, the best possible precision is set by the smallest difference between two different values of the parameter θ which can still be distinguished by the measurement, which in turn means, since the measurement is performed on a quantum state evolved by the single parameter transformation, the two closest quantum states which can be distinguished. The FI is defined as

$$F[\rho(\theta);\{\hat{E}(\xi)\}] = \int d\xi P(\xi|\theta)\left[\frac{\partial \log P(\xi|\theta)}{\partial\theta}\right]^2 = \int d\xi \frac{1}{P(\xi|\theta)}\left[\frac{\partial P(\xi|\theta)}{\partial\theta}\right]^2, \tag{3.5}$$

where the conditional probabilities are given by the quantum mechanical expectation values, $P(\xi|\theta) = \mathrm{Tr}[\hat{E}(\xi)\rho(\theta)]$.

Another important quantity is the quantum Fisher information (QFI), F_Q, obtained from the FI by maximizing over all possible measurements,

$$F_Q[\rho(\theta)] = \max_{\{\hat{E}(\xi)\}} F\big[\rho(\theta);\{\hat{E}(\xi)\}\big]. \tag{3.6}$$

Therefore, while the FI depends on the transformation (i.e. the interferometric apparatus), the input state, and the measurement, the QFI depends, given an interferometer, only on the input state. For pure input states, and for a unitary phase transformation with the generator $\hat{H}$, where $\hat{H} = \hat{J}_{\vec{n}}$ for linear two-mode interferometers which we are interested in, the QFI is [12, 13]

$$F_Q[|\psi\rangle;\hat{H}] = 4\langle\Delta\hat{H}^2\rangle_\psi = 4(\langle\hat{H}^2\rangle_\psi - \langle\hat{H}\rangle_\psi^2). \tag{3.7}$$

On the other hand, for mixed input states, the QFI is given by [12, 13]

$$F_Q[\rho;\hat{H}] = 2\sum_{j,k}(\lambda_j+\lambda_k)\Big(\frac{\lambda_j-\lambda_k}{\lambda_j+\lambda_k}\Big)^2|\langle j|\hat{H}|k\rangle|^2, \tag{3.8}$$

where $\rho = \sum_k \lambda_k|k\rangle\langle k|$ is the spectral decomposition of the input state, and the sum is over terms where $\lambda_j + \lambda_k \neq 0$ only.

For practical purposes, a fundamental result is given by Fisher's theorem, which ensures that the bound (3.4), often called Cramér-Rao lower bound (CRLB), can be saturated in the central limit, typically for large number of measurement m, using a maximum-likelihood (ML) estimator [21]. Since we will make use of ML estimators in our study of interferometric implementations with trapped BECs, applications of ML estimation to specific cases will be discussed in detail in the following sections. We limit ourselves to mention that the ML estimator $\theta_{\mathrm{ML}}(\xi)$ is obtained by maximizing, given the measurement outcomes ξ, the conditional probability $P(\xi|\theta)$.

3.1.3 Entanglement and interferometer sensitivity

In this final part of the section, we will briefly introduce some results regarding the connection between the interferometer sensitivity and the amount of entanglement present in the input state.

The usual definition of entanglement comes through stating which states are not entangled, that is, fully separable. A pure state of N particles is called fully separable if can be written as a product state, $|\psi_{\rm fs}\rangle = \otimes_{i=1}^{N}|\psi^{(i)}\rangle$, where $|\psi^{(i)}\rangle$ is a pure state of particle i. A mixed state is fully separable if it can be written as an incoherent mixture of such product states,

$$\rho_{\rm fs} = \sum_k p_k |\psi_k^{(1)}\rangle\langle\psi_k^{(1)}| \otimes |\psi_k^{(2)}\rangle\langle\psi_k^{(2)}| \otimes \cdots \otimes |\psi_k^{(N)}\rangle\langle\psi_k^{(N)}|, \tag{3.9}$$

where $\{p_k\}$ is a probability distribution [88]. Any such state can be generated by local operations and classical communication [88, 65]. Non-separable states are entangled, and non-local operations are needed for their production.

A connection between entanglement and sensitivity for two-mode interferometers has been recently established [74]. It has been shown that, for all fully separable input states, and for any unitary generator of a linear two-mode interferometer, $\hat{H} = \hat{J}_{\vec{n}}$, the FI is bounded by the number of particles, $F[\rho_{\rm fs}; \hat{J}_{\vec{n}}] \leq N$. Therefore, by the CRLB (3.4), the phase sensitivity is bounded by the shot-noise limit,

$$\Delta\theta_{\rm est} \geq \frac{1}{\sqrt{N_{\rm tot}}}, \tag{3.10}$$

where $N_{\rm tot} = mN$ is the total number of particles used in the m runs. This means that only entangled input states can reach a sub shot-noise sensitivity.

On the other hand, the Heisenberg limit, already introduced in the previous section, sets as the ultimate limit on the phase sensitivity allowed by quantum mechanics. It is important to point out that all these bounds must be carefully defined in relation to the resources used. If the number of measurements, m and the number of particles used in each measurement, N are fixed separately, then the HL is given by [35]

$$\Delta\theta = \frac{1}{\sqrt{m}N}. \tag{3.11}$$

3.2 Why interferometry with dilute BECs ?

Interferometers operating with atoms are particularly useful and versatile tools for measuring phase shifts originating from a large variety of interactions with external sources [22]. In many cases, the interaction is largely enhanced for atoms as compared to photons, enabling phase

estimation with an increased precision. This happens, for instance, for the rotational Sagnac phase, given by $4\pi\Omega A\frac{m}{\hbar}$, (where m is the mass of the atoms and equals $\hbar/\lambda c$ for photons; λ is the wavelenght of the radiation, A is the area of the interferometer, and Ω is the angular velocity of the setup). For the same A and Ω, and typical values of the atomic mass and λ, the Sagnac phase is enlarged by a factor 10^{10} in an atom interferometer as compared to an optical interferometer. However, the phase is also dependent on the area of the interferometer, which is typically considerably smaller in an atom interferometer.

Interferometry with BECs might offer additional advantages with respect to atom interferometry. The reduced spreading in the momentum distribution is advantagous for the operation of interferometers with standing light waves functioning as beam splitters. The low velocities also enable the realization of interferometers enclosing a larger area. Moreover, the inter-particle interactions, toghether with the macroscopic phase coherence, allow to create entangled states which, as mentioned above, can be used to perform quantum interferometry at the HL.

This makes the dilute BEC a promising system to measure the electromagnetic [66, 68, 57, 5] or gravitational [28, 1] forces. Moreover, the inter-atomic interactions have been already used to create entangled states [27, 38, 75, 61].

Another very promising experimental tool which can be used with atomic BECs is the possibility to tune the strength of the atom-atom interaction and dynamically adjust it near so-called Feshbach resonances [53, 20]. In particular, atom-atom interactions can be tuned to zero to allow for the realization of non-interacting BECs [87, 77] . This feature has been exploited to realize an interferometer with BEC trapped inside an optical lattice [28, 39]. Here Bloch oscillations were forced by gravity and imaged at different times after releasing the trap. Due to the micrometric size of the atomic sample (related to the BEC small spreading in momentum distribution) and the enhanced coherence times (allowed by the tuning of the inter-particle interactions almost to zero) this sensor seems an ideal tool for measuring forces with high sensitivity.

3.3 Implementation in double-well traps I: Rabi interferometer and application to the measurement of short range forces

This section is based on the work: **Rabi Interferometry and Sensitive Measurement of the Casimir-Polder Force with Ultra-Cold Gases**, J. Chwedeńczuk

[*INO-CNR, BEC Center, and Dipartimento di Fisica, Via Sommarive 14, 38123 Povo, Trento, Italy*] L. Pezzé [*Laboratoire Charles Fabry, Institut d'Optique, 2 Avenue Fresnel, 91127 Palaiseau - France*], F.P., and A. Smerzi [*INO-CNR, BEC Center, and Dipartimento di Fisica, Via Sommarive 14, 38123 Povo, Trento, Italy*], published in Phys. Rev. A **82**, 032104 (2010).

As anticipated, a BEC interferometer can be implemented using ultracold atoms inside a double-well trap [71, 55, 47, 37] (see section 1.7 for an example of experimental realization of a BEC double-well). The two interferometer modes correspond to states localized about the two minima of the external potential, as illustrated in Fig. 3.1 b).

In the two-mode approximation, the Hamiltonian of the system can be written as a function of the collective angular momentum operators,

$$\hat{H} = -E_J \hat{J}_x + \frac{E_C}{N} \hat{J}_z^2 + \delta \hat{J}_z, \tag{3.12}$$

where E_J is the kinetic energy related to the hopping of particles between the wells, E_C is the atom-atom interaction energy within each well, and δ is the potential energy difference between the two localized single particle states.

In subsection 1.7.5, we have analyzed the two-mode approximation to the GP mean-field equation for a BEC in a double-well. A quantization of the latter mean-field two-mode model will yeld a Hamiltonian of the same kind of Eq. (3.12). The overlap integrals $\mathcal{K}$ and $(1/2)g \int d^3r \Phi_{\mathrm{L,R}}^4$, defined in 1.7.5, would substitute E_J and E_C/N, respectively[2].

Looking at Eq. (3.12), we see that the phase shift transformation $\exp(-i\hat{J}_z\theta)$ can be performed by letting the system evolve in presence of an energy difference between the two potential minima, $\delta \neq 0$, but making both the coupling between the two wells and the atom-atom interaction negligible. The beam splitter transformation $\exp(-i\hat{J}_x\pi/2)$ can also be implemented by letting the atoms oscillate between the wells with no energy difference between the minima, $\delta = 0$, and with negligible atom-atom interactions, over a time interval t such that $tE_J/\hbar = \pi/2$.

An important achievement would be the realization of the double-well Mach-Zehnder interferometer, which, as discussed in the previous section, constitutes the paradigm of linear interferometrs. Since it requires two beam splitters, plus an intermediate phase shift, the experimental realization of a double-well MZI demands an exquisite control over the dynamical manipulation of the inter-well barrier, accompanied by the proper time-dependent tuning of the interactions between the atoms by Feschbach resonances.

[2] the overlap integral χ must also be neglected in order to get Eq. (3.12)

On the other hand, it is interesting and experimentally relevant to search for alternative interferometric schemes which can be easier to realize, and therefore potentially more stable than the MZI. This is the main motivation for the works described here and in the next section, where we propose two simpler interferometers to be implemented with dilute BECs inside double-well traps.

3.3.1 Overview of the main results

We propose a new interferometric protocol: a double-well Rabi interferometer (RI). This can be implemented using either degenerate spin-polarized Fermions or non-interacting Bose-Einstein condensates (BECs). The Rabi interferometer is less sensitive than the MZI, but does not require any splitting/recombination processes, and is potentially suitable for the estimation of forces rapidly decaying with distance. Moreover, in analogy to the MZI, but differently from previous proposals for the measurement of weak forces, the RI can reach a sub shot-noise phase sensitivity using spin squeezed states recently created with a BEC [27]. In the scheme presented here, atoms oscillate between the two wells while acquiring a phase shift. The relative number of particles among the two wells undergoes Rabi oscillations analogous to those experienced by a collection of two-level atoms in a quasi-resonant field [89]. The measurement of population imbalance as a function of time permits to infer the value of the external force as it affects both the amplitude and the frequency of Rabi oscillations. In particular, once fed with a fermionic/bosonic spin coherent state, the interferometer allows for an accurate measurement of the Casimir-Polder force between the atomic sample and a surface. We show that, even in the presence of typical experimental noise, it is possible to distinguish between thermal and zero-temperature regimes of the Casimir-Polder potential [2], which has not yet been achieved in experiment [68, 57, 66, 82].

3.3.2 The model

We consider a degenerate gas of N non-interacting atoms confined in a double-well potential, with the splitting direction along x_1, and a harmonic transverse confinement along $\vec{x}_\perp = (x_2, x_3)$. Let us define the operators $\hat{a}_{\mathrm{r/l},\vec{n}_\perp}$, together with the corresponding wave-functions $\psi_{\mathrm{r/l}}(x_1, x_2, x_3)$, which annihilate a particle in the right/left well occupying a harmonic trap state labeled by indices $\vec{n}_\perp = (n_2, n_3)$. Under proper choice of commutation relations, the Hamiltonian either for ultracold bosons or ultracold fermions, reads

$$\hat{H} = -E_J \hat{J}_x + \delta \hat{J}_z. \tag{3.13}$$

This is exactly the two-mode hamiltonian of Eq. (3.12), where the interaction between the atoms has been neglected.

Notice that, while ultracold bosons populate only the $\vec{n}_\perp = 0$ transverse state, fermions distribute over N lowest states of the trap. Therefore, in order to get Eq. (3.13) with fermionic atoms, we need to further assume that the level spacing of the harmonic trap in x_2 and x_3 directions is much smaller than the gap between the two lowest and higher excited states of the double-well potential in direction x_1, so that the higher modes of the double-well are not populated. In the second quantization notation we use here, the collective angular momenta (3.1) can be written as functions of the operators $\hat{a}_{\mathrm{r/l},\vec{n}_\perp}$ and $\hat{a}^\dagger_{\mathrm{r/l},\vec{n}_\perp}$. They read,

$$\begin{aligned}
\hat{J}_x &\equiv \frac{1}{2}\sum_{\vec{n}_\perp}\left(\hat{a}^\dagger_{r,\vec{n}_\perp}\hat{a}_{l,\vec{n}_\perp} + \hat{a}^\dagger_{l,\vec{n}_\perp}\hat{a}_{r,\vec{n}_\perp}\right), \\
\hat{J}_y &\equiv \frac{1}{2i}\sum_{\vec{n}_\perp}\left(\hat{a}^\dagger_{r,\vec{n}_\perp}\hat{a}_{l,\vec{n}_\perp} - \hat{a}^\dagger_{l,\vec{n}_\perp}\hat{a}_{r,\vec{n}_\perp}\right), \\
\hat{J}_z &\equiv \frac{1}{2}\sum_{\vec{n}_\perp}\left(\hat{a}^\dagger_{r,\vec{n}_\perp}\hat{a}_{r,\vec{n}_\perp} - \hat{a}^\dagger_{l,\vec{n}_\perp}\hat{a}_{l,\vec{n}_\perp}\right),
\end{aligned} \tag{3.14}$$

where for fermions the sum runs over lowest N states of the harmonic trap, while for bosons only $\vec{n}_\perp = 0$ contributes.

We separate the external potential into a double-well part, $V_{\mathrm{dw}}(x_1, x_2, x_3)$, which is symmetric with respect to zero along the splitting direction x_1, plus an asymmetric part $V(x_1)$, due to the external force we want to measure. The latter induces a difference in potential energy,

$$\delta = \int dx_1 dx_2 dx_3 \, \left(|\psi_r|^2 - |\psi_l|^2\right) V(x_1) \, . \tag{3.15}$$

3.3.3 Estimation of the energy difference from detuned Rabi oscillations

The goal of the Rabi interferometer is therefore to estimate the unknown value of the energy difference δ. We choose to measure the population imbalance between the two wells, which corresponds to eigenvalues of the operator [3] $\hat{J}_z$. We can usefully rewrite the evolution operator generated by (3.13) as

$$\hat{U}(t) = e^{-it\hat{H}/\hbar} = e^{-i\alpha\hat{J}_y} e^{i\omega t\hat{J}_x} e^{i\alpha\hat{J}_y}, \tag{3.16}$$

where $\cos\alpha = E_J/\hbar\omega$, $\sin\alpha = \delta/\hbar\omega$ and $\omega = \sqrt{E_J^2 + \delta^2}/\hbar$ is the detuned Rabi frequency. The energy difference δ plays indeed the role of a detuning. Instead of evolving the input state and

[3] instead of the general POVM considered in subsection 3.1.2, here we have a measurement connected with an ordinary observable

subsequently measure J_z, we can use the Heisenberg picture to evolve the measurement operator J_z:

$$\hat{J}_z(t,\delta) = \sin\alpha\cos\alpha(\cos\omega t - 1)\hat{J}_x - \cos\alpha\sin\omega t\ \hat{J}_y + (\cos^2\alpha\ \cos\omega t + \sin^2\alpha)\hat{J}_z \tag{3.17}$$

In the following, we will analyze a simple estimator: a least square fit to the time oscillation of the population imbalance. We will see that this actually corresponds to a ML estimator, and therefore, as seen in subsection 3.1.2, allows us to calculate the sensitivity by the CRLB (3.4).

The estimation protocol consists of collecting k values of the population imbalance, $\{n\} = \{n(t_1), \ldots, n(t_k)\}$, each $n(t_i)$ coming from an average over m independent measurements, $n(t_i) = \frac{1}{m}\sum_{j=1}^{m} n_j(t_i)$, where $n_j(t_i)$ is a result of a single run. The value of δ is then estimated from a least squares fit in time of the function $n_{\text{fit}}(t,\delta)$ to the k-tuple $\{n\} = \{n(t_1), \ldots, n(t_k)\}$. The function $n_{\text{fit}}(t,\delta)$ must be known before the phase estimation is performed. It must be constructed by repeating the above described experimental sequence a sufficient number of times, but using different known values of δ. This stage, preceding phase estimation, is called calibration. For a sufficiently large number of iterations, and in absence of thermal or technical noise, the measured function $n_{\text{fit}}(t,\delta)$ will tend to the quantum mechanical average, $\langle\hat{J}_z(t,\delta)\rangle$, where the expectation value is calculated with the input state of the interferometer, since we are adopting the Heisenberg picture.

If the number of measurements $m \gg 1$, we can use the central limit theorem to write the conditional probability for measuring a value $n(t_i)$ as the Gaussian,

$$p(n(t_i)|\delta) = \frac{1}{\sqrt{2\pi}\Delta\hat{J}_z(t_i,\delta)/\sqrt{m}}\ \exp\left[-\frac{(n(t_i) - \langle\hat{J}_z(t_i,\delta)\rangle)^2}{2\ \Delta^2\hat{J}_z(t_i,\delta)/m}\right], \tag{3.18}$$

where $\Delta^2\hat{J}_z(t_i,\delta) = \langle\hat{J}_z(t_i,\delta)^2\rangle - \langle\hat{J}_z(t_i,\delta)\rangle^2$. As well as the fitting function n_{fit}, we assume that the variance $\Delta^2\hat{J}_z(t_i,\delta)$ will coincide, after a sufficient number of measurements, with the corresponding quantum mechanical average.

Since measurements at different times are independent, the joint conditional probability of detecting the k-tuple $\{n\}$ is simply the product, $p(\{n\}|\delta) = \prod_{i=1}^{k} p(n(t_i)|\delta)$. The condition for the least squares estimator,

$$\frac{\partial}{\partial\delta}\left[\sum_{i=1}^{k}\frac{\left(n(t_i) - \langle\hat{J}_z(t_i,\delta)\rangle\right)^2}{2\ \Delta^2\hat{J}_z(t_i,\delta)}\right] = 0 \tag{3.19}$$

maximizes the probability $p(\{n\}|\delta)$ with respect to δ, i.e. $\frac{\partial}{\partial\delta}\ p(\{n\}|\delta) = 0$. Therefore, the least square fit corresponds to the ML estimator for the measurement described by the probability

$p(\{n\}|\delta)$, and its sensitivity saturates the CRLB:

$$\Delta^2\delta = \left[\int d\{n\}\frac{\left[\frac{\partial}{\partial\delta}p(\{n\}|\delta)\right]^2}{p(\{n\}|\delta)}\right]^{-1} = \frac{1}{\sum_{i=1}^{k}\frac{1}{\Delta^2\delta(t_i)}}, \tag{3.20}$$

where

$$\Delta^2\delta(t_i) = \frac{\Delta^2\hat{J}_z(t_i,\delta)}{m\left[\frac{\partial}{\partial\delta}\langle\hat{J}_z(t_i,\delta)\rangle\right]^2}. \tag{3.21}$$

To perform an explicit calculation, we will now choose a specific input state. We use a coherent spin state (CSS) [3] as input of the Rabi interferometer. This state corresponds to a Poissonian distribution of particles among the two wells, and thus contains no entanglement. For fermions, it is given by $|\mathrm{CSS}\rangle_F = \prod_{\vec{n}_\perp}\frac{1}{\sqrt{2}}\left(\hat{a}^\dagger_{r,\vec{n}_\perp} + \hat{a}^\dagger_{l,\vec{n}_\perp}\right)|0\rangle$, where $|0\rangle$ is the vacuum and the product runs over the first N excited states along the (x_2, x_3) directions, while for bosons $|\mathrm{CSS}\rangle_B = \frac{1}{\sqrt{N!}}\left[\frac{1}{\sqrt{2}}\left(\hat{a}^\dagger_{r,0} + \hat{a}^\dagger_{l,0}\right)\right]^N|0\rangle$. Such a quantum state is commonly prepared in double-well traps with ultracold bosonic atoms. The CSS is an eigenstate of $\hat{J}_x$, with the eigenvalue equal to $\frac{1}{2}N$, while $\langle\hat{J}_{y,z}\rangle = 0$ and $\langle\hat{J}^2_{y,z}\rangle = \frac{1}{4}N$. The exact expression for the sensitivity at time t_i is calculated with help of Eqs (3.17) and (3.21):

$$\Delta\delta(t_i) = \frac{E_J}{\sqrt{mN}}\frac{\sqrt{\left(\cos(\omega t_i) + \frac{\delta^2}{E_J^2}\right)^2 + \left(1 + \frac{\delta^2}{E_J^2}\right)\sin^2(\omega t_i)}}{\left|\frac{E_J^2-\delta^2}{\hbar^2\omega^2}\left[\cos(\omega t_i) - 1\right] - \frac{\delta^2 t_i}{\hbar^2\omega}\sin(\omega t_i)\right|}. \tag{3.22}$$

It can be simplified under assumptions $\frac{\delta^2}{E_J^2} \ll 1$ and $t_i \ll t_0 \equiv \hbar^2\omega/\delta^2$ (in Section III we show that this assumptions are well satisfied for typical experimental parameters). Then $\omega \simeq E_J/\hbar$, the relative population oscillates as

$$\langle\hat{J}_z(t_i,\delta)\rangle = \frac{N}{2}\frac{\delta}{E_J}\left[\cos\left(\frac{E_J t_i}{\hbar}\right) - 1\right], \tag{3.23}$$

and the sensitivity

$$\Delta\delta(t_i) = \frac{1}{\sqrt{mN}}\frac{E_J}{\left|\cos\left(\frac{E_J t_i}{\hbar}\right) - 1\right|} \tag{3.24}$$

scales at the shot noise limit, $\Delta\delta(t_i) \sim N^{-\frac{1}{2}}$. The smallest error $\Delta\delta_{\min} = E_J/2\sqrt{mN}$ is reached when $\frac{E_J t_i}{\hbar} = \pi(2j+1)$ with $j \in \mathbb{N}$.

3.3.4 Measurement of the Casimir-Polder force

In the RI, the atoms oscillate between the two wells in presence of an external force which creates a potential gradient along the splitting direction. This induces an energy difference among the two

wells, δ, whose value can be inferred from the measurement of population imbalance oscillations. Therefore, in order to have a sufficient signal to noise ratio on δ, the interferometer is best suited for measuring forces which decay on a scale of typical inter-well distances of a few microns.

As a specific application, in this subsection we examine the measurement of the Casimir-Polder force with a bosonic RI. We consider a BEC of $N = 2500$ ^{87}Rb atoms trapped in a double-well, with typical experimental parameters taken from [33], with the minima of the potential separated by $l = 4.8$ μm, and the hopping energy equal to $E_J/\hbar = 52.3$ s^{-1}. The force is induced by a surface positioned at a distance d of a few micrometers from one of the wells (see the inset of Fig.3.2 for a sketch of the experimental configuration).

Before coming to the calculations, let us discuss some technical aspects of the implementation. In [66], the temperature dependence of the Casimir-Polder force was measured with a dielectric surface at distances ranging from 7 to 11 micrometers from the cloud. Another option would be to use a metallic instead of dielctric surface. However, at distances of a few micrometers from magnetically or optically trapped atoms, the near-field magnetic noise originating from the metallic surface leads to decoherence and losses in the cloud, as observed in several experimental setups [31, 54, 52]. The underlying mechanism are the spin flip transitions induced by either thermal currents or technical noise creating oscillating magnetic fields [42]. Therefore, as also suggested by the measurement of trap lifetime made with a microfabricated silicon chip [57], a dielectric might be preferable for the measurement of Casimir-Polder force proposed here, since in this case a reduction in the condensate lifetime was observed only when the surface was close enough (less than two micrometers) to reduce the trap depth. As a final comment, we note that, even when near-field magnetic noise is relevant, the coherence time at distances of 5 micrometers from a metallic surface can be of the order of 1 second [83], allowing for the observation a few coherent Rabi oscillation (the typical Rabi period is about 100 ms). Moreover, as discussed below, the RI can operate at a fixed optimal time within the first period, with no need for multiple oscillations. The bosonic RI also requires the suppression of inter-atomic interactions (the impact of the two-body interactions on the sensitivity is discussed in the next subsection), which can be achieved via magnetic or optical Feschbach resonances.

Let us briefly introduce some properties of the Casimir-Polder force, acting between the atoms and a surface. The exact form of the potential, given in [2], depends on the dielectric properties of the atoms and the plate, as well as on the temperature T of the latter. If the thermal wavelength $\lambda_{th} = \frac{\hbar c}{k_B T}$ of the photons emitted from the plate is much larger than d (as it is for $d \simeq 5$ μm

when $T \leq 100$ K [4]), the Casimir-Polder potential is well approximated by

$$V_{\rm CP}(x_1;\ell) = -\frac{3\ \hbar\ c\ \alpha_0}{8\ \pi\ \ell^4}\ \frac{\varepsilon_0 - 1}{\varepsilon_0 + 1}\ \phi(\varepsilon_0), \tag{3.25}$$

where $\ell = x_1 + \frac{1}{2}l + d$ is the distance between the atoms and the surface. Here $c \simeq 3 \times 10^8\ \frac{\rm m}{\rm s}$ is the speed of light, $\alpha_0 = 47.3 \times 10^{-30}$ m^3 is the static value of ^{87}Rb atomic polarizability, and the function $\phi(\varepsilon_0)$, whose value is 0.8 for sapphire, is defined in [2]. If, on the other hand, the temperature of the plate is high ($T \gtrsim 300$ K), so that the condition $\lambda_{th} \gg d$ is not satisfied, the Casimir-Polder interaction is described by

$$V_{\rm CP}^{th}(x_1;\ell) = -\frac{k_B T\ \alpha_0}{4\ \ell^3}\ \frac{\varepsilon_0 - 1}{\varepsilon_0 + 1}\ . \tag{3.26}$$

In Fig. 3.2, we plot the detuning δ as a function of the distance d between the surface and the cloud, for three different temperatures. For this example, we have chosen a sapphire surface, with the static value of the dielectric function $\varepsilon_0 = 9.4$. When the plate is positioned at $d = 4\ \mu$m, we have $\delta/\hbar = 4.4\ s^{-1}$, $\frac{\delta^2}{E_J^2} = 0.007$ and $t_0 \simeq 3$ s. In order to compute the value of δ, one can numerically calculate $\psi_{l/r}$ using GP equation, as done for the mean-field two-mode model in subsection 1.7.5. The period of Rabi oscillations is $\omega = 120$ ms, and is much shorter than t_0, which justifies the use of the approximate Eq.(3.24) in order to evaluate the sensitivity.

Let us remark that, in the low-T limit, the potential $V_{\rm CP}$ is proportional to $\hbar$ and c and does not depend on the temperature of the surface, contrary to $V_{\rm CP}^{th}$. Therefore, if the sensitivity of the RI is sufficient to distinguish between the two regimes of Eqs. (3.25) and (3.26), it would be possible to discriminate between purely quantum and thermal effects.

In Fig. 3.2, the error bars around the dashed line give the uncertainty $\Delta\delta/\hbar$ of the Rabi interferometer fed by a CSS, obtained by fitting to $k = 10$ points at times $t_i = \frac{2\pi\hbar}{E_J}\frac{i}{k}$ within the first Rabi period, each with $m = 10$ measurements. The sensitivity is calculated with Eqs (3.20) and (3.24), also including a realistic estimate of the dominant experimental noise, as discussed below.

3.3.5 Sources of noise

Spin-polarized fermions are natural candidates for the implementation of the above interferometric scheme, since the particle-particle interaction is naturally suppressed by the Pauli exclusion principle. Ultracold fermi gases have been used to observe macroscopic Bloch oscillations induced

[4] The surface can be cooled down to T =4.2K; see T. Nirrengarten *et al.*, Phys. Rev. Lett. **97**, 200405 (2006) and T. Mukai *et al.*, Phys. Rev. Lett. **98**, 260407 (2007)

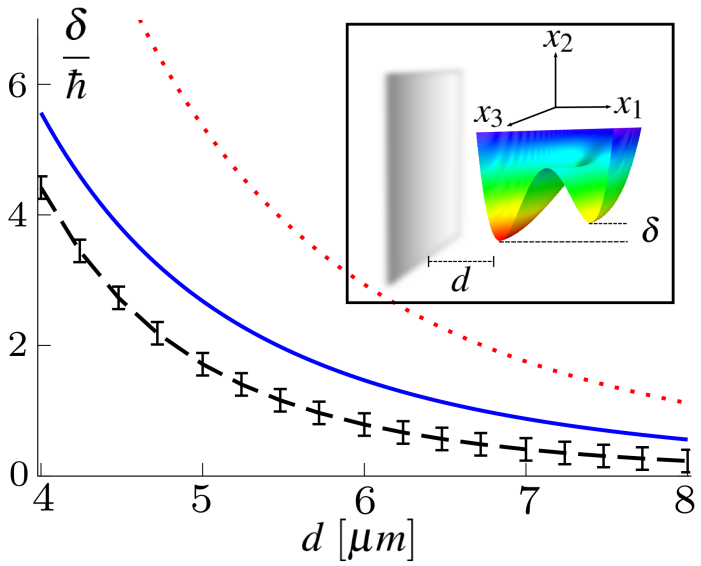

Fig. 3.2: The detuning $\delta/\hbar$, as a function of distance d, calculated with $V_{\rm CP}(x_1;d)$ (dashed black line), $V_{\rm CP}^{th}(x_1;d)$ at $T = 300$ K (solid blue line) and at $T = 600$ K (dotted red line). Error bars around the dashed black line show the corresponding sensitivity from Eq.(3.20) of a fit to $k = 10$ equally spaced points in the first Rabi period with $m = 10$ measurements at each time point. The uncertainty includes the effect of residual atom-atom interactions and limited resolution of the measurement of population imbalance (see text for details). The input state is the classical spin coherent state. The inset shows the trap configuration for measurement of the Casimir-Polder force.

by gravity in optical lattice [76], or perform Ramsey interferometry through Bragg diffraction [23].

In the case of bosons instead, the value of the s-wave scattering length can be strongly reduced by using Feshbach resonances, as already mentioned above. However, a residual interaction is always left. In the best situations so far experimentally realized, the scattering length has been tuned down to a =0.01 $\times$ Bohr radius; this has been demonstrated for ^{39}K atoms in [29]. The ratio $N\frac{E_c}{E_J}$ can thus be as small as 0.1. Such a small interaction can be taken into account by introducing an additional term $E_C\hat{J}_z^2$ in Hamiltonian (3.13), and calculating the first order correction to the evolution operator (3.16). We checked that, when $N\frac{E_C}{E_J} = 0.1$, the interactions marginally spoil the sensitivity.

Another important source of noise in the RI is given by the limited resolution on the popula-

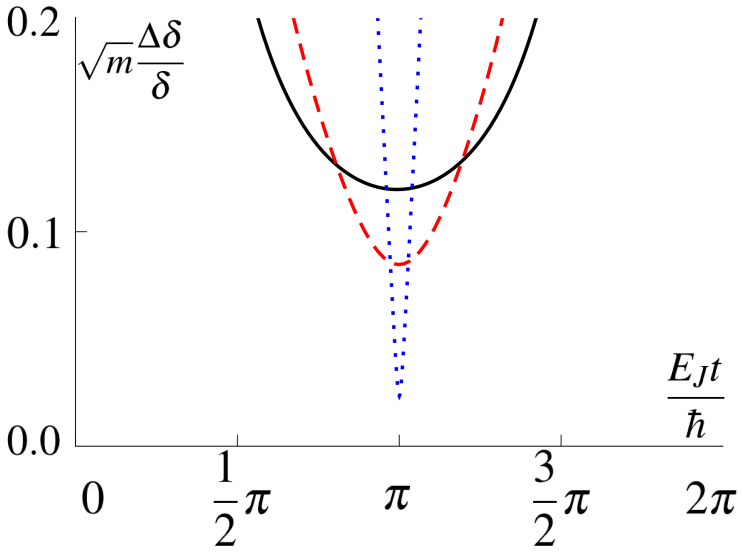

Fig. 3.3: The sensitivity $\sqrt{m}\Delta\delta$ as a function of time, in units of δ. Solid black, dashed red and dotted blue lines correspond to ξ^2 =1.0, 0.5, 0.017, respectively. The sensitivity is optimal at $\frac{E_J}{\hbar}t = \pi$. Here, $N = 2500$ and $\frac{\delta^2}{E_J^2} = 0.007$.

tion imbalance measurement. This can be taken into account by substituting the ideal probability $p(\{n\}|\delta)$ with the convolution $p_{\rm res}(\{n\}|\delta) = \int d\{n'\}\mathcal{P}(\{n\}|\{n'\})p(\{n'\}|\delta)$, where $\mathcal{P}(\{n\}|\{n'\})$ gives the probability to measure the population imbalance $\{n\}$, given the true value $\{n'\}$. We take $\mathcal{P}(\{n\}|\{n'\}) = \prod_{i=1}^{k}\left[\frac{1}{\sqrt{2\pi}\sigma_{\rm res}}\exp\left[-\frac{(n(t_i)-n'(t_i))^2}{2\sigma_{\rm res}^2}\right]\right]$, with a conservative value $\sigma_{\rm res} = 40$, i.e. the population imbalance is measured with a resolution of ± 40 particles. In this case, $\frac{\Delta\delta}{\delta}$ for the spin coherent state with 2500 atoms increases by a factor of two over the level of quantum noise. Yet, the sensitivity is sufficient to precisely distinguish between thermal and zero-temperature regimes of the Casimir-Polder force, as seen in Fig.3.2.

3.3.6 Interferometer with squeezed input states

So far, we have discussed the sensitivity of the RI with a coherent input state. Here we show that, keeping the number of atoms constant, higher sensitivity can be reached with spin squeezed states, such that $\xi^2 \equiv N\langle\hat{J}_z^2\rangle/\langle\hat{J}_x\rangle^2 < 1$ [90]. The squeezing parameter ξ^2 is equal to 1 for a CSS and decreases when reducing the fluctuations of $\hat{J}_z$ while the coherence is kept constant, $\langle\hat{J}_x\rangle \propto N$. In Fig.3.3, we plot the sensitivity $\Delta\delta$ as a function of time, for three different values

of the squeezing parameter. At a time t such that $\frac{E_J}{\hbar}t = \pi$, the sensitivity is optimal, and reads

$$\Delta\delta = \xi \frac{E_J}{2\sqrt{N}\sqrt{m}} \ , \tag{3.27}$$

showing a scaling $N^{-\frac{1}{2}}$ for the CSS and approaching N^{-1} in the limit of very strong squeezing. The figure also reveals that, for strong squeezing, the value of $\Delta\delta$ is small only around the optimal point. Therefore, it is reasonable to focus the experimental effort around this point, instead of acquiring data distributed over the whole Rabi period, as it was done for the fitting protocol described above. This allows to decrease $\Delta\delta$ by a factor which ranges from $\sqrt{k}$, in a strong squeezing limit, to $\sqrt{8/3}$, for a coherent state. Squeezed states can be created by adiabatically splitting an interacting BEC trapped in a double-well potential, as recently experimentally demonstrated in [27], where a state with $\xi^2 \simeq 0.6$ for $N \simeq 2200$ particles was prepared.

3.3.7 Comparison with other interferometric setups

The possibility to use cold/degenerate atoms for the measurement of forces at small distances has led to a number of proposals and experiments [17, 28, 39, 91, 68, 66]. In [66], the second derivative of the Casimir-Polder potential was deduced from the shift of the frequency of the collective oscillations of a BEC in a trap put below a surface. The precision of the experiment was not sufficient to make a distinction between thermal and zero-temperature regimes. We notice that, differently from [66], the Rabi interferometer provides the value of δ, which is related to the first spatial derivative of the perturbing potential. On the theoretical side, the Ref. [17] proposes to estimate the strength of the interaction between the atoms and a surface using the frequency shift of Bloch oscillations of a cold either fermionic or bosonic gas in a vertical optical lattice. An important aspect of this proposal is the scaling of the sensitivity $\Delta\delta \sim t^{-1}$ with the oscillation time t. The Rabi interferometer does not benefit from time scaling for the typical experimental times. However, the phase estimation with the Rabi interferometer has two important advantages with respect to those proposals. First, the perturbing potential is deduced from the measurement of the number of particles, not from the interference pattern of an atomic cloud released from the optical lattice [17, 28]. Counting atoms in dilute samples by making use of resonant light beams is a promising technique [8, 27] and is expected to reach a very high signal to noise ratio. Moreover, differently from the Bloch oscillation proposal, the sensitivity of the Rabi interferometer can be quantum-enhanced by the use of proper particle-entangled states. As shown above, the phase sensitivity $\Delta\delta \sim N^{-\beta}$ scales at the shot noise $\beta = 1/2$ for the CSS and can be further increased $1/2 < \beta < 1$ for spin squeezed states.

Let us finally compare our RI to the the Mach Zehnder interferometer. The latter has two important advantages: i) the wells can be separated far apart, allowing for the measurement of forces having larger langth scales, and ii) the sensitivity is scaling with the inverse of time. Next, we compare the sensitivity of the RI and the MZI fed with the CSS. When $\frac{\delta^2}{E_J^2} \ll 1$, the difference between the sensitivities of the MZI and the RI grows in time. The smallest difference is $\Delta\delta = \frac{\pi}{2}\Delta\delta_{\mathrm{MZI}}$, obtained at the the first optimal time (equal to 60 ms for $\delta/\hbar = 4.4$ s^{-1} and $E_J/\hbar = 52.3$ s^{-1}).

The MZI can thus in general be regarded as a better interferometer than the RI, with the only disadvantage of a difficult double-well implementation of a more complicated interferometric sequence. As already argued, this constitutes indeed the main motivation leading to the proposal of the RI, which does not require any coherent splitting/recombination of the atomic cloud.

3.4 Outlook

We have shown that a degenerate either bosonic or fermionic gas in a double-well potential can constitute a sensitive device for measuring short-range interactions, as the Casimir-Polder force. We have demonstrated that, when the Rabi interferometer is fed with a classical spin coherent state with moderate number of atoms, the Casimir-Polder force can be measured with precision sufficient to distinguish between its thermal and quantum, zero-temperature regime. Our predictions include possible sources of noise, as imperfect detection and residual atomic interaction, and optimization of the population imbalance measurement.

As a further application to detection of weak forces, one can think of the same Rabi protocol described here for the measurement of the Casimir-Polder potential, to be used for instance to estimate the maximum size of possible corrections to the Newton's law of gravitation due to the conjecture that gravity propagates in more than three spacial dimensions. Preliminary calculations suggest that the higher bound to these corrections, set by previous experiments, could be further decreased using the Rabi Interferometer with typical double-well parameters and a spin coherent input state.

3.5 Implementation in double-well traps II: atom position measurement and two-slit interference

This section is based on the work: **Phase Estimation With Interfering Bose-Condensed Atomic Clouds**, J. Chwedeńczuk [*INO-CNR, BEC Center, and Dipartimento di Fisica, Via Sommarive 14, 38123 Povo, Trento, Italy*], F.P., and A. Smerzi [*INO-CNR, BEC Center, and Dipartimento di Fisica, Via Sommarive 14, 38123 Povo, Trento, Italy*], published in Phys. Rev. A **82**, 051601(R) (2010). Some of the results presented here are taken from an extended version of the above manuscript, arXiv:1012.3593.

The essential part of an interferometer is obviously the phase accumulation stage, which, in the linear two-mode case, is described by the operator $\exp\big(-i\theta\hat{J}_z\big)$. As discussed in subsection 3.1.1, after this, the interferometric sequence must necessarily be closed by a recombination of the two arms, which is typically performed through a beam splitter, $\exp\big(-i(\pi/2)\hat{J}_x\big)$. In a double-well setup, the beam splitter is implemented by a suitable dynamic manipulation of the inter-well barrier. In the Mach-Zehnder interferometer, the beam splitter takes place after the phase shift (see Eq. (3.2)), but we have seen from the above example of the Rabi interferometer that, even if these two parts of the sequence are carried on at the same time, the scheme works, and sub-shot noise sensitivity can still be reached with this simpler sequence.

In this section, we will study another way of simplifying the interferometric sequence, this time upon removing the beam splitter, and recombining the two arms of our double-well interferometer by releasing the particles from the trap to form a two-slit interference pattern.

3.5.1 Overview of the main results

Starting from the idea that the recombination of the two-modes can be realized just by releasing them form the double-well trap, so that they form a two-slit interference pattern (as shown in Fig.3.4), in this section we discuss how the information about the phase can be extracted from this pattern, and derive the sensitivity for different estimation strategies, all based on the measurement of atom positions.

First, we demonstrate that by performing a least-squares fit to the measured density [80], the estimation sensitivity $\Delta\theta$ is bounded by the shot-noise.

In order to overcome this limit, high-order spatial correlation functions must be measured,

namely, of order not smaller than $\sqrt{N}$, where N is the total number of particles. In particular, when the estimation is performed using the N-th order correlation function, the sensitivity saturates the bound set by the Quantum Fisher Information (3.7). We then analyze an estimation scheme based on the detection of the position of the center-of-mass of the interference pattern, which can still yield sub-shot-noise sensitivity. Even though allowing for the highest possible phase estimation sensitivities, these schemes might prove experimentally very challenging, since they require a very efficient single-atom detection (in the center-of-mass protocol every single atom must be counted), and, in the case of the correlation function estimator, a very long calibration stage.

The necessity to measure high-order correlations comes from the overlap between the modes, which washes out the information about the phase shift. Indeed, we finally study the sensitivity of the Mach-Zehnder interferometer, and we observe that a non-zero overlap between the wave-packets dramatically reduces the sensitivity.

3.5.2 The model

The interferometric sequence we analyze here is made of just two parts: i) a phase shift, $\hat{U}(\theta)= e^{-i\theta \hat{J}_z}$ acts on the input state $|\psi_{\rm in}\rangle$, and ii) the double-well trap is suddenly switched off and the cloud freely expands. The goal is, as usual, to estimate the phase θ, which we suppose be caused by some external effect we want to measure.

As done in the previous section, we adopt a two-mode approximation, which corresponds to writing the many-body field operator as

$$\hat{\Psi}(x,t) = \psi_{\rm l}(x,t)\hat{a}_{\rm l} + \psi_{\rm r}(x,t)\hat{a}_{\rm r}, \tag{3.28}$$

where $\hat{a}^\dagger_{\rm l/r}$ creates a particle in the left/right well. Differently from the previous section, we consider here only the problem along the splitting direction, x, and only bosonic particles, so that the collective angular momentum operators (3.14) become

$$\begin{aligned}
\hat{J}_x &\equiv \frac{1}{2}(\hat{a}^\dagger_{\rm l}\hat{a}_{\rm r} + \hat{a}^\dagger_{\rm r}\hat{a}_{\rm l}) \ , \\
\hat{J}_y &\equiv \frac{1}{2i}(\hat{a}^\dagger_{\rm l}\hat{a}_{\rm r} - \hat{a}^\dagger_{\rm r}\hat{a}_{\rm l}) \ , \\
\hat{J}_z &\equiv \frac{1}{2}(\hat{a}^\dagger_{\rm l}\hat{a}_{\rm l} - \hat{a}^\dagger_{\rm r}\hat{a}_{\rm r}) \ .
\end{aligned} \tag{3.29}$$

In order to describe the expansion after the trap release, the two mode functions $\psi_{\rm l/r}(x,t)$ include the dependence on time.

As anticipated, at the output of the interferometer, that is, after a time sufficient for the two modes to overlap and form an interference pattern, the positions of the particles are measured. The whole statistical information about the positions of particles is contained in the conditional probability of finding N particles at positions $\vec{x}_N = (x_1 \dots x_N)$ [50, 18, 63]. This probability, $p_N(\vec{x}_N|\theta) = (1/N!)G_N(\vec{x}_N, \theta)$, is expressed in terms of the N-th order correlation function

$$G_N(\vec{x}_N, \theta) = \langle \psi_{\rm out}|\hat{\Psi}^\dagger(x_1,t)\dots\hat{\Psi}^\dagger(x_N,t)\hat{\Psi}(x_N,t)\dots\hat{\Psi}(x_1,t)|\psi_{\rm out}\rangle \ . \tag{3.30}$$

Here, $|\psi_{\rm out}\rangle$ denotes the state after the phase shift transformation, $|\psi_{\rm out}\rangle = \hat{U}(\theta)|\psi_{\rm in}\rangle$.

We decompose the initial state in the well-population basis, $|\psi_{\rm in}\rangle = \sum_{n=0}^{N} C_n|n, N-n\rangle$, and suppose that the expansion coefficients are real and posses the symmetry $C_n = C_{N-n}$. As we will argue later, such choice of C_n's is natural in context of this work. We switch from the Schrödinger to the Heisenberg representation, where the field operator evolves according to,

$$\hat{\Psi}_\theta(x,t) \equiv \hat{U}^\dagger(\theta)\hat{\Psi}(x,t)\hat{U}(\theta) = \psi_{\rm l}(x,t)e^{i\frac{\theta}{2}}\hat{a}_{\rm l} + \psi_{\rm r}(x,t)e^{-i\frac{\theta}{2}}\hat{a}_{\rm r}. \tag{3.31}$$

In order to write $p_N(\vec{x}_N|\theta)$ in a useful form [63], we use the basis of coherent phase states, already introduced in the previous section, which is parametrized by the phase angle φ: $|\varphi, N\rangle = (1/\sqrt{2^N N!})\big(\hat{a}_{\rm l}^\dagger + e^{i\varphi}\hat{a}_{\rm r}^\dagger\big)^N|0\rangle$ (where $|0\rangle$ is the vacuum state). The action of the field operator on these states can be written in a simple form, $\hat{\Psi}_\theta(x,t)|\varphi, N\rangle = \sqrt{N/2}\ u_\theta(x,\varphi;t)|\varphi, N-1\rangle$, where

$$u_\theta(x,\varphi;t) = \psi_{\rm l}(x,t)e^{\frac{i}{2}(\theta+\varphi)} + \psi_{\rm r}(x,t)e^{-\frac{i}{2}(\theta+\varphi)}. \tag{3.32}$$

By expanding the Fock states in the basis of the coherent states
$|n, N-n\rangle = \sqrt{2^N/\binom{N}{n}}\int_0^{2\pi}(d\varphi/2\pi)e^{-i\varphi(N-n)}|\varphi, N\rangle$, we can easily write the result of the action of the field operator on the input state,

$$\hat{\Psi}_\theta(x,t)|\psi_{\rm in}\rangle = \sqrt{\frac{2^N N}{2}}\sum_{n=0}^{N}\frac{C_n}{\sqrt{\binom{N}{n}}}\int_0^{2\pi}\frac{d\varphi}{2\pi}e^{-i\varphi(N-n)}u_\theta(x,\varphi;t)|\varphi, N-1\rangle. \tag{3.33}$$

Using Eq. (3.33), we can express the probability $p_N(\vec{x}_N, \theta)$ as

$$\begin{aligned} p_N(\vec{x}_N|\theta) &= \int_0^{2\pi}\int_0^{2\pi}\frac{d\varphi}{2\pi}\frac{d\varphi'}{2\pi}\prod_{i=1}^{N}u_\theta^*(x_i,\varphi;t)u_\theta(x_i,\varphi';t) \\ &\times \sum_{n,m=0}^{N}\frac{C_nC_m\cos\left[\varphi\left(\frac{N}{2}-n\right)\right]\cos\left[\varphi'\left(\frac{N}{2}-m\right)\right]}{\sqrt{\binom{N}{n}\binom{N}{m}}}. \end{aligned} \tag{3.34}$$

In the remaining part of this section, we will always choose t large enough so that the two modes $\psi_{\rm l/r}$ fully overlap, and the interference pattern is formed. In this regime, the relevant quantities

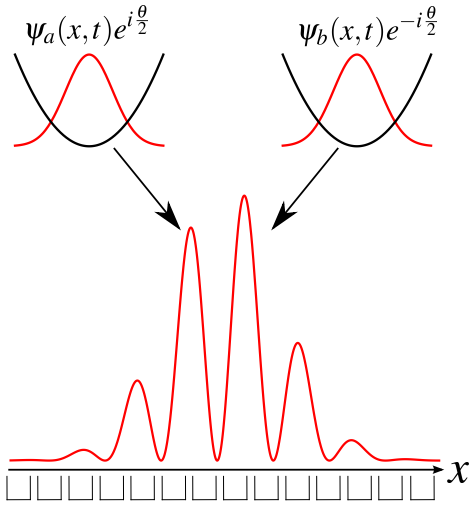

Fig. 3.4: Schematic representation of the interferometric procedure. First, a relative phase θ is imprinted between the wells. Then, the BECs are released from the trap and form an interference pattern. The detectors (symbolically represented as open squares) measure the positions of atoms.

change only by a scaling with $\sim \sqrt{t}$ of the characterisitc dimensions of the system (see below for quantitative arguments). The probability (3.34) is the starting point for the following discussion of various phase estimation strategies.

3.5.3 Estimation via the fit to the density

The simplest way of estimating the value of θ is by fitting the average density to the interference pattern, as the position of the maximum depends on the relative phase between the two clouds. Such fit is commonly employed with BECs in double-wells, in order to determine, for instance, the phase coherence in the system [5, 27].

The formalism we will employ to treat the fit of the average density is analogous to the one used for the fit in time of the population imbalance oscillations, studied in the previous section. In the experimental imaging of the expanded cloud, the interference pattern is sampled using M bins located at positions x_i $(i = 1 \dots M)$. The number of particles n_i in each bin is measured m times, giving the set $n_i^{(k)}$, $k = 1, ..., m$. The function $n_{\rm fit}(i, \theta)$, $i = 1, ..., M$, with free parameter θ is then fitted to the histogram of the measured density $\{x_i, \bar{n}_i\}, i = 1, ..., M$, where $\bar{n}_i = \sum_{k=1}^{m} n_i^{(k)}/m$. As discussed in the previous section, the function $n_{\rm fit}(i, \theta)$ must

be constructed in the calibration stage, and we again assume that the technical/thermal noise is negligible, such that, after a sufficient number of experiments, $n_{\rm fit}$ tends to the quantum mechanical average $\langle n_i \rangle$, which can be calculated from the N-particle probability (3.34):

$$\langle n_i \rangle = N \int\limits_{\Delta x_i} dx_1 \int\limits_{-\infty}^{\infty} d\vec{x}_{N-1}\, p_N(\vec{x}_N|\theta) = \int\limits_{\Delta x_i} dx_1 G_1(x_1|\theta), \tag{3.35}$$

where $G_1(x_1|\theta) = \langle \Psi_\theta^\dagger(x_1,t)\Psi_\theta(x_1,t)\rangle$ is the one-particle density. If we further assume that the size Δx of each of the M bins is much smaller than the length scale of oscillation of the interference pattern, then $\langle n_i \rangle$ is proportional to the average density

$$\langle n_i \rangle = G_1(x_i,\theta)\Delta x. \tag{3.36}$$

The value of θ is determined from the least squares formula

$$\frac{d}{d\theta} \sum_{i=1}^{M} \frac{(\bar{n}_i - \langle n_i \rangle)^2}{2\Delta^2 n_i/m} = 0. \tag{3.37}$$

Here again we assumed the thermal/technical noise to be negligible, so that also the fluctuations in each bin, $\sum_{k=1}^{m}(n_i^{(k)} - \bar{n}_i)^2$, tend, for sufficienlty large m, to the quantum mechanical average

$$\Delta^2 n_i = \langle n_i^2 \rangle - \langle n_i \rangle^2 = \int\limits_{\Delta x_i} dx_1\ G_1(x_1,\theta) + \int\limits_{\Delta x_i}\int\limits_{\Delta x_i} d\vec{x}_2\ G_2(\vec{x}_2,\theta) - \langle n_i \rangle^2\ , \tag{3.38}$$

which, in the small bin limit, reads

$$\Delta^2 n_i = G_1(x_i,\theta)\Delta x + \left[G_2(x_i,x_i,\theta) - G_1^2(x_i,\theta)\right](\Delta x)^2. \tag{3.39}$$

From Eq. (3.39), we see that the bin fluctuations get a contribution from quantum correlations, proportional to G_2. For a coherent spin state, where no particle correlations are present $G_2 = G_1^2$, the fluctuations are Poissonian, $\Delta^2 n_i = G_1(x_i,\theta)\Delta x$. As explained in subsection 3.1.2, the sensitivity for such state is limited by the shot-noise. Thefore, we might guess that for an entangled state, satisfying $G_2 \neq G_1^2$, the fluctuations (3.39) could in some cases improve the sensitivity below the shot-noise.

To verify this guess, we need to determine how the quantum fluctuations $\Delta^2 n_i$ in the i-th bin influence the sensitivity of the phase estimation via the fit (3.37). To this end, we will construct a MLE estimator which coincides with the fit estimator, and then use the CRLB (3.4) to calculate the sensitivity, as done in the previous section for the Rabi interferometer. If the number of measurements m is large, then according to the central limit theorem the probability distribution

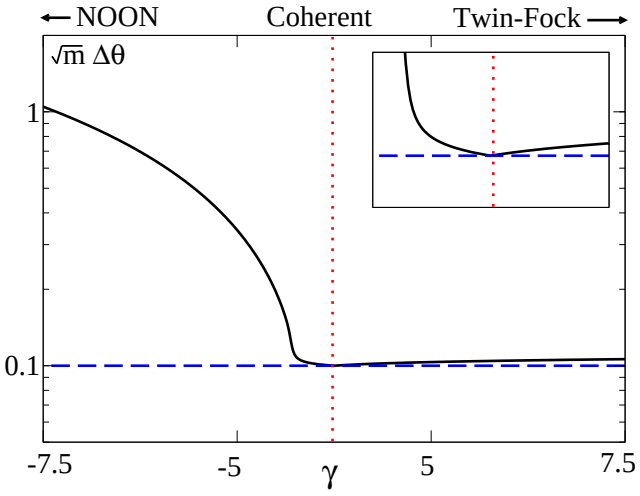

Fig. 3.5: Sensitivity $\sqrt{m}\Delta\theta$ of the phase estimation from the fit to the density, as a function of $|\psi_{\rm in}\rangle \in \mathcal{A}$ (solid black line) with $N = 100$ particles. The blue dashed line represents the shot-noise limit. The horizontal dotted red line indicates the position of the coherent state. Clearly, the sensitivity is bounded by the shot-noise. The inset shows the behavior of the sensitivity in the vicinity of the coherent state.

for the average $\bar{n}_i$ in the i-th bin tends to the Gaussian $p(\bar{n}_i|\theta) = \big(1/(\sqrt{2\pi}\Delta n_i/\sqrt{m})\big)exp\big(-(\bar{n}_i - \langle n_i\rangle)^2/(2\Delta^2 n_i/m)\big)$. In every shot the atom counts are correlated between the bins. However, in order to link the MLE with the sensitivity of the least squares fit, we construct the total probability, which we have to maximize, as if the measurement results $\bar{n}_i$ and $\bar{n}_j$, with $i \neq j$, were uncorrelated. This last step constitutes a difference between the spacial fit considered here and the time fit of the previous section. Indeed, in the latter case, measurements made at different times are rightfully considered as independent, since in a typical experiment they would belong to different runs, that is, would be performed on different atomic clouds.

Taking the total probability of measuring the values $\{\bar{n}\} = (\bar{n}_1 \dots \bar{n}_M)$ as a product $P(\{\bar{n}\}|\theta) = \prod_{i=1}^{M} p(\bar{n}_i|\theta)$, we see once again that its maximization, $\frac{d}{d\theta}P(\{\bar{n}\}|\theta) = 0$ corresponds to the least squares formula Eq.(3.37). So the fit sensitivity coincides with the MLE sensitivity, given by the CRLB (3.4), with the FI,

$$F = \sum_{\bar{n}_1 \dots \bar{n}_M = 0}^{N} \frac{1}{P(\{\bar{n}\}|\theta)} \left(\frac{\partial}{\partial\theta}P(\{\bar{n}\}|\theta)\right)^2 \xrightarrow{m\gg 1} m\sum_{i=1}^{M} \frac{1}{\Delta^2 n_i}\left(\frac{\partial\langle n_i\rangle}{\partial\theta}\right)^2. \tag{3.40}$$

In the remainder of this subsection, we will demonstrate that the fit sensitivity $\Delta\theta$ is bounded

by the shot-noise, which falsifies our previous guess. Let us assume for the moment that the second term in the Eq.(3.39),which is proportional to $(\Delta x)^2$, can be neglected. Then, as it is for a coherent state, the particle number distribution is Poissonian, and we expect the sensitivity to be worse than shot noise, as we show next.

The FI from (3.40) reads

$$F = m\sum_{i=1}^{M}\frac{1}{G_1(x_i,\theta)}\left(\frac{\partial}{\partial\theta}G_1(x_i,\theta)\right)^2\Delta x \simeq mN\int_{-\infty}^{\infty}dx\frac{1}{p_1(x|\theta)}\left(\frac{\partial}{\partial\theta}p_1(x|\theta)\right)^2, \tag{3.41}$$

with the one-particle probability

$$p_1(x|\theta) = \frac{1}{2}(|\psi_{\rm l}(x,t)|^2 + |\psi_{\rm r}(x,t)|^2) + \frac{2}{N}\langle\hat{J}_x\rangle{\rm Re}\left[\psi_{\rm l}^*(x,t)\psi_{\rm r}(x,t)e^{i\theta}\right]. \tag{3.42}$$

Making a model for the spacial modes $\psi_{\rm l/r}(x,t)$, we can now calculate the FI (3.41) explicitly. As the interference pattern is formed after long expansion time, the mode functions can be written as [69]

$$\psi_{\rm l/r}(x,t) \simeq \frac{1}{\tilde{\sigma}}\ \exp\left(i\frac{x^2}{2\tilde{\sigma}^2} \mp i\frac{x\ x_0}{\tilde{\sigma}^2}\right)\ \tilde{\psi}(\frac{x}{\tilde{\sigma}^2}), \tag{3.43}$$

where $\tilde{\sigma} = \sqrt{\frac{\hbar t}{m}}$, $\tilde{\psi}$ is the Fourier transform of the initial wave-packets, common for $\psi_{\rm l}$ and $\psi_{\rm r}$, and the separation of the wells is $2x_0$. This gives $F = mN\int_{-\infty}^{\infty}(dx/\tilde{\sigma}^2)\ \left|\tilde{\psi}(x/\tilde{\sigma}^2)\right|^2(a^2\sin^2\varphi)/(1 + a\cos\varphi)$, with $a = \frac{2}{N}\langle\hat{J}_x\rangle$ and $\varphi = 2\ x\ x_0/\tilde{\sigma}^2+\theta$. Notice that when the expansion time is long, the function $\tilde{\psi}$ varies slowly, as compared to the period of oscillations of $\sin\varphi$ and $\cos\varphi$. Therefore, in the above expression, one can substitute the oscillatory part with its average value. Using the normalization of $\tilde{\psi}$ we obtain

$$F = mN\ \frac{a^2}{2}\ \frac{1-(-1+\sqrt{1-a^2})^2}{1+a(-1+\sqrt{1-a^2})} \tag{3.44}$$

Since $0 \le a \le 1$, we have $0 \le F \le mN$. Therefore, when the term proportional to $(\Delta x)^2$ in the fluctuations (3.39) can be neglected, the sensitivity

$$\Delta\theta \ge \Delta\theta_{SN} = \frac{1}{\sqrt{m}}\frac{1}{\sqrt{N}} \tag{3.45}$$

for any two-mode input state ($\Delta\theta_{SN}$ denotes the shot-noise sensitivity).

Below, we will argue that the inclusion of the second term, accounting for particle correlation contribution to the fluctuations in (3.39), does not improve the sensitivity.

In Eq.(3.39), the first term $G_1(x_i,\theta)\Delta x$ scales linearly with the particle number N, while the second term, as a function of N, is a polynomial of the order not higher than two, $\lambda_2\ N^2 + \lambda_1\ N + \lambda_0$. The fluctuations $\Delta^2 n_i$ must be positive, thus $\lambda_2\ \ge 0$. Otherwise, for large enough

N, no matter how small Δx, we would have $\Delta^2 n_i < 0$. If $\lambda_2 > 0$, the positive second term in Eq. (3.39) enlarges the fluctuations and thus worsens the sensitivity. Finally, if $\lambda_2 = 0$, the first and second terms in Eq.(3.39) scale linearly with N, and for small Δx the first term always dominates, thus we end up again with Eq.(3.41)[5].

To conclude this analysis of the fit estimator, we will study the dependence of the sensitivity $\Delta\theta$ on the input state $\psi_{\rm in}$. We consider the ground states of the condensate in a symmetric double-well potential, using the two-mode Hamiltonian (3.12) with $\delta = 0$. We construct a family of states $\mathcal{A}$ by finding ground states of Eq. (3.12) for various values of the ratio $\gamma = \frac{E_C}{NE_J}$. For $\gamma > 0$, the elements of $\mathcal{A}$ are number-squeezed states and tend to the twin-Fock state $|\psi_{\rm in}\rangle = \left|\frac{N}{2}, \frac{N}{2}\right\rangle$ with $\gamma \to \infty$. For $\gamma < 0$, the elements of $\mathcal{A}$ are phase-squeezed states [37]. With $\gamma \to -\infty$, the ground state of (3.13) tends to the NOON state $|\psi_{\rm in}\rangle = \frac{1}{\sqrt{2}}(|N,0\rangle + |0,N\rangle)$. With $\gamma = 0$ we have a spin coherent state, $|\psi_{in}\rangle = \frac{1}{\sqrt{N!}}\left(\frac{\hat{a}_1^\dagger + \hat{a}_r^\dagger}{\sqrt{2}}\right)^N |0\rangle$. Notice that for all $|\psi_{\rm in}\rangle \in \mathcal{A}$, the coefficients C_n are real and symmetric. For each state in $\mathcal{A}$, we calculate $a = \frac{2}{N}\langle \hat{J}_x \rangle$, and insert it into Eq.(3.44). The sensitivity $\Delta\theta$, shown in Fig.3.5, is clearly bounded by the shot noise. The best sensitivity, exactly equal to the shot noise, is reached for a coherent state.

The value of the FI given by Eq.(3.41) is expressed in terms of a single-particle probability. We expected the useful non-classical many body correlations to decrease the value of $\Delta\theta$, but the FI (3.41) is however insensitive to these correlations, and is thus bounded by the shot-noise. In the next subsection, we demonstrate that the estimation based on the measurement of position correlations can instead improve the phase sensitivity below the SQL.

3.5.4 Estimation via the correlation functions

In the estimation protocol discussed next, the phase θ is deduced from the measurement of the k-th order correlation function $G_k(\vec{x}_k|\theta)$, involving the aquisition of a set of k particles positions $\vec{x}_k$. We choose again to deduce θ using a MLE with the probability $p_k(\vec{x}_k|\theta) = ((N-k)!/N!)G_k(\vec{x}_k|\theta)$, where, in each experiment, the phase is chosen from the condition $\frac{d}{d\theta}p_k(\vec{x}_k|\theta) = 0$. In the calibration stage, the probability function to be used for the MLE must be constructed by repeating the experiment with different known values of θ. We assume that the calibration provides a probability coinciding with the quantum mechanical average p_k, meaning that we are neglecting thermal/technical noise. After a sufficiently large number m of experiments, the

[5] A similar argument shows that increasing Δx also worsens the sensitivity with respect to Eq.(3.41)

sensitivity saturates the CRLB,

$$\Delta^2\theta = \frac{1}{m}\frac{1}{F_{(k)}}, \tag{3.46}$$

with the FI

$$F_{(k)} = \frac{N}{k}\int_{-\infty}^{\infty} d\vec{x}_k \frac{1}{p_k(\vec{x}_k|\theta)}\left(\frac{\partial}{\partial\theta}p_k(\vec{x}_k|\theta)\right)^2, \tag{3.47}$$

where the coefficient N/k accounts for the number of independent drawings of k particles from N, i.e. $\binom{N}{k}/\binom{N-1}{k-1}$. Indeed, when drawing k particles from N in all possible ways, one takes $\binom{N-1}{k-1}$ times the same particle.

We notice that, by setting $k = 1$, i.e. the estimator is the single-particle density, we recover the FI from Eq.(3.41). Therefore, the measurement of positions of N particles used as independent is, in terms of sensitivity, equivalent to fitting the average density to the interference pattern, and is limited by the shot-noise.

One of the main results presented in this section, comes from analyzing the estimation sensitivity when the full N-body density correlation function is measured. By using the general form (3.43) of the mode functions $\psi_{\mathrm{l/r}}$ in Eq. (3.32), then inserting the probability (3.34) in the FI Eq.(3.47), and exchanging the order of integration between phase and space, we get

$$F_{(k=N)} = 4\sum_{n=0}^{N} C_n^2\left(n - \frac{N}{2}\right)^2 = 4\Delta^2\hat{J}_z = F_Q. \tag{3.48}$$

Here, the F_Q, defined in Eq. (3.7), is the QFI in the case of pure states. Since our interferometric transformation is simply given by the phase shift $\exp\left(-i\theta J_z\right)$, we have $F_Q = 4\Delta^2\hat{J}_z$. The above equation tells us that the N-body density correlation provides an optimal measurement, since, as we learned in subsection 3.1.2, the QFI results from a maximization of the FI over all possible measurements.

The question now is thus for which input state this optimal measurement can also give a sub-shot-noise sensitivity. As denoted by open circles in Fig.3.6, the Eq.(3.48) gives $\Delta\theta = \sqrt{m}\Delta\theta_{SN}$ for the coherent state ($\gamma = 0$), and overcomes this bound for all $|\psi_{\mathrm{in}}\rangle \in \mathcal{A}$ with $\gamma < 0$. The NOON state gives the Heisenberg limit,

$$\Delta\theta_{HL} = \frac{1}{\sqrt{m}}\frac{1}{N}. \tag{3.49}$$

We now discuss how the sensitivity given Eq.(3.46) changes for $k < N$. This question is important for experimental purposes, since the measurement of the N-body correlation requires single-atom resolution with 100% efficiency. The space integrals for $k \neq 1, N$ cannot be evaluated

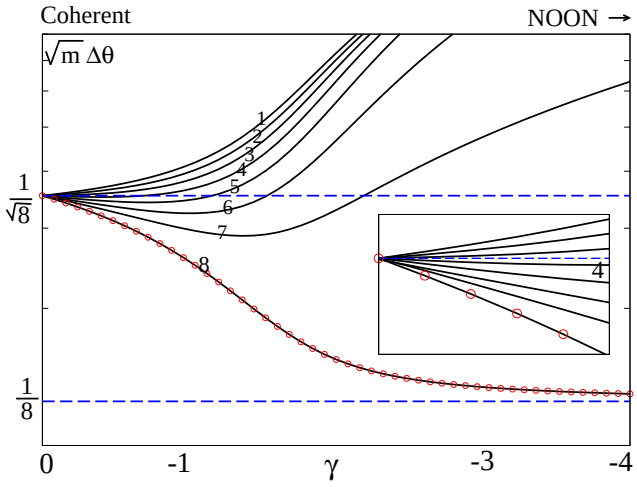

Fig. 3.6: The sensitivity $\sqrt{m}\Delta\theta$ (black solid lines), calculated by numerical integration of the Eq.(3.47) for various k, as a function of $|\psi_{in}\rangle \in \mathcal{A}$ with $\gamma < 0$ and $N = 8$. The two limits, $\sqrt{m}\Delta\theta_{SN}$ and $\sqrt{m}\Delta\theta_{HL}$ are denoted by the upper and lower dashed blue lines, respectively. The optimal sensitivity, given by the QFI, is drawn with red open circles. The inset magnifies the vicinity of the coherent state, showing that the sub-shot-noise sensitivity is reached starting from $k_{\min} = 4$.

analytically, thus we calculate the FI numerically, taking Gaussian wave-packets

$$\tilde{\psi}(\frac{x}{\tilde{\sigma}^2}) = \left(\frac{2\sigma_0^2}{\pi}\right)^{\frac{1}{4}} \exp\left(-\frac{x^2\sigma_0^2}{\tilde{\sigma}^4}\right) \tag{3.50}$$

with the initial width $\sigma_0 = 0.1$ and half of the well separation $x_0 = 1$. The Fig.3.6 shows the sensitivity (3.46) as a function of $|\psi_{\text{in}}\rangle \in \mathcal{A}$ with $N = 8$ atoms, for $k = 1, ..., 8$. The sensitivity improves with growing k, and goes below the shot-noise limit at $k_{\min} = 4$.

For higher numbers of particles, we numerically checked that $k_{\min}$ tends to $\sqrt{N}$. Therefore, one would have to measure the correlation function of the order of at least $\sqrt{N}$ in order to beat the shot-noise limit.

In a realistic experiment with cold atoms, where $N \simeq 1000$, it would be very difficult to use the correlation function of such high order for phase estimation. The biggest difficulty resides in the calibration stage, during which one would need to experimentally probe a function of a k dimensional variable $\vec{x}_k$ (with $k > \sqrt{N}$), and for different values of the phase θ.

In the next sub section we present a phase estimation scheme based on the measurement of the center-of-mass of the interference pattern. Although the probability for measuring the

center-of-mass at position x is a function of just a one-dimensional variable, it can still provide the sub-shot-noise sensitivity. Nevertheless, we will see that the achievement of sub-shot noise sensitivity with this estimation protocol is still challenging.

3.5.5 Estimation via the center-of-mass measurement

In the estimation protocol we discuss now, after all the N particles are detected at positions $\vec{x}_N$, the center-of-mass coordinate

$$x = \frac{1}{N}\sum_{i=1}^{N} x_i \tag{3.51}$$

is recorded. The phase θ is obtained from a MLE, with the probability $p_{\rm cm}(x|\theta)$, describing the statistics of the center-of-mass position. As anticipated, the calibration stage has the advantage, with respect to the correlation function estimation described before, that the function to be constructed depends on a one-dimensional variable. The probability $p_{\rm cm}(x|\theta)$ can be obtained from the full N-body probability (3.34): $p_{\rm cm}(x|\theta) = \int d\vec{x}_N\, \delta\big(x - (1/N)\sum_{i=1}^{N} x_i\big) p_N(\vec{x}_N|\theta)$, where "$\delta$" is the Dirac delta. To provide an analytical expression for this probability, we model the mode-functions by Gaussians as in Eq.(3.50). Using a realistic assumption that the initial separation of the wave-packets is much larger than their width, i.e. $\exp\big(-x_0^2/\sigma_0^2\big) \ll 1$, we obtain

$$p_{\rm cm}(x|\theta) = \sqrt{\frac{2\sigma_0^2 N}{\pi\tilde{\sigma}^4}}\exp\left(-\frac{2x^2\sigma_0^2}{\tilde{\sigma}^4}N\right)\left[1 + \frac{1}{2}(C_0 + C_N)^2\cos\left(N\theta + \frac{2Nx_0}{\tilde{\sigma}^2}x\right)\right]. \tag{3.52}$$

Remarkably, the above probability depends on θ only for states with non-negligible NOON components, C_0 and C_N, as already noticed in [4].

Estimating θ using MLE, the sensitivity is given by the CRLB, $\Delta\theta^2 = 1/mF_{\rm cm}$, and the FI can be calculated analytically,

$$F_{\rm cm} = \int_{-\infty}^{\infty} \frac{dx}{p_{cm}(x|\theta)}\left(\frac{\partial}{\partial\theta}p_{cm}(x|\theta)\right)^2 = N^2\left[1 - \sqrt{1 - \frac{1}{2}(C_0 + C_N)^2}\right], \tag{3.53}$$

where m is the number of experiments. In Fig.3.7, we plot $\Delta\theta$ as a function of $|\psi_{\rm in}\rangle \in \mathcal{A}$ with $\gamma \leq 0$. Although the estimation through the center-of-mass is not optimal ($\sqrt{m}\Delta\theta > 1/\sqrt{F_Q}$), the sensitivity can be better than the shot-noise, with $\Delta\theta \to \Delta\theta_{HL}$ for $|\psi_{\rm in}\rangle \to$ NOON.

Therefore, the center-of-mass estimation seems a promising strategy, since it allows for sub-shot-noise sensitivity with a calibration stage involving a probability in a one-dimensional space. However, as we shall show next, sub-shot noise sensitivities require the detection of all N atoms.

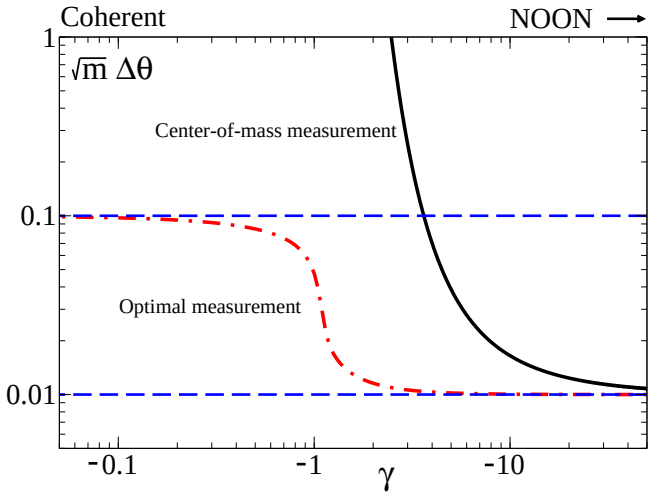

Fig. 3.7: The sensitivity $\sqrt{m}\Delta\theta$ (black solid line) calculated with Eq.(3.53), as a function of $|\psi_{in}\rangle \in \mathcal{A}$ with $\gamma < 0$ and $N = 100$. The values of $\sqrt{m}\Delta\theta_{SN}$ and $\sqrt{m}\Delta\theta_{HL}$ are denoted by the upper and lower dashed blue lines, respectively. The optimal sensitivity, given by the inverse of the QFI, is drawn with the red dot-dashed line.

If the the center-of-mass is calculated from $k < N$ particle positions, the probability (3.52) becomes $p^{(k)}_{cm}(x|\theta) = \int d\vec{x}_k\, \delta\left(x - \frac{1}{k}\sum_{i=1}^{k} x_i\right) p_k(\vec{x}_k|\theta)$, where $p_k(\vec{x}_k|\theta) = \int d\vec{x}_{N-k} p_N(\vec{x}_N|\theta)$. The latter can be given in explicit form:

$$p^{(k)}_{cm}(x|\theta) = \sqrt{\frac{2\sigma_0^2 k}{\pi\tilde{\sigma}^4}} \exp\left(-\frac{2x^2\sigma_0^2}{\tilde{\sigma}^4}k\right)\left[1 + \mathrm{A}\cos\left(k\theta + \frac{2kx_0}{\tilde{\sigma}^2}x\right)\right], \tag{3.54}$$

where

$$\mathrm{A} = 2\sum_{i=0}^{N-k}\binom{(N-k)}{i}\frac{C_i C_{i+k}}{\sqrt{\binom{N}{i+k}\binom{N}{i}}}. \tag{3.55}$$

For $k = N$ we recover the result from the previous section $\mathrm{A} = 2C_0C_N = (C_0 + C_N)^2/2$ (as we are using the symmetric states, $C_0 = C_N$). The FI for the probability (3.54) is

$$F = mk^2(1 - \sqrt{1 - \mathrm{A}^2}). \tag{3.56}$$

Let us now evaluate A, and in turn F, for various $k \simeq N$. For $k = N$ and the NOON state, we have $C_0 = C_N = \frac{1}{\sqrt{2}}$, giving $\mathrm{A} = 1$ and $F = mN^2$. From Eq.(3.55) it is apparent that, for any k, A is the sum of $N-k$ terms, each depending on the coefficients C_i and C_{i+k}. And thus for $k = N-1$, A will be maximal for a NOON-like state with $C_0 = C_{N-1} = 1/2$ and $C_1 = C_N = 1/2$. For this state we obtain $\mathrm{A} = \frac{1}{\sqrt{N}}$, and for large N the value of the FI is $F = mN$. Therefore,

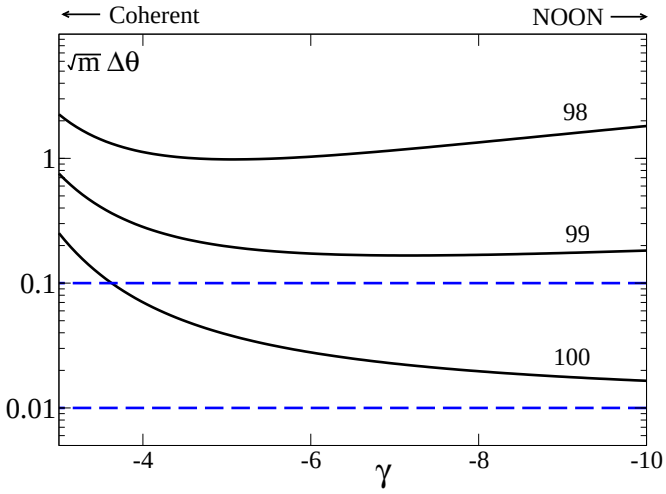

Fig. 3.8: The sensitivity $\sqrt{m}\Delta\theta$ (black solid line) calculated with Eq.(3.56), as a function of $|\psi_{in}\rangle \in \mathcal{A}$ with $\gamma < 0$ and $N = 100$. The values of $\sqrt{m}\Delta\theta_{SN}$ and $\sqrt{m}\Delta\theta_{HL}$ are denoted by, respectively, the upper and the lower dashed blue line. The three solid lines correspond to the phase sensitivity for estimation of the center-of-mass with different number of particles. For $k = 100$, the sensitivity is below the shot-noise and tends to $\sqrt{m}\Delta\theta_{HL}$ for $|\psi_{in}\rangle \to$ NOON. As soon as $k \neq N$, the sub-shot-noise sensitivity is lost and the value of $\sqrt{m}\Delta\theta$ increases dramatically.

the phase estimation using the center-of-mass of $N-1$ particles gives a sensitivity bounded by the shot-noise.

Each loss of an atom decreases the FI roughly by a factor of N, drastically deteriorating the sensitivity. In Fig.3.8 we plot the sensitivity $\sqrt{m}\Delta\theta$ calculated with the FI (3.56), for different $k \simeq N$. To calculate A, we choose the subset of $|\psi_{\rm in}\rangle \in \mathcal{A}$ which are in the vicinity of the NOON state. The Figure shows a dramatic loss of sensitivity as soon as $k \neq N$.

3.5.6 Effect of mode overlap on the Mach-Zehnder Interferometer sensitivity

So far, we focused on the position measurement of particles released from a double-well trap, and studied the phase estimation sensitivity. The fit to the density gives sensitivity limited by the shot-noise, and this bound can be overcome by phase estimation with correlation functions of the order of at least $\sqrt{N}$. As it is difficult to measure these correlations in the experiment, it will be challenging to beat the shot-noise limit using the interference pattern. Although the sensitivity

of the phase estimation based on the center-of-mass measurement can also be sub-shot-noise, the protocol is extremely vulnerable to the loss of particles.

In the above scenario, the sub-shot-noise sensitivity, which relies on non-classical correlations between the particles (entanglement), is reached by directly measuring spatial correlations between the atoms forming the interference pattern, and using the latter as estimators for the phase shift. On the other hand, it is well known that the Mach-Zehnder Interferometer can provide sub-shot-noise sensitivity just by a simple measurement of the population imbalance between the two wells, and a proper choice of the input state $|\psi_{\rm in}\rangle$. Indeed, the correlations between the two modes carry the part of the information contained in the particle correlations which is useful for phase estimation. When the clouds are released from the trap and the two modes start to overlap, the correlations between the two modes are lost, since a particle detected in the overlap region cannot be told to have come from either of the two initially separated clouds. This is the reason why it is necessary then to directly measure high-order spatial correlation functions in order to reach sub-shot-noise sensitivity.

It would be thus interesting to quantify the effect of the wave-packets' overlap on the sensitivity of the MZI. This analysis has also a practical interest since, in the implementation of the atomic MZI, the precision of the population imbalance measurement can be improved by opening the trap and letting the clouds expand for a while. In this way the density of the clouds drops, facilitating the measurement of the number of particles. However, during the expansion, the clouds inevitably start to overlap, leading to loss of information about the origin of the particles, as noted above. In this section, we show how the increasing overlap deteriorates the sensitivity of the MZI.

The double-well implementation of the MZI has been discussed in subsection 3.3. The corresponding transformation is given by Eq. (3.2). In order to analyze the sensitivity of the MZI, we use the conditional probability $p_N(\vec{x}_N|\theta)$ of detecting N atoms at positions $\vec{x}_N = x_1 \dots x_N$, already introduced above, now with the MZI evolution operator, instead of the simple phase shift. Therefore, the probability $p_N(\vec{x}_N|\theta)$ for the MZI is given by Eq.(3.34) with the $u_\theta(x,\varphi;t)$ given by

$$u_\theta(x,\varphi;t) = \tag{3.57}$$

$$= \left[\psi_{\rm l}(x,t)\cos\left(\frac{\theta}{2}\right) + \psi_{\rm r}(x,t)\sin\left(\frac{\theta}{2}\right)\right]\exp\left(i\frac{\varphi}{2}\right) \tag{3.58}$$

$$+ \left[\psi_{\rm r}(x,t)\cos\left(\frac{\theta}{2}\right) - \psi_{\rm l}(x,t)\sin\left(\frac{\theta}{2}\right)\right]\exp\left(-i\frac{\varphi}{2}\right). \tag{3.59}$$

The most common phase-estimation protocol discussed in context of the MZI is the mea-

surement of the population imbalance between the two arms of the interferometer. In order to assess how the sensitivity of this protocol is influenced by the expansion of the wave-packets, we introduce the probability of measuring n_L atoms in the left sub-space as follows

$$p_{\rm imb}(n_L|\theta) = \binom{N}{n_L} \int_{-\infty}^{0} d\vec{x}_{n_L} \int_{0}^{\infty} d\vec{x}_{N-n_L}\, p_N(\vec{x}_N|\theta). \tag{3.60}$$

This probability depends on the expansion time via $\psi_{\rm l/r}(x,t)$, which enter the definition of $p_N(\vec{x}_N|\theta)$. If the number m of population imbalance measurements is large enough, we can assume $p_{\rm imb}$ to be Gaussian. As already argued when studying the fit estimation, if then we choose a MLE strategy with this probability, the sensitivity saturates the CRLB:

$$\Delta^2\theta = \frac{1}{m}\frac{\Delta^2 n}{\left|\frac{\partial\langle n\rangle}{\partial\theta}\right|^2}, \tag{3.61}$$

where

$$\langle n\rangle = \int_0^\infty dx\, G_1(x|\theta) - \frac{N}{2} \tag{3.62}$$

is the average value of the population imbalance and

$$\Delta^2 n = \frac{N^2}{4} - \int_0^\infty \int_{-\infty}^0 d\vec{x}_2\, G_2(\vec{x}_2|\theta) - \langle n\rangle^2, \tag{3.63}$$

are the associated fluctuations.

When the two wave-packets don't overlap, i.e. $\psi_{\rm l}(x,t)\psi^*_{\rm r}(x,t) \simeq 0$ for all $x \in \mathbb{R}$, Eq.(3.61) simplifies to

$$\Delta^2\theta = \frac{1}{m}\frac{\Delta^2\hat{J}_x \sin^2\theta + \langle \hat{J}_z^2\rangle \cos^2\theta}{\langle \hat{J}_x\rangle^2 \cos^2\theta}. \tag{3.64}$$

This is the well-known expression for the sensitivity of the population imbalance between separated arms. It gives $\Delta\theta \leq \Delta\theta_{SN}$ for all $|\psi_{\rm in}\rangle \in \mathcal{A}$ with $\gamma \geq 0$.

We investigate the impact of the overlap on the sensitivity (3.61) by modelling the free expansion of the wave-packets $\psi_{\rm l/r}(x,t)$ by Gaussians,

$$\psi_{\rm l/r}(x,t) = \frac{1}{(2\pi\sigma_0^2(1+i\ t))^{1/4}} \exp\left(-\frac{(x\pm x_0)^2}{4\sigma^2(1+i\ t)}\right), \tag{3.65}$$

and take $x_0 = 1$ and the initial width $\sigma_0 = 0.1$. Notice that, differently from Eq. (3.43), here we have not assumed the expansion time t to be long, since we are interested in studying the effect of small mode overlap on the MZI sensitivity.

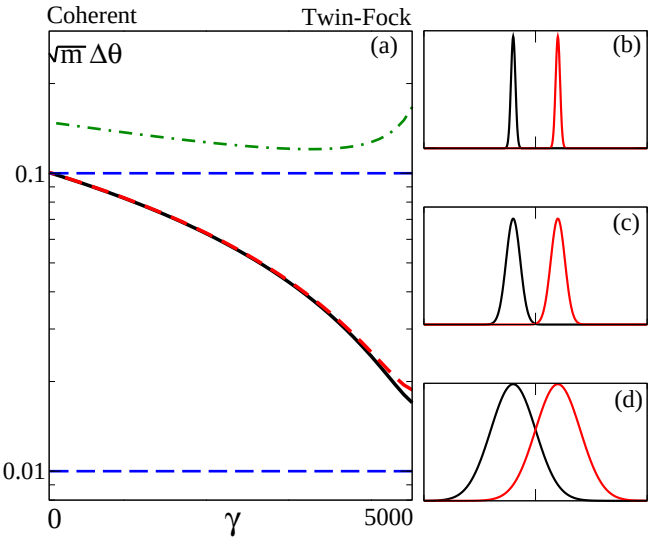

Fig. 3.9: (a) The sensitivity $\sqrt{m}\Delta\theta$ calculated with Eq.(3.61) for three different expansion times t, as a function of $|\psi_{in}\rangle \in \mathcal{A}$ with $\gamma \geq 0$, with $N = 100$ and $\theta = 0$. The solid black line corresponds to the situation shown in (b), where $t = 0$ and the wave-packets don't overlap. The dashed red line corresponds to (c), where $t = 3$ and the wave-packets start to overlap. The dot-dashed green line corresponds to (d), where $t = 10$ and the wave-packets strongly overlap. Clearly, the sensitivity is largely affected by any non-vanishing overlap. The values of $\sqrt{m}\Delta\theta_{SN}$ and $\sqrt{m}\Delta\theta_{HL}$ are denoted by respectively the upper and the lower dashed blue line.

In Fig. 3.9, we plot the sensitivity $\sqrt{m}\Delta\theta$, taking $\theta = 0$ and $N = 100$, for three different expansion times t. The initial sensitivity deteriorates as soon as the condensates start to overlap, and the sub-shot-noise sensitivity is lost for long expansion times.

As anticipated, we attribute this decline to the loss of information about the correlations between the modes. Therefore, special attention has to be paid to avoid the overlap when letting the two trapped condensates spread. Although we expect that the expansion facilitates the atom-number measurement, these results indicate that any overlap of the spatial modes has a strong negative impact on the sensitivity of the MZI.

3.5.7 Outlook

In this manuscript we have discussed in detail how the measurement of positions of atoms forming an interference pattern can be useful in context of atom interferometry.

We showed that the phase estimation based on the fit to the density gives sensitivity limited by the shot-noise. This is an important message, which, according to previous literature, had not yet been clarified.

On the other hand, we demonstrated that the sensitivity can be improved below the shot-noise limit by estimating the phase using correlation functions of order at least $\sqrt{N}$. Though this seems a powerful estimation strategy, even allowing for HL sensitivities, the experimental difficulty of measuring high-order correlations is a challenging experimental task. There are however recent experimental developments in single-atom detection with trapped BECs that seem very promising [40], and keep these estimation protocols from being considered impracticable already with small ($N \sim 1000$) condensates. It must be considered that, in order to make sub-shot noise interferometry to be an actual advantage over its classical counterpart, the total number of particle must be sufficiently large for the $1/\sqrt{N}$ gain to be sizable.

From the foundational point of view, it would be anyway interesting to perform proof-of-principle experiments with very few particles, such that the measurement of the full N-body correlation function could be performed with current detection capabilities. Photons would thus be better candidates over atoms, since non-classical -and in particular NOON- states of very few particles have already been experimentally created.

Bibliography, Part II

[1] B. P. Anderson and M. A. Kasevich. Macroscopic Quantum Interference from Atomic Tunnel Arrays. *Science*, 282(5394):1686–1689, 1998.

[2] M. Antezza, L. P. Pitaevskii, and S. Stringari. Effect of the casimir-polder force on the collective oscillations of a trapped bose-einstein condensate. *Phys. Rev. A*, 70(5):053619, Nov 2004.

[3] F. T. Arecchi, E. Courtens, R. Gilmore, and H. Thomas. Atomic coherent states in quantum optics. *Phys. Rev. A*, 6(6):2211–2237, Dec 1972.

[4] R. Bach and K. Rzążewski. Correlations in atomic systems: Diagnosing coherent superpositions. *Phys. Rev. Lett.*, 92(20):200401, May 2004.

[5] F. Baumgärtner, R. J. Sewell, S. Eriksson, I. Llorente-Garcia, J. Dingjan, J. P. Cotter, and E. A. Hinds. Measuring energy differences by bec interferometry on a chip. *Phys. Rev. Lett.*, 105(24):243003, Dec 2010.

[6] D. W. Berry, B. L. Higgins, S. D. Bartlett, M. W. Mitchell, G. J. Pryde, and H. M. Wiseman. How to perform the most accurate possible phase measurements. *Phys. Rev. A*, 80(5):052114, Nov 2009.

[7] D. W. Berry and H. M. Wiseman. Optimal states and almost optimal adaptive measurements for quantum interferometry. *Phys. Rev. Lett.*, 85(24):5098–5101, Dec 2000.

[8] P. Böhi, M. F. Riedel, J. Hoffrogge, J. Reichel, T. W. Hänsch, and P. Treutlein. oherent manipulation of boseeinstein condensates with state-dependent microwave potentials on an atom chip. *Nature Physics*, 5:592–597, 2009.

[9] S. Boixo, A. Datta, M. J. Davis, S. T. Flammia, A. Shaji, and C. M. Caves. Quantum metrology: Dynamics versus entanglement. *Phys. Rev. Lett.*, 101(4):040403, Jul 2008.

[10] S. Boixo, S. T. Flammia, C. M. Caves, and J. Geremia. Generalized limits for single-parameter quantum estimation. *Phys. Rev. Lett.*, 98(9):090401, Feb 2007.

[11] J. J. . Bollinger, W. M. Itano, D. J. Wineland, and D. J. Heinzen. Optimal frequency measurements with maximally correlated states. *Phys. Rev. A*, 54(6):R4649–R4652, Dec 1996.

[12] S. L. Braunstein and C. M. Caves. Statistical distance and the geometry of quantum states. *Phys. Rev. Lett.*, 72(22):3439–3443, May 1994.

[13] S. L. Braunstein, C. M. Caves, and G. J. Milburn. Generalized uncertainty relations: Theory, examples, and lorentz invariance. *Annals of Physics*, 247(1):135 – 173, 1996.

[14] H. Cable and G. A. Durkin. Parameter estimation with entangled photons produced by parametric down-conversion. *Phys. Rev. Lett.*, 105(1):013603, Jul 2010.

[15] G. K. Campbell, A. E. Leanhardt, J. Mun, M. Boyd, E. W. Streed, W. Ketterle, and D. E. Pritchard. Photon recoil momentum in dispersive media. *Phys. Rev. Lett.*, 94(17):170403, May 2005.

[16] R. A. Campos, C. C. Gerry, and A. Benmoussa. Optical interferometry at the heisenberg limit with twin fock states and parity measurements. *Phys. Rev. A*, 68(2):023810, Aug 2003.

[17] I. Carusotto, L. Pitaevskii, S. Stringari, G. Modugno, and M. Inguscio. Sensitive measurement of forces at the micron scale using bloch oscillations of ultracold atoms. *Phys. Rev. Lett.*, 95(9):093202, Aug 2005.

[18] Y. Castin and J. Dalibard. Relative phase of two bose-einstein condensates. *Phys. Rev. A*, 55(6):4330–4337, Jun 1997.

[19] C. M. Caves. Quantum-mechanical noise in an interferometer. *Phys. Rev. D*, 23(8):1693–1708, Apr 1981.

[20] C. Chin, R. Grimm, P. Julienne, and E. Tiesinga. Feshbach resonances in ultracold gases. *Rev. Mod. Phys.*, 82(2):1225–1286, Apr 2010.

[21] H. Cramer. *Mathematical methods of Statistics*. University Press, Princeton, 1946.

[22] A. D. Cronin, J. Schmiedmayer, and D. E. Pritchard. Optics and interferometry with atoms and molecules. *Rev. Mod. Phys.*, 81(3):1051–1129, Jul 2009.

[23] B. Deh, C. Marzok, S. Slama, C. Zimmermann, and P. Courteille. Bragg spectroscopy and ramsey interferometry with an ultracold fermi gas. *Applied Physics B: Lasers and Optics*, 97:387–396, 2009. 10.1007/s00340-009-3736-0.

[24] R. Demkowicz-Dobrzanski, U. Dorner, B. J. Smith, J. S. Lundeen, W. Wasilewski, K. Banaszek, and I. A. Walmsley. Quantum phase estimation with lossy interferometers. *Phys. Rev. A*, 80(1):013825, Jul 2009.

[25] U. Dorner, R. Demkowicz-Dobrzanski, B. J. Smith, J. S. Lundeen, W. Wasilewski, K. Banaszek, and I. A. Walmsley. Optimal quantum phase estimation. *Phys. Rev. Lett.*, 102(4):040403, Jan 2009.

[26] J. P. Dowling. Correlated input-port, matter-wave interferometer: Quantum-noise limits to the atom-laser gyroscope. *Phys. Rev. A*, 57(6):4736–4746, Jun 1998.

[27] J. Estéve, C. Gross, A. Weller, S. Giovanazzi, and M. K. Oberthaler. Squeezing and entanglement in a boseeinstein condensate. *Nature*, 455:1216–1219, 2008.

[28] M. Fattori, C. D'Errico, G. Roati, M. Zaccanti, M. Jona-Lasinio, M. Modugno, M. Inguscio, and G. Modugno. Atom interferometry with a weakly interacting bose-einstein condensate. *Phys. Rev. Lett.*, 100(8):080405, Feb 2008.

[29] M. Fattori, G. Roati, B. Deissler, C. D'Errico, M. Zaccanti, M. Jona-Lasinio, L. Santos, M. Inguscio, and G. Modugno. Magnetic dipolar interaction in a bose-einstein condensate atomic interferometer. *Phys. Rev. Lett.*, 101(19):190405, Nov 2008.

[30] T. Fernholz, H. Krauter, K. Jensen, J. F. Sherson, A. S. Sørensen, and E. S. Polzik. Spin squeezing of atomic ensembles via nuclear-electronic spin entanglement. *Phys. Rev. Lett.*, 101(7):073601, Aug 2008.

[31] J. Fortágh, H. Ott, S. Kraft, A. Günther, and C. Zimmermann. Surface effects in magnetic microtraps. *Phys. Rev. A*, 66(4):041604, Oct 2002.

[32] W.-B. Gao, C.-Y. Lu, X.-C. Yao, P. Xu, O. Guhne, A. Goebel, Y.-A. Chen, C.-Z. Peng, Z.-B. Chen, and J.-W. Pan. Experimental demonstration of a hyper-entangled ten-qubit schrodinger cat state. *Nature Physics*, 6:331–335, 2010.

[33] R. Gati, B. Hemmerling, J. Fölling, M. Albiez, and M. K. Oberthaler. Noise thermometry with two weakly coupled bose-einstein condensates. *Phys. Rev. Lett.*, 96(13):130404, Apr 2006.

[34] V. Giovannetti, S. Lloyd, and L. Maccone. Quantum-Enhanced Measurements: Beating the Standard Quantum Limit. *Science*, 306(5700):1330–1336, 2004.

[35] V. Giovannetti, S. Lloyd, and L. Maccone. Quantum metrology. *Phys. Rev. Lett.*, 96(1):010401, Jan 2006.

[36] K. Goda, O. Miyakawa, E. E. Mikhailov, S. Saraf, R. Adhikari, K. McKenzie, R. Ward, S. Vass, A. J. Weinstein, and N. Mavalvala. A quantum-enhanced prototype gravitational-wave detector. *Nature Physics*, 4:472–476, 2008.

[37] J. Grond, U. Hohenester, I. Mazets, and J. Schmiedmayer. Atom interferometry with trapped boseeinstein condensates: impact of atomatom interactions. *New Journal of Physics*, 12(6):065036, 2010.

[38] C. Gross, T. Zibold, E. Nicklas, J. Estéve, and M. K. Oberthaler. Nonlinear atom interferometer surpasses classical precision limit. *Nature*, 464:1165–1169, 2010.

[39] M. Gustavsson, E. Haller, M. J. Mark, J. G. Danzl, G. Rojas-Kopeinig, and H.-C. Nägerl. Control of interaction-induced dephasing of bloch oscillations. *Phys. Rev. Lett.*, 100(8):080404, Feb 2008.

[40] D. Heine, W. Rohringer, D. Fischer, M. Wilzbach, T. Raub, S. Loziczky, X. Liu, S. Groth, B. Hessmo, and J. Schmiedmayer. A single-atom detector integrated on an atom chip: fabrication, characterization and application. *New Journal of Physics*, 12(9):095005, 2010.

[41] C. W. Helstrom. *Quantum Detection and Estimation Theory.* Academic Press, New York, 1976.

[42] C. Henkel, S. Ptting, and M. Wilkens. Loss and heating of particles in small and noisy traps. *Applied Physics B: Lasers and Optics*, 69:379–387, 1999. 10.1007/s003400050823.

[43] B. L. Higgins, D. W. Berry, S. D. Bartlett, H. M. Wiseman, and G. J. Pryde. Entanglement-free heisenberg-limited phase estimation. *Nature*, 450:393–396, 2007.

[44] A. S. Holevo. *Probabilistic and Statistical Aspects of Quantum Theory.* North-Holland, Amsterdam, 1982.

[45] M. J. Holland and K. Burnett. Interferometric detection of optical phase shifts at the heisenberg limit. *Phys. Rev. Lett.*, 71(9):1355–1358, Aug 1993.

[46] R. Horodecki, P. Horodecki, M. Horodecki, and K. Horodecki. Quantum entanglement. *Rev. Mod. Phys.*, 81(2):865–942, Jun 2009.

[47] Y. P. Huang and M. G. Moore. Optimized double-well quantum interferometry with gaussian squeezed states. *Phys. Rev. Lett.*, 100(25):250406, Jun 2008.

[48] P. Hyllus, O. Gühne, and A. Smerzi. Not all pure entangled states are useful for sub-shot-noise interferometry. *Phys. Rev. A*, 82(1):012337, Jul 2010.

[49] H. Hffner, C. Roos, and R. Blatt. Quantum computing with trapped ions. *Physics Reports*, 469(4):155 – 203, 2008.

[50] J. Javanainen and S. M. Yoo. Quantum phase of a bose-einstein condensate with an arbitrary number of atoms. *Phys. Rev. Lett.*, 76(2):161–164, Jan 1996.

[51] G.-B. Jo, Y. Shin, S. Will, T. A. Pasquini, M. Saba, W. Ketterle, D. E. Pritchard, M. Vengalattore, and M. Prentiss. Long phase coherence time and number squeezing of two bose-einstein condensates on an atom chip. *Phys. Rev. Lett.*, 98(3):030407, Jan 2007.

[52] M. P. A. Jones, C. J. Vale, D. Sahagun, B. V. Hall, and E. A. Hinds. Spin coupling between cold atoms and the thermal fluctuations of a metal surface. *Phys. Rev. Lett.*, 91(8):080401, Aug 2003.

[53] T. Köhler, K. Góral, and P. S. Julienne. Production of cold molecules via magnetically tunable feshbach resonances. *Rev. Mod. Phys.*, 78(4):1311–1361, Dec 2006.

[54] A. E. Leanhardt, Y. Shin, A. P. Chikkatur, D. Kielpinski, W. Ketterle, and D. E. Pritchard. Bose-einstein condensates near a microfabricated surface. *Phys. Rev. Lett.*, 90(10):100404, Mar 2003.

[55] C. Lee. Adiabatic mach-zehnder interferometry on a quantized bose-josephson junction. *Phys. Rev. Lett.*, 97(15):150402, Oct 2006.

[56] D. Leibfried, E. Knill, S. Seidelin, J. Britton, R. B. Blakestad, J. Chiaverini, D. B. Hume, W. M. Itano, J. D. Jost, C. Langer, R. Ozeri, R. Reichle, and D. J. Wineland. Creation of a six-atom 'schrdinger cat' state. *Nature*, 438:639–642, 2005.

[57] Y.-j. Lin, I. Teper, C. Chin, and V. Vuletić. Impact of the casimir-polder potential and johnson noise on bose-einstein condensate stability near surfaces. *Phys. Rev. Lett.*, 92(5):050404, Feb 2004.

[58] R. Loudon. Quantum limit on the michelson interferometer used for gravitational-wave detection. *Phys. Rev. Lett.*, 47(12):815–818, Sep 1981.

[59] A. Luis. Nonlinear transformations and the heisenberg limit. *Physics Letters A*, 329(1-2):8 – 13, 2004.

[60] J. C. F. Matthews, A. Politi, A. Stefanov, and J. L. O'Brien. Manipulation of multiphoton entanglement in waveguide quantum circuits. *Nature Photonics*, 3:346–350, 2009.

[61] K. Maussang, G. E. Marti, T. Schneider, P. Treutlein, Y. Li, A. Sinatra, R. Long, J. Estève, and J. Reichel. Enhanced and reduced atom number fluctuations in a bec splitter. *Phys. Rev. Lett.*, 105(8):080403, Aug 2010.

[62] M. W. Mitchell, J. S. Lundeen, and A. M. Steinberg. Super-resolving phase measurements with a multiphoton entangled state. *Nature*, 429:161–164, 2004.

[63] W. J. Mullin, R. Krotkov, and F. Laloë. The origin of the phase in the interference of bose-einstein condensates. *American Journal of Physics*, 74(10):880–887, 2006.

[64] T. Nagata, R. Okamoto, J. L. O'Brien, K. Sasaki, and S. Takeuchi. Beating the Standard Quantum Limit with Four-Entangled Photons. *Science*, 316(5825):726–729, 2007.

[65] M. A. Nielsen and I. L. Chuang. *Quantum Computation and Quantum Information*. University Press, Cambridge, 2000.

[66] J. M. Obrecht, R. J. Wild, M. Antezza, L. P. Pitaevskii, S. Stringari, and E. A. Cornell. Measurement of the temperature dependence of the casimir-polder force. *Phys. Rev. Lett.*, 98(6):063201, Feb 2007.

[67] C. Orzel, A. K. Tuchman, M. L. Fenselau, M. Yasuda, and M. A. Kasevich. Squeezed States in a Bose-Einstein Condensate. *Science*, 291(5512):2386–2389, 2001.

[68] T. A. Pasquini, Y. Shin, C. Sanner, M. Saba, A. Schirotzek, D. E. Pritchard, and W. Ketterle. Quantum reflection from a solid surface at normal incidence. *Phys. Rev. Lett.*, 93(22):223201, Nov 2004.

[69] P. Pedri, L. Pitaevskii, S. Stringari, C. Fort, S. Burger, F. S. Cataliotti, P. Maddaloni, F. Minardi, and M. Inguscio. Expansion of a coherent array of bose-einstein condensates. *Phys. Rev. Lett.*, 87(22):220401, Nov 2001.

[70] A. Peres. *Quantum Theory: Concepts and Methods.* Kluwer, Dordrecht, 1995.

[71] L. Pezzé, L. A. Collins, A. Smerzi, G. P. Berman, and A. R. Bishop. Sub-shot-noise phase sensitivity with a bose-einstein condensate mach-zehnder interferometer. *Phys. Rev. A*, 72(4):043612, Oct 2005.

[72] L. Pezzé and A. Smerzi. Phase sensitivity of a mach-zehnder interferometer. *Phys. Rev. A*, 73(1):011801, Jan 2006.

[73] L. Pezzé and A. Smerzi. Mach-zehnder interferometry at the heisenberg limit with coherent and squeezed-vacuum light. *Phys. Rev. Lett.*, 100(7):073601, Feb 2008.

[74] L. Pezzé and A. Smerzi. Entanglement, nonlinear dynamics, and the heisenberg limit. *Phys. Rev. Lett.*, 102(10):100401, Mar 2009.

[75] M. F. Riedel, P. Böhi, Y. Li, T. W. Hänsch, A. Sinatra, and P. Treutlein. Atom-chip-based generation of entanglement for quantum metrology. *Nature*, 464:1170–1173, 2010.

[76] G. Roati, E. de Mirandes, F. Ferlaino, H. Ott, G. Modugno, and M. Inguscio. Atom interferometry with trapped fermi gases. *Phys. Rev. Lett.*, 92(23):230402, Jun 2004.

[77] G. Roati, M. Zaccanti, C. D'Errico, J. Catani, M. Modugno, A. Simoni, M. Inguscio, and G. Modugno. ^{39}k bose-einstein condensate with tunable interactions. *Phys. Rev. Lett.*, 99(1):010403, Jul 2007.

[78] M. Rosenkranz and D. Jaksch. Parameter estimation with cluster states. *Phys. Rev. A*, 79(2):022103, Feb 2009.

[79] S. M. Roy and S. L. Braunstein. Exponentially enhanced quantum metrology. *Phys. Rev. Lett.*, 100(22):220501, Jun 2008.

[80] Y. Shin, M. Saba, T. A. Pasquini, W. Ketterle, D. E. Pritchard, and A. E. Leanhardt. Atom interferometry with bose-einstein condensates in a double-well potential. *Phys. Rev. Lett.*, 92(5):050405, Feb 2004.

[81] A. Sorensen, L.-M. Duan, J. I. Cirac, and P. Zoller. Many-particle entanglement with bose-einstein condensates. *Nature*, 409:63–66, 2001.

[82] C. I. Sukenik, M. G. Boshier, D. Cho, V. Sandoghdar, and E. A. Hinds. Measurement of the casimir-polder force. *Phys. Rev. Lett.*, 70(5):560–563, Feb 1993.

[83] P. Treutlein, P. Hommelhoff, T. Steinmetz, T. W. Hänsch, and J. Reichel. Coherence in microchip traps. *Phys. Rev. Lett.*, 92(20):203005, May 2004.

[84] H. Uys and P. Meystre. Quantum states for heisenberg-limited interferometry. *Phys. Rev. A*, 76(1):013804, Jul 2007.

[85] H. Vahlbruch, M. Mehmet, S. Chelkowski, B. Hage, A. Franzen, N. Lastzka, S. Goßler, K. Danzmann, and R. Schnabel. Observation of squeezed light with 10-db quantum-noise reduction. *Phys. Rev. Lett.*, 100(3):033602, Jan 2008.

[86] P. Walther, J.-W. Pan, M. Aspelmeyer, R. Ursin, S. Gasparoni, and A. Zeilinger. De broglie wavelength of a non-local four-photon state. *Nature*, 429:158–161, 2004.

[87] T. Weber, J. Herbig, M. Mark, H.-C. Nagerl, and R. Grimm. Bose-Einstein Condensation of Cesium. *Science*, 299(5604):232–235, 2003.

[88] R. F. Werner. Quantum states with einstein-podolsky-rosen correlations admitting a hidden-variable model. *Phys. Rev. A*, 40(8):4277–4281, Oct 1989.

[89] P. J. Windpassinger, D. Oblak, P. G. Petrov, M. Kubasik, M. Saffman, C. L. G. Alzar, J. Appel, J. H. Müller, N. Kjærgaard, and E. S. Polzik. Nondestructive probing of rabi oscillations on the cesium clock transition near the standard quantum limit. *Phys. Rev. Lett.*, 100(10):103601, Mar 2008.

[90] D. J. Wineland, J. J. Bollinger, W. M. Itano, and D. J. Heinzen. Squeezed atomic states and projection noise in spectroscopy. *Phys. Rev. A*, 50(1):67–88, Jul 1994.

[91] P. Wolf, P. Lemonde, A. Lambrecht, S. Bize, A. Landragin, and A. Clairon. From optical lattice clocks to the measurement of forces in the casimir regime. *Phys. Rev. A*, 75(6):063608, Jun 2007.

[92] W. K. Wootters. Statistical distance and hilbert space. *Phys. Rev. D*, 23(2):357–362, Jan 1981.

[93] B. Yurke, S. L. McCall, and J. R. Klauder. Su(2) and su(1,1) interferometers. *Phys. Rev. A*, 33(6):4033–4054, Jun 1986.

Conclusions

In the work presented in this dissertation, we have seen how dilute ultracold atomic BECs are very promising systems where to study superfluid phenomena, as well as the implementation of quantum interferometers. Both aspects can be investigated using the same BEC setup: a double-well trap.

First, we have considered the flow of a dilute BEC through a weak link, where macroscopic Josephson oscillations, superfluid critical velocities and dissipation dynamics can be studied.

We analyzed the properties of transport through the weak link by studying the dependence of the total current on the phase difference existing at the two ends of the link, thereby constructing the so-called current-phase relation. The latter can be used to characterize the crossover from tunneling to hydrodynamic transport, since the dependence of the current on the phase difference changes from sinusoidal to multivalued. Apart from studying this crossover, already demonstrated experimentally with superfluid helium, we discovered a new regime of current-phase relation which is characterized by a different kind of multivaluedness. This discovery is highly interesting, since this new regime can be related to a novel behavior of current oscillations in the Josephson ac effect, which could be observable with dilute BECs. However, in order to subsantiate this conclusion, further systematical study of the dynamics is required, especially in order to propose a possible experimental observation of this novel regime using a BEC trapped in a double-well.

So far, the experimental measurement of current-phase relation with dilute BECs, and therefore also the observation of the crossover from tunneling to hydrodynamic transport, has not been made. However, we have shown, with the support of experimental data, that this crossover can be experimentally demonstrated by analyzing the frequency of the Josephson plasma oscillations in a double-well trap with tunable barrier height. This has been done by verifying a remarkably good agreement of the experimental data with the superfluid hydrodynamics equations (in the strong-coupling regime), with a two-mode model (in the tunneling regime), and with the Gross-Pitaevskii equation in the intermediate regime. This result is a clear example of how to

exploit the cleannes of the BEC system, allowing for a direct comparison of experimental data with simple theoretical models, toghether with the refined control over the trapping parameters, allowing for tuning the inter-well barrier from zero to a value larger than the chemical potential.

We have seen that the current-phase relation carries also informations about the superfluid instability, since the Josephson critical current, i.e. the highest current possible for any imposed phase difference, is related to the critical velocity above which the superfluid starts to be dissipated. We studied this instability by determining the highest velocity for which no excitations were present inside the bulk of the cloud, using the time-dependent Gross-Pitaevskii equation. We also investigated the dissipation dynamics above the critical value. We studied the superfluid dissipation through the phase slip mechanism in one, two, and three dimensional weak links, where the excitations are solitons, vortices, and vortex lines/rings, respectively.

In two and three dimensions, the dynamics is very rich, and we found that the nature of the excitations and their dynamics is dramatically dependent on the weak-link geometry. Remarkably, the slightest axial asymmetry about the flow direction makes vortex rings unstable toward breaking. We considered two configurations which are of experimental relevance in the context of ultracold BECs: a waveguide and a torus. The latter setup, where superfluid persistent current have already been experimentally observed, is of particular interest also from the interferometric point of view, since it can be used as a rotation sensor, in analogy to SQUID devices already realized with superfluid helium.

Our study is the first to systematically address the dynamics of phase slip dissipation inside a constriction in a fully three-dimensional geometry. The possibility to study the superfluid instability dynamics with a theoretical model which is experimentally relevant is a very important advantage of dilute BECs over strongly interacting superfluids like helium II. In the latter context indeed, different vortex structures responsible for phase slip dissipation have been proposed, but their actual relevance was assessed mainly through the agreement between the corresponding estimate for the critical velocity and the experimental data.

Throughout all our studies of superfluid dissipation, we have been looking for a general criterion determining the critical velocity. We found that the hydrodynamic local criterion, $v(\boldsymbol{r}) = c(\boldsymbol{r})$, according to which the critical velocity is reached as soon as the local fluid velocity equals the local sound speed at any point in the fluid, is verified only in one-dimensional cases, while in two and three dimensions we discovered a new criterion to hold, $v_{\mathrm{TF}} = c_{\mathrm{tr}}$: the instability sets in when the fluid velocity at the Thomas-Fermi surface of the cloud equals the "true" sound speed, that is, the actual velocity of propagation of low-lying Bogoliubov modes, which depends

on the geometry of the weak link.

This finding is very interesting and somewhat unexpected, and has left several open questions. First of all, it is not clear why the hydrodynamic local criterion $v(\boldsymbol{r}) = c(\boldsymbol{r})$ fails when going from one to two/three dimensions, since none of the underlying assumptions seems related to the dimensionality of the system. A first step toward answering this question can be made by observing that the condition $v(\boldsymbol{r}) = c(\boldsymbol{r})$ can still be associated with an instability, yet not the one which dissipates the superfluid flow, but rather remains confined outside the surface of the cloud, with vortices trying to penetrate the bulk and not succeeding. Moreover, the physical origin of our new found criterion, which predicts very well the Gross-Pitaevskii instability toward superfluid dissipation, and seems more general than the local criterion $v(\boldsymbol{r}) = c(\boldsymbol{r})$, is not yet clear. This is in part due to unclear issues about the instability of the Gross-Pitaevskii equation at the critical velocity in presence of macroscopic obstacles, like the weak link case we study here. The instability seems indeed to be connected with the disappearance of the stationary solutions, at least for the flow through single obstacles, but it is not known whether it corresponds to any dynamical/energetical instability. Therefore, the comparison with predictions based on energetic arguments, similar to the well known Feynman criterion (on which most of the studies of the critical velocity for superfluid helium are based), or even with the results of a full linear stability analysis, can be very useful in understanding this important matters.

In the second part of this dissertation, we turned to the study of possible implementation of quantum interferometers with dilute BECs in double-well traps, where every operation is performed by dynamical manipulation of the inter-well barrier.

With this respect, the above described experimental analysis of Josephson plasma frequency in the crossover between strongly coupled (hydrodynamic) to tunneling coupled superfluids, provides a very useful piece of information. Indeed, in performing the spitting/recombination of the two clouds, necessary for closed loop interferometry, any spurious excitation must be carefully avoided, and thus the low-lying modes frequencies must be known for all barrier heights.

Starting from the observation that a double-well Mach-Zehnder interferometer requires an exquisite control over the dynamical manipulation of both the inter-well barrier and the atom-atom interactions, we proposed two simpler schemes: i) a Rabi interferometer, where the phase shift takes place while the atoms oscillate between the two wells, and ii) an interferometer based on the position measurement of the atoms released from the trap and forming a two-slit interference pattern.

As the price to pay for a simpler interferomettric scheme, we find that the Rabi interferometer

has a sensitivity which is generally worse than the Mach-Zehnder. However, the sensitivity still scales in the same way with the number of resources employed (number of particles in input), and in particular becomes better that the shot-noise sensitivity (scaling as $1/\sqrt{N}$) when entangled states are used. We studied the sensitivity of the Rabi interferometer for the measurement of weak forces, considering realistic sources of experimental noise. We analyzed in detail an application to the measurement of the Casimir-Polder force, and found that, even without quantum enhancement of the sensitivity, the zero and finite temperature regimes of the Casimir interaction can be discriminated. This result has not been achieved in previous measurements of the Casimir-Polder force, but our calculations show that it should be possible with current-technology using BECs trapped in a double-well.

For the second interferometer proposed, we have first analyzed the phase estimation based on a fit of the average density to the interference pattern, and found that the sensitivity is always worse than the shot-noise. This result had not been stated in previous literature, where also some arguments leading to the opposite conlusion have been given.

After observing that the fit is shot-noise limited because it actually disregards particle correlations, we have demonstrated that the latter can indeed be measured in order to infer the phase with a sub-shot noise sensitivity. In particular, the shot-noise limit can be overcome only using correlation functions of order k not smaller than $\sqrt{N}$, where N is the total number of particles. Remarkably, we have shown that when $k = N$ the measurement is optimal, i.e. it corresponds to the best possible choice of the quantity to measure in order to infer the phase, and the sensitivity reaches the Heisenberg limit, scaling as $1/N$.

The fact that sub-shot noise sensitivities are reached only by such refined measurements is due to the overlap between the two clouds, which washes out the information about the modes, since it is not possible to determine then whether a particle came from either of the two wells. We also showed that indeed this overlap dramatically deteriorates the sensitivity also in the double-well Mach-Zehnder interferometer.

The measurement of the center of mass of all the N particles also provides sub-shot-noise sensitivity, but, as well as the correlation function-based scheme described above, would be very challenging to implement experimentally, since it requires very refined detection tools. A main message resulting from our study of phase estimation schemes based on the interference pattern is indeed that, for particle numbers sufficiently high that the sub-shot-noise sensitivity (in the best case scaling as $1/N$) becomes an actual gain over shot-noise sensitivity, these schemes would be extremely demanding from an experimental point of view. There are however recent important

developments in the atom detection capabilities, according to which, at least with a mesoscopic BEC with about 1000 atoms, single atom detection with high efficiency could be performed on a very large fraction of the cloud, therefore suggesting that the correlation function-based scheme described above might become possible.

PUBLICATIONS

1) F. Piazza, L. Pezzé and A. Smerzi, "Macroscopic Superpositions of Phase States with Bose-Einstein condensates", Phys. Rev. A 78, 051601(R) (2008)

2) F. Piazza, L. A. Collins, and A. Smerzi, "Vortex-induced phase-slip dissipation in a toroidal Bose-Einstein condensate flowing through a barrier ", Phys. Rev. A 80, 021601(R) (2009)

3) G. Watanabe, F. Dalfovo, F. Piazza, L. P. Pitaevskii, and S. Stringari, "Critical velocity of superfluid flow through single-barrier and periodic potentials ", Phys. Rev. A 80, 053602 (2009)

4) F. Piazza, L. A. Collins, and A. Smerzi, "Current-phase relation of a Bose-Einstein condensate flowing through a weak link ", Phys. Rev. A 81, 033613 (2010)

5) J. Chwedeńczuk, L. Pezzé, F. Piazza, A. Smerzi, "Rabi Interferometry and Sensitive Measurement of the Casimir-Polder Force with Ultra-Cold Gases", Phys. Rev. A 82, 032104 (2010)

6) L. J. LeBlanc, A. B. Bardon, J. McKeever, M. H. T. Extavour, D. Jervis, J. H. Thywissen, F. Piazza, A. Smerzi, "Dynamics of a tunable superfluid junction ", Phys. Rev. Lett. 106, 025302 (2011).

7) J. Chwedeńczuk, F. Piazza, A. Smerzi, "Phase Estimation With Interfering Bose-Condensed Atomic Clouds", Phys. Rev. A 82, 051601(R) (2010)

8) F. Piazza, L. A. Collins, and A. Smerzi, "Instability and Vortex Rings Dynamics in a Three-Dimensional Superfluid Flow Through a Constriction ", arXiv:1011.5041v1

9) J. Chwedeńczuk, F. Piazza, A. Smerzi, "Phase Estimation from Atom Position Measurements", arXiv:1012.3593v1